Collider physics in anticipation of new TeV-scale phenomena

Dissertation

Zum Erlangen des akademischen Grades
"Doktor der Naturwissenschaften"
an der Fakultät Physik der Technischen
Universität Dortmund

Henning Sedello

Dezember 2013

Tag der mündlichen Prüfung:	25. Februar 2014
Prüfungskommission:	Prof. Dr. R. Böhmer, Prof. Dr. G. Hiller, Prof. Dr. H. Päs, PD Dr. R. Klingenberg
Erstgutachterin:	Prof. Dr. G. Hiller
Zweitgutachter:	Prof. Dr. H. Päs

Abstract

In this thesis, we perform phenomenological studies in the Minimal Supersymmetric Standard Model (MSSM) and in the model of large extra dimensions by Arkani-Hamed, Dimopoulos, and Dvali (ADD).

In the MSSM, parts of the up-type squark flavor structure are inaccessible in low-energy precision measurements. We discuss the prospects to constrain these parts by measuring a macroscopic lifetime of a directly produced light stop. Such a lifetime can exceed the order of picoseconds in the Minimal-Flavor-Violation scheme if the light stop ($\tilde{t}_1$) predominantly decays as $\tilde{t}_1 \to c\tilde{\chi}_1^0$ to a charm quark (c) and a lightest neutralino ($\tilde{\chi}_1^0$). We discuss kinematics of this decay for stops hypothetically produced in the $pp \to \tilde{t}_1\tilde{t}_1\overline{tt}$ channel at the Large Hadron Collider (LHC). We find that the transverse impact parameters of the charmed decay products can be of $\mathcal{O}(180\,\mu\text{m})$ for a stop lifetime of 1 ps. We further discuss $\tilde{t}_1 \to c\tilde{\chi}_1^0$ for a bino-like $\tilde{\chi}_1^0$ subsequently decaying to a photon and a light gravitino in $\tilde{t}_1\tilde{t}_1^*$ events. This scenario is significantly constrained by early 7-TeV LHC data.

In the ADD model, we discuss graviton-enhanced dilepton production within the Asymptotic-Safety Scenario of quantum gravity, using a newly developed implementation of the relevant processes in the Monte-Carlo generator PYTHIA 8. From the results of recent 20-fb^{-1} CMS searches for anomalous dilepton production at high dilepton invariant masses, we derive bounds on the transition scale associated with the ultraviolet fixed-point of Newtons coupling in the Asymptotic-Safety Scenario.

Zusammenfassung

Inhalt dieser Dissertation sind phänomenologische Studien zum minimalen supersymmetrischen Standardmodell (MSSM) und zum ADD-Modell der großen zusätzlichen Dimensionen nach Arkani-Hamed, Dimopoulos und Dvali.

Teile der Flavorstruktur des MSSMs können nicht in niederenergetischen Präzisionsmessungen untersucht werden. Wir erörtern, ob sie stattdessen durch Messungen der Lebensdauern direkt erzeugter leichter Stops beschränkt werden können. Wenn Flavorverletzung minimal realisiert ist, kann das leichtere Stop ($\tilde{t}_1$) eine Lebensdauer in der Größenordnung von Pikosekunden haben, sofern es primär ein Charm-Quark und ein leichtestes Neutralino ($\tilde{\chi}_1^0$) zerfällt. Wir untersuchen die Kinematik des hypothetischen Stopzerfalls in ($pp \to \tilde{t}_1\tilde{t}_1\overline{tt}$)-Produktion für den LHC. Hier erwarten wir, dass die transversalen Impaktparameter der hadronischen Zerfallsprodukte in der Größenordnung von 180 µm für eine Stoplebensdauer von einer Pikosekunde liegen. Wir betrachten außerdem den Fall, dass in $\tilde{t}_1\tilde{t}_1^*$-Ereignissen ein binoartiges $\tilde{\chi}_1^0$, welches in $\tilde{t}_1 \to c\tilde{\chi}_1^0$ produziert wurde, in ein Photon und ein leichtes Gravitino zerfällt. Frühe LHC-Ergebnisse mit 7 TeV Schwerpunktsenergie schränken den erlaubten Parameterraum für diese Zerfallskette bereits stark ein.

Im ADD-Modell betrachten wir Leptonenpaarproduktion im Szenario der asymptotisch sicheren Quantengravitation. Wir adaptieren Schranken aus 20-fb^{-1} CMS-Suchen nach anormalen Leptonenpaarproduktionsraten und geben Schranken an jene Skala an, die den Übergang von Newtons Kopplung in ein asymptotisch sicheres Fixpunktregime charakterisiert. Die Berechnung erfolgt mittels einer neuentwickelten Implementierung der relevanten Prozesse im Monte-Carlo-Generator PYTHIA 8.

Contents

Preface vii

Acknowledgements viii

I Particle physics in the LHC era 1

1 The Standard Model 3
1.1 Field content and interactions . . . 3
1.2 Broken flavor symmetry . . . 4
1.3 Higgs mass, hierarchy problem, and naturalness . . . 7
1.4 Dark Matter . . . 8
1.5 Summary . . . 9

2 Beyond the Standard Model 10
2.1 Symmetry, supersymmetry . . . 10
2.1.1 Fields and couplings in the MSSM . . . 11
2.1.2 Masses in the MSSM . . . 14
2.1.3 Local supersymmetry and massive gravitinos . . . 16
2.2 Large Extra Dimensions . . . 18
2.2.1 Compactified dimensions and the Planck scale . . . 18
2.2.2 Gravitons in $4+n$ dimensions . . . 20

II Stops and flavor at the LHC 23

3 Introduction: Sparticles as probes for flavor dynamics 25

4 Flavor in the MSSM 27
4.1 Constraints on the squark mass matrices . . . 27
4.2 The origin of flavor violation . . . 30
4.3 Minimal Flavor Violation . . . 31

5 Probing flavor with long-lived light stops 33
5.1 Stop masses . . . 33
5.1.1 Renormalization-group running . . . 33
5.1.2 LR mixing . . . 34
5.1.3 Higgs-mass corrections . . . 34
5.1.4 Direct-search limits . . . 35

5.2 FCNC stop decays . . . 36
5.3 Long-lived stops at the LHC—the $\tilde{t}_1\tilde{t}_1\bar{t}\bar{t}$-channel . . . 38
5.3.1 Stop kinematics and decays . . . 40
5.3.2 Cuts and event count . . . 44
5.3.3 Summary and recent data . . . 46

6 Subsequent gravitational neutralino decay **47**
6.1 FCNC stop decays revisited . . . 47
6.2 Neutralino decays . . . 51
6.3 Collider bounds from the $\tilde{t}_1\tilde{t}_1^*$-channel . . . 52
6.3.1 Exclusion limits for $\mathcal{B}(\tilde{t}_1 \to \tilde{\chi}_1^0 c)$ . . . 53
6.3.2 Implications for Y, $m_{3/2}$, and the lifetimes . . . 55
6.3.3 If there were a signal . . . 58

7 Conclusion of Part II **60**

III Drell-Yan leptons with asymptotically safe gravity **63**

8 Introduction: Gravity effects at colliders **65**

9 Asymptotic Safety **67**
9.1 A renormalizable theory of quantum gravity . . . 67
9.2 Approximate renormalization-group running . . . 69

10 Virtual gravitons in the s-channel **72**
10.1 Renormalization-scale choices . . . 73
10.2 KK sum with $\mu^2 = m^2$ . . . 74
10.3 KK sum with $\mu^2 = \hat{s} + m^2$—quenched approximation . . . 75
10.3.1 $\hat{s} + m^2$ propagator . . . 75
10.3.2 $\hat{s} - m^2 + \mathrm{i}\epsilon$ propagator . . . 76
10.4 Approximation-scheme dependence . . . 80

11 Drell-Yan leptons at the LHC **82**
11.1 Parton-level cross sections . . . 82
11.2 LHC phenomenology . . . 83
11.2.1 AS cross sections . . . 85
11.2.2 Approximation-scheme dependence . . . 86
11.2.3 Bounds from dilepton LHC data . . . 90
11.2.4 Comparison to real-graviton searches . . . 97

12 Conclusion of Part III **99**

Overall conclusion and outlook **101**

Appendices **104**

A Miscellaneous formulae **104**
A.1 Hadronic cross sections in the parton model—PDFs 104
A.2 Hadron-collider observables 105
A.3 RGE evolution of the soft sfermion mass terms 106
A.4 Phase-space integrals 107
A.5 Kaluza-Klein decomposition 107
A.6 Schwarzschild radius in LED 108
A.7 Kinematic functions in LED parton-level cross sections 108

B Simplified $\gamma\gamma\not{E}_T$ and $t\bar{t}\not{E}_T$ cuts **109**
B.1 DØ—$\gamma\gamma\not{E}_T$ channel 109
B.2 ATLAS—$\gamma\gamma\not{E}_T$ channel 109
B.3 ATLAS—$t\bar{t}\not{E}_T$ channel 110

C Additional Kaluza-Klein sums **111**
C.1 Quenched approximation—KK sum with $\mu^2 = m^2$ and $s \geq 0$ 111
C.2 Linear and quadratic approximation—seminumerical KK sums 111

D PYTHIA implementation of Asymptotic Safety **114**

Bibliography **117**

Preface

With the recent detection of a Higgs boson at the Large Hadron Collider (LHC) [1], a fundamental scalar particle was observed for the first time—a fundamental scalar within the Standard Model of particle physics (SM). The fact that this observation was possible is both comforting and puzzling. It is comforting, because this Higgs boson neatly fits into the SM, where it is a prediction of electroweak symmetry breaking. At the same time it is puzzling that the Higgs mass is small enough to be accessible at the LHC at all. If there is only the SM, radiative corrections to the Higgs mass are expected to be of the order of the Planck mass $\sim 10^{19}\,\text{GeV}$. The fact that the Higgs mass—and with it the entire SM spectrum—is only at the 100-GeV scale, despite these corrections, is widely regarded as unnatural and is known as the electroweak hierarchy problem. For its solution, new phenomena must emerge at the TeV scale explaining the smallness of the Higgs mass.

This thesis is about collider phenomenology in two well-known models beyond the SM, postulating such new phenomena: The Minimal Supersymmetric Standard Model (MSSM) implementing spacetime supersymmetry and the ADD model of large extra dimensions. The work is presented in three parts:

In the introductory Part I, we review the SM and discuss some of its major shortcomings, most notably the electroweak hierarchy problem and the unknown origin of flavor violation. We then introduce the MSSM and the ADD model.

In Part II, we turn to a specific topic in the MSSM. We discuss the prospects to explore a part of the MSSM's flavor structure through the flavor-changing charge-conserving stop decay $\tilde{t}_1 \to \tilde{\chi}_1^0 c$. We discuss the collider phenomenology of two scenarios where one may access the stop mixing structure through a measurement of macroscopic stop lifetimes. In the first scenario, stops produced in $pp \to \tilde{t}_1\tilde{t}_1\overline{tt}$ events decay to stable neutralinos. In the second scenario, neutralinos additionally are allowed to decays to photons and light gravitinos. We discuss bounds on the spectrum implied by experimental searches in the $\gamma\gamma\not{E}_T$ channel.

In Part III, we turn to the ADD model and discuss dilepton events assuming that gravity is asymptotically safe. With a newly developed implementation of the relevant processes to the Monte-Carlo generator PYTHIA 8, we discuss the approximation-scheme dependence of the leptons' invariant-mass distribution. From $20\,\text{fb}^{-1}$ of dilepton events measured by CMS in the LHC's 8-TeV run, we derive bounds on the transition scale and Planck scale associated with the high-energy regime of gravity.

*

The findings discussed in this thesis partly have been published in Ref. [2–4].

Acknowledgements

I like to thank my supervisor Gudrun Hiller for her guidance, for her contagious enthusiasm about physics, and for her valuable critical comments on earlier versions of this work. Further I would like to thank the TIII/TIV staff at TU Dortmund—my office colleagues Jong Soo Kim and Magdalena Zenglein in particular—for the pleasant company and numerous helpful discussions.

I want to thank Albert Knutsson and Hannes Jung for the hospitality and the insights into uPDFs and Monte-Carlo techniques I received during my stay at DESY, Hamburg, in the autumn of 2010. This stay was made possible in the course of an Analysis Centre studentship of the Helmholtz Alliance "PHYSICS AT THE TERASCALE".

Finally, I thank my family for all the support and the care packages I received. Especially, I thank my baby, Felix, for each smile he cast at me in the intense final phase of this work. Having written this, I owe special thanks to Marion, his mother, who took care for him when he was in no mood to smile.

Part I

Particle physics in the LHC era

1 The Standard Model

The Standard Model of particle physics (SM), dating back to the early 1970s [5], has been extremely successful in the description of high-energy interactions. At the time of writing, even after forty years of experimental tests, it successfully describes the vast majority of the phenomena observed in collider experiments. The SM's success climaxes in the triumphant observation of a particle consistent with the much sought-after Higgs particle independently at ATLAS and CMS [1], the general-purpose experiments at the Large Hadron Collider (LHC).

Despite of its success, the SM is plagued by several shortcomings that stimulated conjectures of numerous extended models beyond the SM (BSM models). Of the extensions, two prominent concepts are subject of this thesis: spacetime supersymmetry (SUSY) and quantum gravity at the electroweak energy scale. We introduce two explicit models incorporating these two concepts in Chapter 2, namely the Minimal Supersymmetric Standard Model (MSSM) and the model of large extra dimensions by Arkani-Hamed, Dimopoulos, and Dvali, the ADD model. Before, we shortly review the SM and three of its shortcomings in the following sections. The shortcomings discussed are the SM's unknown mechanism of flavor breaking, its hierarchy problem, and its lack of a realistic dark-matter candidate.

1.1 Field content and interactions

The SM is a quantum field theory of spin-1/2 fermions, spin-1 gauge bosons, and spin-0 bosons. It is a Yang-Mills theory and exhibits a local gauge symmetry associated with the gauge group

$$\mathcal{G}_{\mathrm{SM}} = \mathrm{SU}(3)_s \times \mathrm{SU}(2)_{\mathrm{L}} \times \mathrm{U}(1)_Y, \tag{1.1}$$

implying minimally coupled interaction terms of the fermions and bosons with the respective coupling constants g_s, g, and g'. The field content of the SM assigned to irreducible representations of $\mathcal{G}_{\mathrm{SM}}$ is enlisted in Table 1.1. The unitary groups constituting $\mathcal{G}_{\mathrm{SM}}$ represent three of the four known fundamental interactions: $\mathrm{SU}(3)_s$ describes strong interactions, and $\mathrm{SU}(2)_{\mathrm{L}} \times \mathrm{U}(1)_Y$ the unified electroweak (EW) interactions. The EW symmetry breaks down when the neutral Higgs field H^0 acquires a vacuum expectation value (VEV) v generating fermion masses through Yukawa-interaction Lagrange densities such as

$$\mathcal{L}_{\text{quark mass}} = -\lambda_d H \overline{q}_{\mathrm{L}} d_{\mathrm{R}} - \lambda_u H^* \circ \overline{q}_{\mathrm{L}} u_{\mathrm{R}} + \text{h.c.}, \tag{1.2}$$

exemplarily for the down and up-quarks with the respective Yukawa couplings λ_d and λ_u. Here and below, we denote with $A \circ B$ the antisymmetric product $A_\alpha \epsilon_{\alpha\beta} B_\beta$ (α, $\beta = 1, 2$), where $\epsilon_{\alpha\beta}$ is the two-dimensional totally antisymmetric tensor. In addition to

Fermions	Gauge rep. $(\mathscr{R}_c, \mathscr{R}_\mathrm{L})_Y$
Quarks	
$q^I_\mathrm{L} = \begin{pmatrix} u^I_\mathrm{L} \\ d^I_\mathrm{L} \end{pmatrix}$	$(\mathbf{3}, \mathbf{2})_{1/6}$
u^I_R	$(\bar{\mathbf{3}}, \mathbf{1})_{2/3}$
d^I_R	$(\bar{\mathbf{3}}, \mathbf{1})_{-1/3}$
Leptons	
$\ell^I_\mathrm{L} = \begin{pmatrix} \nu^I \\ e^I_\mathrm{L} \end{pmatrix}$	$(\mathbf{1}, \mathbf{2})_{-1/2}$
e^I_R	$(\mathbf{1}, \mathbf{1})_{-1}$

Vector bosons	Gauge rep. $(\mathscr{R}_c, \mathscr{R}_\mathrm{L})_Y$
Gluons	
G^μ_a	$(\mathbf{8}, \mathbf{1})_0$
Weak gauge bosons	
W^μ_i	$(\mathbf{1}, \mathbf{3})_0$
B-field	
B^μ	$(\mathbf{1}, \mathbf{1})_0$

Scalar bosons	Gauge rep. $(\mathscr{R}_c, \mathscr{R}_\mathrm{L})_Y$
Higgs doublet	
$H = \begin{pmatrix} H^+ \\ H^0 \end{pmatrix}$	$(\mathbf{1}, \mathbf{2})_{1/2}$

Table 1.1: Field content of the SM ($\mathscr{R}_x$: irreducible representation of gauge group $\mathrm{SU}(N)_x$, Y: hypercharge, $I = 1$–3: matter generation index; $i = 1$–3, $a = 1$–8: weak and colored gauge indices, $\mu = 0$–3: Minkowski index. Spinor indices are omitted.)

fermion masses, the masses of the EW gauge bosons are generated in the EW symmetry breaking. The resulting mass eigenstates are the W-bosons $W^\mu_\pm = 1/\sqrt{2}(W^\mu_1 \mp \mathrm{i}W^\mu_2)$, the Z-boson $Z^\mu = -\mathrm{s_W}B^\mu + \mathrm{c_W}W^\mu_3$, and the massless photon $A^\mu = \mathrm{c_W}B^\mu + \mathrm{s_W}W^\mu_3$ ($\mathrm{s_W}$ and $\mathrm{c_W}$ denote sin and cos of the weak-mixing angle θ_W). In Table 1.2 we enlist several SM parameters used in later parts of this thesis.

A first shortcoming of the SM is directly apparent in (1.1), the very first equation: Being a product of three groups, $\mathcal{G}_\mathrm{SM}$ allows for three independent couplings constants. If $\mathcal{G}_\mathrm{SM}$ were a subgroup of one single semi-simple group, the couplings were unified into only one coupling constant. (Yet, considering only the SM particle content for renomalization-group (RG) running, the three SM couplings never unify at a common grand unified theory (GUT) scale.) Considerable effort has been devoted to the development of such GUTs, see Ref. [6] for a review.

1.2 Broken flavor symmetry

Of each fermion field, the SM contains three copies—generations—that transform identically under $\mathcal{G}_\mathrm{SM}$, but differ in their Yukawa couplings, which are thus complex 3×3-matrices in general: Y_u, Y_d, and Y_ℓ.

Without the Yukawa fermion mass terms, the Lagrange density of the SM is invariant under global transformations that mix the three generation within each of the gauge

Symbol	Value	Ref.	Description
m_Z	$91.1876 \pm 0.0021\,\text{GeV}$	[7]	Z-boson pole mass
Γ_Z	$2.4952 \pm 0.0023\,\text{GeV}$	[7]	Z-boson width
m_W	$80.385 \pm 0.015\,\text{GeV}$	[7]	W-boson pole mass
m_t	$173.07 \pm 0.52 \pm 0.72\,\text{GeV}$	[7]	Top-quark pole mass
m_b	$4.78 \pm 0.06\,\text{GeV}$	[7]	Bottom-quark pole mass
$\alpha_{\text{em}}(m_Z)^{-1}$	127.994 ± 0.014	[7]	Inverse electromagnetic coupling constant at the m_Z scale; $\alpha_{\text{em}} = e^2/(4\pi)$ with $e = \text{s}_\text{W} g$.
$\text{s}_\text{W}{}^2(m_Z)$	0.23116 ± 0.00012	[7]	Squared sinus of the weak-mixing angle at the m_Z scale
G_F	$(1.1663787 \pm 0.0000006) \times 10^{-5}\text{GeV}^{-2}$	[7]	Fermi coupling constant
G_N	$(6.670837 \pm 0.00080) \times 10^{-39}\text{GeV}^{-2}$	[7]	Newton's gravitational constant
A	$0.823\,^{+0.012}_{-0.033}$	[8]	CKM Wolfenstein parameters
λ	$0.22457\,^{+0.00186}_{-0.00014}$	[8]	
$\bar{\rho}$	$0.1289\,^{+0.0176}_{-0.0094}$	[8]	
$\bar{\eta}$	$0.348\,^{+0.012}_{-0.012}$	[8]	

Table 1.2: Parameters used in several places throughout this work. Running quantities are in the $\overline{\text{MS}}$-scheme [9].

group representation, described mathematically in terms of the flavor group

$$\mathcal{G}_\text{flav} = \mathcal{G}_q \times \mathcal{G}_\ell, \tag{1.3}$$

where

$$\mathcal{G}_q = \text{SU}(3)_{q_\text{L}} \times \text{SU}(3)_{u_\text{R}} \times \text{SU}(3)_{d_\text{L}}, \qquad \mathcal{G}_\ell = \text{SU}(3)_{\ell_\text{L}} \times \text{SU}(3)_{e_\text{R}}. \tag{1.4}$$

The fermion fields in Table 1.1 can be assigned to fundamental representations of the SU(3) groups:

$$\begin{aligned} q_\text{L} &\sim (\mathbf{3},\mathbf{1},\mathbf{1})_q, & \ell_\text{L} &\sim (\mathbf{3},\mathbf{1})_\ell, \\ u_\text{R} &\sim (\mathbf{1},\mathbf{3},\mathbf{1})_q, & e_\text{R} &\sim (\mathbf{1},\mathbf{3})_\ell, \\ d_\text{R} &\sim (\mathbf{1},\mathbf{1},\mathbf{3})_q, \end{aligned} \tag{1.5}$$

where $(\mathscr{R}_{\boldsymbol{q_\text{L}}}, \mathscr{R}_{\boldsymbol{u_\text{R}}}, \mathscr{R}_{\boldsymbol{d_\text{R}}})_q$ and $(\mathscr{R}_{\boldsymbol{\ell_\text{L}}}, \mathscr{R}_{\boldsymbol{e_\text{R}}})_\ell$ denote representations of $\mathcal{G}_q$ and $\mathcal{G}_\ell$.

Fermion mass terms break this flavor symmetry, since exemplarily the down and up-quark mass terms (generalized to three generations, suppressing indices) transform according to

$$H \bar{q}_\text{L} \mathsf{Y}_d d_\text{R} \mapsto H \bar{q}_\text{L} \mathsf{U}^\dagger_{q_\text{L}} \mathsf{Y}_d \mathsf{U}_{d_\text{R}} d_\text{R}, \tag{1.6a}$$

$$H^* \circ \bar{q}_\text{L} \mathsf{Y}_u u_\text{R} \mapsto H^* \circ \bar{q}_\text{L} \mathsf{U}^\dagger_{q_\text{L}} \mathsf{Y}_u \mathsf{U}_{u_\text{R}} u_\text{R} \tag{1.6b}$$

under flavor transformations (U_X: unitary matrices, representations of the transformation on the X subspace).

Y_u and Y_d cannot be diagonalized at the same time by means of flavor transformations since they are generic, uncorrelated complex matrices in the SM. Flavor transformations account for only three of the four required unitary matrices ($\mathsf{U}_{q_\mathrm{L}}$, $\mathsf{U}_{u_\mathrm{R}}$, and $\mathsf{U}_{u_\mathrm{R}}$).

At best the quark Yukawa couplings can be brought to the following form by the means of flavor transformations:

$$\mathsf{Y}_u = \mathrm{diag}\,(\lambda_{u_I}), \qquad\qquad \mathsf{Y}_d = \mathsf{V}_\mathrm{CKM}\,\mathrm{diag}\,(\lambda_{d_I}), \tag{1.7}$$

where V_CKM is the Cabibbo-Kobayashi-Maskawa matrix (CKM matrix) [10]. We refer to this basis as the diagonal-Y_u basis. Experimentally, it has been established, that V_CKM is non-diagonal and complex valued. Explicitly it reads in the Wolfenstein parametrization [11]

$$\mathsf{V}_\mathrm{CKM} = \begin{pmatrix} 1-\lambda^2 & \lambda & A\lambda^3(\bar\rho - \mathrm{i}\bar\eta) \\ -\lambda & 1-\lambda^2/2 & A\lambda^2 \\ A\lambda^3(1-\bar\rho-\mathrm{i}\bar\eta) & -A\lambda^2 & 1 \end{pmatrix} + \mathcal{O}(\lambda^4), \tag{1.8}$$

with the parameters enlisted in Table 1.2. As a consequence of the non-diagonal structure of V_CKM, the generations of the mass eigenstates mix in charged-current interactions. There is no such mixture in the neutral-current interaction terms. Since V_CKM is strongly hierarchical and close to identity ($\lambda \simeq 0.2$), gauge and mass eigenstates are strongly aligned, and the flavor quantum numbers associated with the six quark mass eigenstates—up, down, strange, charm, bottom, and top—serve well as approximately conserved quantum numbers in interactions.

We focus on the quark sector above; though, an equivalent structure exists in the lepton sector, once the nonzero neutrino masses are accounted for. The equivalent to V_CKM in the lepton sector is the Pontecorvo-Maki-Nagawa-Sakata matrix V_PMNS [12]. Unlike V_CKM it is not close to diagonal, but apparently it exhibits a $\mathcal{O}(1)$ mixing [7, 13].

The SM does not predicted the structure of V_CKM which entails flavor violation and CP violation. It merely parametrizes it—just as the Yukawa couplings $\lambda_{u,d,e}$ and thus the fermion masses. Mechanisms with horizontal symmetries such as the Froggatt-Nielson mechanism [14] can be added to the SM to explain the flavor structure dynamically.

1.3 Higgs mass, hierarchy problem, and naturalness

The SM's Higgs particle is the particle associated upon quantization with the remnant massive degree of freedom h that is left of H after the spontaneous breakdown of the EW symmetry,

$$h(x) = \sqrt{2}\mathrm{Re}\, H_0(x) - v. \tag{1.9}$$

For the physical Higgs mass, $m_h = (91^{+30}_{-23})\,\mathrm{GeV}$ is favored by global fits on EW precision data [15] (excluding direct Higgs searches) and $m_h = (125.9 \pm 0.4)\,\mathrm{GeV}$ [7] by the recent findings of ATLAS and CMS.

The dynamics of the Higgs doublet H is implemented by the means of a ϕ^4-theory with quartic coupling λ, giving a Higgs mass of

$$m_h = \sqrt{2\lambda}v. \tag{1.10}$$

Large radiative corrections can be calculated for the Higgs mass. In fact, one-loop self-energy Feynman graphs induce quadratically divergent corrections to m_h. Explicitly the Higgs self energy at zero momentum $M^2_{hhf}(0)$, generated through a loop involving fermion f, is [16]

$$\begin{aligned} M^2_{hhf}(0) &= -2\lambda_f^2 \int \frac{d^4k}{(2\pi)^4} \left[\frac{1}{k^2 - m_f^2} + \frac{2m_f^2}{(k^2 - m_f^2)^2}\right] \\ &\sim \frac{2\lambda_f^2}{16\pi^2}\Big[\Lambda^2_{\mathrm{UV}} + m_f^2 \times (\text{logarithmic divergent and finite terms})\Big]. \end{aligned} \tag{1.11}$$

Here λ_f is the fermion's Yukawa coupling, and Λ_{UV} parametrizes the quadratic divergence of the $1/(k^2 - m_f^2)$-term.

Although the quadratic divergence in (1.11) can be absorbed via renormalization [17, 18], Λ_{UV} may be interpreted as a physical scale. Λ_{UV} can be taken as the energy scale where the SM ceases to describe nature and is to be replaced by a higher theory. Within a GUT setup this can be the unification scale. Ultimately, the Planck scale $\mathrm{M_{PL}} = 1/\sqrt{G_\mathrm{N}} \sim \mathcal{O}(10^{19}\,\mathrm{GeV})$, the scale where quantum-gravity effects presumably can no longer be neglected, is such a scale.

With $\Lambda_{\mathrm{UV}} = \mathrm{M_{PL}}$, a hierarchy problem emerges [19, 20]. Why is m_h—and with it the scale of EW physics—so much smaller than $\mathrm{M_{PL}}$? The magnitude of the radiative corrections is set by $\mathrm{M^2_{PL}}$. Therefore, the bare $m^2_{h,0}$ must be of the same order so that the tree-level mass and its corrections cancel at a the precision of more than 30 digits to yield $m_h^2 \approx (100\,\mathrm{GeV})^2$. Quadratically divergent Higgs loops $\propto \lambda = m_h^2/(2v^2)$ even potentiate this problem. Even if the divergence is removed, $M^2_{hhf}(0)$ is sensitive through the m_f^2-term in (1.11) to the mass of any new fermion, that may exists in high-scale theories.

The fine-tuning required to yield a Higgs mass as low as the EW scale is regarded as unnatural, where several definitions of naturalness are discussed in the literature [20, 21]. Following Ref. [21], a small number such as m_h—viewed at a much higher energy scale—can be regarded as natural if setting it to zero increases the symmetry of the system under consideration, which is not the cases for SM Higgs particle [21].

1.4 Dark Matter

So far we discussed intrinsic deficiencies of the SM. Now we come to an astrophysical phenomenon the SM fails to explain: the abundance of Dark Matter.

It is well established that visible baryonic matter only constitutes a small fraction ($\sim 15\%$) of the current matter density in the universe [22]. The bulk of matter is non-luminescent and non-absorbing—i.e. dark—and experiences only little self interactions. Candidate particles for dark matter are categorized dependent on how relativistic they were at the beginning of structure formation. They are hot Dark Matter (HDM) if their mass was negligible compared to the temperature, i.e., $p = 1/3\varrho$ (where p and ϱ are the associated momentum and energy densities). They are cold Dark Matter (CDM) if they were non-relativistic, i.e. $p \approx 0$.

The obvious SM dark-matter particles are neutrinos ν^I. SM neutrinos are HDM yielding a current relative matter density of [7, 23]

$$\Omega_\nu \mathsf{h}^2 = \varrho_\nu / \varrho_{\text{crit}} \mathsf{h}^2 \approx \frac{m_\nu^{\text{tot}}}{94\,\text{eV}} \qquad \text{with} \qquad m_\nu^{\text{tot}} = 2\sum_{I=1}^{3} m_\nu^I. \tag{1.12}$$

Here ϱ_{crit} is the energy density corresponding to a flat Friedmann-Robertson-Walker (FRW) universe, and $\mathsf{h} = 0.673 \pm 0.12$ [24] is the the Hubble constant in units of $100\,\text{km}/(\text{s}\,\text{Mpc})$. The relation in (1.12) would lead to a realistic dark-matter density with $\mathcal{O}(\text{eV})$ neutrino masses; however, a dominating HDM component is known to hinder a realistic structure formation [25]. Hence, dark matter is generally assumed to be dominantly cold. Assuming a flat FRW universe whose late expansions is dominated by CDM and a cosmological constant Λ (the ΛCDM model), a recent analysis of the cosmic microwave background by the Planck experiment found that the current relative densities of baryonic matter and non-baryonic CDM are [24]

$$\Omega_b \mathsf{h}^2 = 0.02205 \pm 0.00028, \qquad \Omega_{\text{CDM}} \mathsf{h}^2 = 0.1199 \pm 0.027, \tag{1.13}$$

yielding a total matter density of $\Omega_m = 0.315 \pm 0.017$ [24]. A typical CDM particle χ has a mass of 10 GeV to a few TeV [26], and gives a relative density of [27]

$$\Omega_\chi \mathsf{h}^2 \simeq \frac{0.1\,\text{pb}}{\langle \sigma_A v \rangle}, \tag{1.14}$$

where σ_A is the annihilation cross section of a $\chi\chi$ pair to SM particles and $0 \leq v < 1$ their velocities in their center-of-mass system. $\langle\cdot\rangle$ denotes thermal averaging. Note that in theories with enlarged particle contents—such as SUSY–, this formula becomes more involved, most noteworthy, if there is significant co-annihilation of χs with other particles of similar masses (cf. Ref. [28], e.g.).

Despite the success of the description of large-scale structure formation, the standard ΛCDM theory is known to yield unrealistic predictions for sub-galactic structures [29]. This and other issues are found to be resolved if Dark Matter is warm (WDM) [30]. WDM is cooled-down HDM, where HDM is prototyped by the SM neutrinos [31]: Any

HDM candidate x that decouples from the photons' thermal bath prior to the neutrinos has a black-body temperature T_x given by

$$T_x = \left(\frac{10.75}{g^*(T_D^x)}\right)^{1/3} T_\nu. \tag{1.15}$$

Here T_ν is the neutrinos' temperature, and $g^*(T_D^x)$ is the effective number of relativistic degrees of freedom at T_D^x, the temperature where x decouples (see Ref. [32] for $g^*(T)$ in the SM). T_x is smaller than T_ν (x is WDM) if any particle species annihilates to photons between T_D^x and T_D^ν.

A recent analysis of Lyman-alpha flux power spectra constrains WDM masses to values smaller than a 4 keV [33].

1.5 Summary

Despite its success, the SM would benefit from improvements in various aspects: There could be grand unification that would reduce the number of independent gauge couplings. The SM's approximate flavor symmetry is not understood, and its breaking accounts for most of the free parameters in the theory (fermion masses and mixing parameters). The mass of the SM's sole fundamental scalar, the Higgs boson, is sensitive to high-energy dynamics, and it is unclear why the Higgs mass is such small. The SM has no CDM candidate that would explain the late history of the universe.

2 Beyond the Standard Model

In this chapter, we introduce two prominent BSM models, solving the hierarchy or naturalness problem in two different approaches: by introducing SUSY or quantum gravity at the EW scale.

Even if they were no solution to the hierarchy problem—if their characteristic energy scales were much higher than the EW scale—both mechanisms are attractive additions to the SM on their own. Most noteworthy SUSY, enlarging the symmetry of the theory.

2.1 Symmetry, supersymmetry

In theoretical physics, finding a symmetry often leads to a massive reduction of a problem's complexity. Symmetries, and the underlying mathematical concept of groups, conversely have been employed very successfully in the construction of theories. Prominent examples in the context of particle physics are "the eightfold way" of the baryons and mesons, the theory of Relativity, and the gauge interactions of the SM.

With the success of describing hadrons of equal spin and their interactions with the help of product representations of two or three SU(N)s, efforts have been made to unite the interactions of different spin states with the same measures. Certain success have been found in the use of the **35** representation of SU(6)[2] to describe pseudoscalar bosons and vector bosons simultaneously, see Ref. [34] for example. The attempts to develop a fully relativistic theory describing states of different spin simultaneously in one representation faced an end in 1967, though, when Coleman and Mandula proved [35] that the most general symmetry Lie group of the S-matrix, the scattering matrix describing relativistic particle interactions, is a direct product of the Poincaré group and internal symmetry groups, where the latter—such as the SM's gauge group—act on the spin and mass eigenstates of the former. The states that would take part in relativistic scattering are required to have a distinct spin eigenvalue in addition to a mass; no symmetry can enforce uniform interactions of different-spin-valued states.

A breakthrough was achieved when Wess and Zumino proposed a model with spacetime supersymmetry [36], circumventing Coleman's and Mandula's constraint on the symmetry of the S-matrix [37]. Spacetime supersymmetry is realized when the Lie algebra of the Poincaré group is extend to a graded algebra by adding N sets of generators Q^i and $\bar{Q}^i$ ($i = 1,\ldots,N$) that satisfy anticommutation relations contrary to the generators $J^{\mu\nu}$ and P^μ of the Poincaré algebra that satisfy commutation relations. In the simplest case with only one Q-$\bar{Q}$ pair ($N = 1$ superymmetry), the (super)multiplets belonging to the irreducible representations of the supergroup would comprise two spin states differing by $\Delta s = 1/2$, with matching degrees of freedom. For $N \neq 1$, the representations contain states with $\Delta s = N/2$.

Hence, in a supersymmetric theory[1] several states of different spin—bosonic and a fermionic—can be described uniformly in terms of a single supermultiplet. Most elegantly, a set of fields belonging to one supermultiplet is arranged to form a single superfield, labeled according to the highest spin state it comprises. Important phenomenologically are left-chiral superfields ($s = 0,\, 1/2$), vector superfields ($s = 1/2,\, 1$), and tensor superfields ($s = 3/2,\, 2$), for $N = 1$ SUSY respectively.

A first striking implication, obvious in the superfield formulation, is that in a supersymmetric theory, all members of a supermultiplet have the same mass. Unfortunately, the SM is not supersymmetric apparently: not only does it comprise more fermion than boson species; also, both types of particles have different masses and in general interact completely differently. Yet, if the SM were supersymmetric, its hierarchy problem instantly would be solved: For every massive fermion constituting a quadratically divergent loop to the Higgs self energy, a corresponding loop from a boson belonging to the same supermultiplet would contribute an equivalent opposite-signed correction; both contributions would cancel exactly [36, 39].

Though the SM is not supersymmetric, it still may be the light remnants of a broken supersymmetric theory. If the heavier rest of the spectrum were not too heavy (at the TeV-scale), the radiative corrections to the Higgs mass

$$\Delta m_h^2 \propto m_f^4 G_F \ln(m_{\tilde{f}}/m_f) \tag{2.1}$$

may still be small enough to be acceptable (here $m_{\tilde{f}}$ denotes the mass of a heavy supersymmetric partner of SM fermion f—see Section 5.1.3 for more details). Technically, the Lagrange density describing the full theory may be split into a supersymmetric part ($\mathcal{L}_{\text{susy}}$) and a supersymmetry-breaking one ($\mathcal{L}_{\text{soft}}$),

$$\mathcal{L} = \mathcal{L}_{\text{susy}} + \mathcal{L}_{\text{soft}}. \tag{2.2}$$

$\mathcal{L}_{\text{soft}}$ would contain couplings that lift the unobserved part of the spectrum above the current experimental reach. As the notation suggests, these SUSY breaking couplings are generally chosen to be "soft", i.e. superrenormalizable, so that SUSY is restored at renormalization scales much higher than the typical energy scale of $\mathcal{L}_{\text{soft}}$.

In the next two sections we introduce the MSSM, the simplest ($N = 1$) globally supersymmetric extension of the SM, and establish the notation we use in later parts of this work. For a detailed introduction see Ref. [16, 40], for example.

2.1.1 Fields and couplings in the MSSM

The MSSM is the minimal supersymmetric extension of the SM in that its particle content is extended in a minimal way to realize a $N = 1$ supersymmetric theory. For every SM particle, exactly one extra particle—a sparticle—is introduced. The partners' spins differ by 1/2, but both transform identically under the SM's gauge group $\mathcal{G}_{\text{SM}}$. Only, as the economic construction of the SM's fermion mass terms with a single Higgs doublet H_u cannot be supersymmetrized, a second Higgs doublet H_d is added to MSSM.

[1] First supersymmetric field theories on 4-dimensional spacetime were formulated in Ref. [38].

The MSSM's field content is enlisted in Table 2.1, following the charge convention of Ref. [41].

Besides kinetic terms and minimally coupled interaction terms, the MSSM's $\mathcal{L}_{\text{susy}}$ contains gauge invariant couplings of all chiral superfields to the Higgs superfields, implemented in terms of a superpotential

$$\mathcal{W} = \mu \mathsf{H}_u \circ \mathsf{H}_d - \mathsf{H}_d \circ \mathsf{L}^I (\mathsf{Y}_e)^{IJ} \mathsf{E}^J - \mathsf{H}_d \circ \mathsf{Q}^I (\mathsf{Y}_d)^{IJ} \mathsf{D}^J - \mathsf{Q}^I \circ \mathsf{H}_u (\mathsf{Y}_u)^{IJ} \mathsf{U}^J. \tag{2.3}$$

Like in the previous chapter, $A \circ B$ denotes the antisymmetric product $A_\alpha \epsilon_{\alpha\beta} B_\beta$ (α, $\beta = 1, 2$) and the $\mathsf{Y}_{e/d/u}$ denote the SM Yukawa coupling matrices. Capital indices I, J, $K = 1$–3 labels the matter generation, and μ is a new, generally complex-valued, parameter of mass dimension one.

From the fields in Table 2.1, more gauge-invariant trilinear (bilinear) terms similar to those appearing in (2.3) can be formed, $\lambda'^{IJK} \mathsf{L}^I \circ \mathsf{Q}^J \mathsf{D}^K$ or $\lambda''^{IJK} \mathsf{U}^I \mathsf{D}^J \mathsf{D}^K$ for example. To prohibit a proton (p) decay[2] that would be possible at tree-level if these lepton- and baryon-number violating terms were present, a new conserved quantum number, matter parity M_p, is postulated [43]. With matter-parity assignments of the superfields as enlisted in Table 2.1, $\mathcal{W}$ in (2.3) is the most general renormalizable, gauge-invariant, M_p-conserving superpotential. For the components of a superfield of given matter parity M_p, a R-parity $R_p = M_p \cdot (-1)^{2s}$ is usually defined [44], where s denotes the spin of the component. With this definition, all SM fields (and the additional scalar H_d) have positive R-parity, while all sparticles have negative R-parity. Most notably, M_p conservation and therefore R-parity conservation imply that sparticles only can interact in pairs with SM particles. They only can be produced pair-wise and a single sparticle can decay to SM particles only if it emits an odd number of lighter sparticles in addition. As a consequence of the latter, there must be a stable lightest supersymmetric particle (LSP).

SUSY breaking is merely parametrized in the most general weak-scale MSSM by the means of a $\mathcal{L}_{\text{soft}}$. This results in a large number of new couplings, added to the model through $\mathcal{L}_{\text{soft}}$. All possible superrenormalizable operators of squarks, sleptons, Higgs fields, and the spin-1/2 gaugino fields not spoiling gauge symmetry and R-parity conservation are allowed to appear in $\mathcal{L}_{\text{soft}}$. Explicitly it reads

$$\begin{aligned}
\mathcal{L}_{\text{soft}} = {} & \tilde{\ell}^*_{\text{L},I} \, (\mathsf{m}^2_L)_{IJ} \, \tilde{\ell}_{\text{L},J} + \tilde{e}^*_{\text{R},I} \, (\mathsf{m}^2_E)_{IJ} \, \tilde{e}_{\text{R},J} && \text{(2.4a)} \\
& + \tilde{q}^*_{\text{L},I} \, (\mathsf{m}^2_Q)_{IJ} \, \tilde{q}_{\text{L},J} + \tilde{u}^*_{\text{R},I} \, (\mathsf{m}^2_U)_{IJ} \, \tilde{u}_{\text{R},J} + \tilde{d}^*_{\text{R},I} \, (\mathsf{m}^2_D)_{IJ} \, \tilde{d}_{\text{R},J} && \text{(2.4b)} \\
& + m^2_{h_u} |h_u|^2 + m^2_{h_d} |h_d|^2 + m^2_{12} \, h_u \circ h_d && \text{(2.4c)} \\
& + h_d \circ \tilde{\ell}_{\text{L},I} (\mathsf{A}_\ell)_{IJ} \tilde{e}^*_{\text{R},J} + h_d \circ \tilde{q}_{\text{L},I} (\mathsf{A}_d)_{IJ} \tilde{d}^*_{\text{R},J} + \tilde{q}_{\text{L},I} \circ h_u (\mathsf{A}_u)_{IJ} \tilde{u}^*_{\text{R},J} && \text{(2.4d)} \\
& + \frac{1}{2} M_1 \, \lambda^B \lambda^B + \frac{1}{2} M_2 \, \lambda^W_i \lambda^W_i + \frac{1}{2} M_3 \, \lambda^G_a \lambda^G_a && \text{(2.4e)} \\
& + \text{h.c.} && \text{(2.4f)}
\end{aligned}$$

The soft terms can be categorized into scalar mass terms (2.4a)–(2.4c), Yukawa-like scalar trilinear interaction terms (2.4d), and bilinear gaugino Majorana mass terms

[2] $\tau_p > 2.1 \times 10^{29}$ years [42]

Left-chiral superfield	Weyl-spinor component	Scalar component	Gauge rep. $(\mathscr{R}_c, \mathscr{R}_\mathrm{L})_Y$	Matter parity M_p
	Quarks	Squarks		
Q^I	$q_\mathrm{L}^I = \begin{pmatrix} u_\mathrm{L}^I \\ d_\mathrm{L}^I \end{pmatrix}$	$\tilde{q}_\mathrm{L}^I = \begin{pmatrix} \tilde{u}_\mathrm{L}^I \\ \tilde{d}_\mathrm{L}^I \end{pmatrix}$	$(\mathbf{3},\mathbf{2})_{1/6}$	-1
U^I	u_R^{Ic}	$\tilde{u}_\mathrm{R}^{I*}$	$(\bar{\mathbf{3}},\mathbf{1})_{-2/3}$	-1
D^I	d_R^{Ic}	$\tilde{d}_\mathrm{R}^{I*}$	$(\bar{\mathbf{3}},\mathbf{1})_{1/3}$	-1
	Leptons	Sleptons		
L^I	$\ell_\mathrm{L}^I = \begin{pmatrix} \nu^I \\ e_\mathrm{L}^I \end{pmatrix}$	$\tilde{\ell}_\mathrm{L}^I = \begin{pmatrix} \tilde{\nu}^I \\ \tilde{e}_\mathrm{L}^I \end{pmatrix}$	$(\mathbf{1},\mathbf{2})_{-1/2}$	-1
E^I	e_R^{Ic}	$\tilde{e}_\mathrm{R}^{I*}$	$(\mathbf{1},\mathbf{1})_{1}$	-1
	Higgsinos	Higgs fields		
H_u	$\tilde{H}_u = \begin{pmatrix} \tilde{H}_u^+ \\ \tilde{H}_u^0 \end{pmatrix}$	$H_u = \begin{pmatrix} H_u^+ \\ H_u^0 \end{pmatrix}$	$(\mathbf{1},\mathbf{2})_{1/2}$	1
H_d	$\tilde{H}_d = \begin{pmatrix} \tilde{H}_d^0 \\ \tilde{H}_d^- \end{pmatrix}$	$H_d = \begin{pmatrix} H_d^0 \\ H_d^- \end{pmatrix}$	$(\mathbf{1},\mathbf{2})_{-1/2}$	1

Vector superfield	4-vector component	Weyl-spinor component	Gauge rep. $(\mathscr{R}_c, \mathscr{R}_\mathrm{L})_Y$	Matter parity M_p
	Gluons	Gluinos		
V_a^G	G_a^μ	λ_a^G	$(\mathbf{8},\mathbf{1})_0$	0
	Weak gauge bosons	Winos		
V_i^W	W_i^μ	λ_i^W	$(\mathbf{1},\mathbf{3})_0$	0
	B-field	Bino		
V^B	B^μ	λ^B	$(\mathbf{1},\mathbf{1})_0$	0

Table 2.1: Field content of the MSSM ($\mathscr{R}_x$: irreducible representation of gauge group $\mathrm{SU}(N)_x$, Y: hypercharge, $I = 1$–3: matter generation index; $i = 1$–3, $a = 1$–8: weak and colored gauge indices, $\mu = 0$–3: Minkowski index. Spinor indices are omitted.)

(2.4e). While the scalar mass terms are Hermitean, the other parameters are complex in general.

A dynamical SUSY-breaking mechanism typically reduces the number of newly introduced couplings to a hand full. Exemplarily, in gauge-mediated SUSY breaking (GMSB) [45], SUSY is broken in a hidden sector of the Lagrangian, and the breaking is mediated on the loop level to the visible MSSM sector through messenger fields transforming non-trivially under $\mathcal{G}_{\mathrm{SM}}$. In the minimal GMSB model (mGMSB), all gaugino, squark, and slepton mass matrices are determined at the energy scale of mediation by their $\mathcal{G}_{\mathrm{SM}}$ structure and a common mass scale M_s. In total the number of new parameters is reduced from 104 to five in this model [46].

Due to the large number of soft SUSY-breaking terms, the mass structure of the MSSM is considerable more complex than that of the SM. We list the expressions relevant for this thesis in the following.

2.1.2 Masses in the MSSM

Like in the SM, the masses of the SM particles are generated through a spontaneous breakdown of the EW gauge symmetry: Both neutral bosonic Higgs fields, H_u^0 and H_d^0, acquire VEVs denoted as v_u and v_d, whose ratio is denoted as

$$\tan\beta = \frac{v_u}{v_d}. \tag{2.5}$$

Gauge bosons and SM fermions

The nonzero masses of the SM gauge bosons and fermions are

$$\begin{aligned} m_W &= \frac{g}{2}(v_u^2 + v_d^2)^{\frac{1}{2}}, & m_Z &= \frac{g}{2\mathrm{c_W}}(v_u^2 + v_d^2)^{\frac{1}{2}}, & & \\ m_e^I &= \frac{v_d}{\sqrt{2}}\lambda_e^I, & m_d^I &= \frac{v_d}{\sqrt{2}}\lambda_d^I, & m_u^I &= \frac{v_u}{\sqrt{2}}\lambda_u^I \end{aligned} \tag{2.6}$$

for the W-bosons, Z-bosons, charged leptons, down-type quarks, and up-type quarks, respectively. The $\lambda_{e/d/u}^I$ are the real diagonal entries of the diagonalized Yukawa couplings.

Higgs bosons

If the MSSM's extended Higgs sector is CP-conserving, it contains two massive scalar Higgs bosons h and H, one massive pseudoscalar Higgs boson A and two massive charged Higgs bosons $H^{\pm}$.

The neutral scalar mass eigenstates h and H are obtained through a rotation,

$$H = \quad (\sqrt{2}\mathrm{Re}\, H_d^0 - v_d)\cos\alpha + (\sqrt{2}\mathrm{Re}\, H_u^0 - v_u)\sin\alpha \tag{2.7a}$$

$$h = -(\sqrt{2}\mathrm{Re}\, H_d^0 - v_d)\sin\alpha + (\sqrt{2}\mathrm{Re}\, H_u^0 - v_u)\cos\alpha, \tag{2.7b}$$

where $m_h < m_H$ by definition. Only two additional MSSM parameters are necessary to parametrize all five Higgs bosons masses at tree-level in addition to m_Z, g, and g';

refer to Ref. [16] for explicit formulae. Remarkably, the tree-level mass of the light neutral Higgs boson h is smaller than m_Z. However, it is subject to substantial positive radiative corrections dominated by the 3rd generation of (s)fermions, see Section 5.1.

The recent discovery of a state consistent with an SM Higgs at the LHC with a mass of roughly 125 GeV [1] suggests that the MSSM Higgs sector is in the decoupling limit [47] where h couples exactly like the SM Higgs. In this limit, defined by $m_A \gg m_z$, the angles α and β fulfill $\cos^2(\beta-\alpha) \approx 0$, and the tree-level Higgs masses are [47]:

$$m_h^2 \approx m_Z^2 \cos^2 2\beta \tag{2.8a}$$

$$m_H^2 \approx m_A^2 + m_Z^2 \sin^2 2\beta \tag{2.8b}$$

$$m_{H^\pm}^2 \approx m_A^2 + m_W^2. \tag{2.8c}$$

Neutralinos, charginos, and gluinos

After EW symmetry breaking, the eight EW gaugino and higgsino Weyl spinors mix to four neutral Majorana spinors (neutralinos) and two charged Dirac spinors (charginos), denoted as $\tilde{\chi}_i^0$ ($i = 1$–4) and $\tilde{\chi}_i^\pm$ ($i = 1$–2). Here and below, mass eigenstates states are labeled in mass order, that is $m_{\tilde{\chi}_1^0} \leq m_{\tilde{\chi}_2^0} \leq \cdots$ exemplary.

The mass eigenvalues are obtained through the diagonalization of the (2×2)-dimensional chargino mass matrix

$$\mathcal{M}_{\tilde{\chi}^\pm} = \begin{pmatrix} M_2 & g\frac{v_u}{\sqrt{2}} \\ g\frac{v_d}{\sqrt{2}} & \mu \end{pmatrix} \tag{2.9}$$

and of the (4×4)-dimensional neutralino mass matrix

$$\mathcal{M}_{\tilde{\chi}^0} = \begin{pmatrix} M_1 & 0 & -g'\frac{v_d}{2} & g'\frac{v_u}{2} \\ 0 & M_2 & g\frac{v_d}{2} & -g\frac{v_u}{2} \\ -g'\frac{v_d}{2} & g\frac{v_d}{2} & 0 & -\mu \\ g'\frac{v_u}{2} & -g\frac{v_u}{2} & -\mu & 0 \end{pmatrix}, \tag{2.10}$$

where—for later reference—the unitary neutralino diagonalization matrix Z_N is defined by

$$\mathsf{Z}_N^* \mathcal{M}_{\tilde{\chi}^0} \mathsf{Z}_N^\dagger = \operatorname*{diag}_{i=1\text{–}4}(m_{\tilde{\chi}_i^0}). \tag{2.11}$$

Note that both mass matrices simplify considerably when the $|M_i|$ and $|\mu|$ are much larger than $\mathcal{O}(m_Z)$ as the off-diagonal entries (blocks) become negligible. In this case, one type of the gauge states dominates each mass eigenstate and the latter is bino-like (neutralinos only), wino-like, or higgsino-like with the respective masses $|M_1|$, $|M_2|$, and $|\mu|$. Throughout this thesis we assume that $\mathcal{M}_{\tilde{\chi}^0}$ and $\mathcal{M}_{\tilde{\chi}^\pm}$ are real matrices.

Since it interacts weakly and usually has a mass of a few 100 GeV, a neutralino LSP is an appealing candidate for cold dark matter.

Unaffected from EW symmetry breaking, the gluino's mass is given by the soft mass M_3. In the phenomenological application in Part II, we switch to the standard notation and denote the gluino as $\tilde{g}$ with mass $m_{\tilde{g}}$.

Up-type squarks

The terms contributing to three generations of left-handed and right-handed up-type squarks can be collected in a Hermitean (6×6)-dimensional squark mass matrix

$$\mathcal{M}_u^2 = \begin{pmatrix} \mathcal{M}_{u,\mathrm{LL}}^2 & \mathcal{M}_{u,\mathrm{LR}}^2 \\ \left(\mathcal{M}_{u,\mathrm{LR}}^2\right)^\dagger & \mathcal{M}_{u,\mathrm{RR}}^2 \end{pmatrix} \tag{2.12}$$

to form $\mathcal{L}_{\tilde{u}\text{-mass}} = -\tilde{\boldsymbol{u}}^\dagger \mathcal{M}_u^2 \tilde{\boldsymbol{u}}$, with $\tilde{\boldsymbol{u}} = (\tilde{u}_\mathrm{L}, \tilde{c}_\mathrm{L}, \tilde{t}_\mathrm{L}, \tilde{u}_\mathrm{R}, \tilde{c}_\mathrm{R}, \tilde{t}_\mathrm{R})^T$. The (3×3)-dimensional submatrices read

$$\mathcal{M}_{u,\mathrm{LL}}^2 = \mathsf{m}_Q^2 + \mathsf{m}_u \mathsf{m}_u^\dagger - m_Z^2 \cos 2\beta \frac{{\mathrm{s_W}}^2 - 3{\mathrm{c_W}}^2}{6} \mathbb{1}_{3\times3} \tag{2.13a}$$

$$\mathcal{M}_{u,\mathrm{RR}}^2 = \mathsf{m}_U^2 + \mathsf{m}_u^\dagger \mathsf{m}_u + m_Z^2 \cos 2\beta \frac{2{\mathrm{s_W}}^2}{3} \mathbb{1}_{3\times3} \tag{2.13b}$$

$$\mathcal{M}_{u,\mathrm{LR}}^2 = -\frac{v_u}{\sqrt{2}} \mathsf{A}_u^* - \mu \mathsf{m}_u \cot\beta, \tag{2.13c}$$

where $\mathsf{m}_u = \frac{v_u}{\sqrt{2}} \mathsf{Y}_u^*$ is the up-type quark mass matrix yielding the quark masses in (2.6) upon diagonalization. For down-type squarks and charged selectrons, mass matrices $\mathcal{M}_d^2$ and $\mathcal{M}_\ell^2$ can be arranged equivalently, see Ref. [16] for instance.

Starting with Yukawa matrices in the diagonal-Y_u basis [cf. (1.7)], the quark mass matrices can be diagonalized with the transformation

$$(d_\mathrm{L}^I,\, \tilde{d}_\mathrm{L}^I) \mapsto (d_\mathrm{L}'^I,\, \tilde{d}_\mathrm{L}'^I) = (\mathsf{V}_{\mathrm{CKM}}^{*JI} d_\mathrm{L}^J,\, \mathsf{V}_{\mathrm{CKM}}^{*JI} \tilde{d}_\mathrm{L}^J). \tag{2.14}$$

The basis obtained, with diagonal quark mass matrices and generally non-diagonal squark mass matrices, is known as the super-CKM basis [48]. As further discussed in Section 4.1, the off-diagonal entries of the (3×3)-dimensional blocks in (2.13) are experimentally found to be severely suppressed in the super-CKM basis. It is therefore justified not to denote the squark mass eigenstates uniformly as $\tilde{u}_i$ or $\tilde{d}_i$ with $i = 1$–6 but instead to retain the knowledge about the dominant flavor by naming the mass eigenstates $\tilde{u}_i$, $\tilde{c}_i$, $\tilde{t}_i$, $\tilde{d}_i$, $\tilde{s}_i$, $\tilde{b}_i$ with $i = 1, 2$. For each squark flavor the labels are assigned in mass order so that $m_{\tilde{t}_1} \leq m_{\tilde{t}_2}$, exemplarily. The unitary matrix used to diagonalize the super-CKM $\mathcal{M}_u^2$ is denoted as Z_u:

$$\mathsf{Z}_u^\dagger \mathcal{M}_u^2 \mathsf{Z}_u = \mathrm{diag}(m_{\tilde{u}_1}, m_{\tilde{c}_1}, m_{\tilde{t}_1}, m_{\tilde{u}_2}, m_{\tilde{c}_2}, m_{\tilde{t}_2}). \tag{2.15}$$

2.1.3 Local supersymmetry and massive gravitinos

The MSSM just introduced bases on a global supersymmetry extending a global Poincaré symmetry, the symmetry of Special Relativity. Since Special Relativity is known to be superseded by General Relativity that bases on a local Poincaré symmetry,

it is natural to replace the global supersymmetry by a local one, building a theory of supergravity, see Ref. [49] for example.

In General Relativity, the invariance under local Poincaré transformations implies the existence of a massless spin-2 state, a graviton. (At least in the weak-field limit, since it is unclear yet, how an ultimate theory of quantum gravity looks like.) In $N = 1$ supersymmetry, this graviton will be accompanied by a massless spin-3/2 superpartner, a gravitino, described by a vector Majorana spinor $\tilde{G}^{\mu}$.

With supergravity, a mechanism to implement spontaneous SUSY breaking into a phenomenologically realistic model containing the MSSM emerges: Spontaneous SUSY breaking may be introduce a gauge singlet chiral superfield Φ whose auxiliary component F is allowed to acquire a VEV at a high renormalization scale (F-term SUSY breaking). This breaking is then propagated to the visible sector—the sector containing the SM—through supergravity couplings, generating the effective, SUSY-breaking terms of $\mathcal{L}_{\text{soft}}$. Analoguous to the Goldstone boson in the Higgs mechanism, a degree of freedom remains unaffected by the breaking, which is called Goldstino owing to its fermionic nature. In the case considered here it is the spin-1/2 component of Φ. Also analogous to the Higgs mechanism, in this superhiggs mechanism [50], the Goldstino is eaten by a massless gauge particle which becomes massive thereafter: the Gravitino. Its mass is given by

$$m_{3/2} = \mathrm{M_{PL}} \mathrm{e}^{-\langle \mathcal{G} \rangle / \mathrm{M_{PL}^2}}, \tag{2.16}$$

where $\langle \mathcal{G} \rangle$ is the VEV of the Kähler potential $\mathcal{G}$ of the theory, one of only two functions necessary to describe the dependence of the most general supergravity Lagrange density on the superfields—cf. Ref. [49] for details, e.g.

Depending on the exact breaking mechanism, $m_{3/2}$ can be very small—this is the case we focus on in later parts of this thesis. If $\tilde{G}$ is to serve as a warm-dark-matter candidate, $m_{3/2}$ is in fact constrained to values smaller than 4 keV [33].

By virtue of supersymmetric equivalence theorem [51] (see also Ref. [16]), a light gravitino's interactions are dominated by its spin-1/2 Goldstino component at center-of-mass energies much larger than $m_{3/2}$, with couplings $\sim (m_{3/2} \overline{\mathrm{M}}_{\mathrm{PL}})^{-1}$.

2.2 Large Extra Dimensions

In the supersymmetric extensions such as the MSSM, the SM's EW hierarchy problem—or the implied naturalness problem—is tackled by introducing new particles to weaken the fine-tuning. We now turn to a radically different option: To remove the hierarchy problem by removing the hierarchy.

In Ref. [52], Arkani-Hamed, Dimopoulos, and Dvali (ADD) advertise this approach by proposing that $\mathrm{M_{PL}} = 1/\sqrt{G_\mathrm{N}} \sim 10^{16}\,\mathrm{TeV}$ is not the true scale of quantum gravity, but that this scale is in fact at the order of $\Lambda_\mathrm{EW} \sim 1\,\mathrm{TeV}$. In the model they propose, Newton's law of gravitation with its large characteristic energy scale $\mathrm{M_{PL}}$ only is a (3+1)-dimensional low energy limit of a fundamental, much stronger higher-dimensional gravity. The additional spatial dimensions are compactified at length scales where Newton's law is experimentally confirmed. As pointed out in the reference, the length scale of this compactification can be large compared to Λ_EW^{-1}, the length scale that is thought to be understood in terms of the 4-dimensional SM. In the following two sections, we introduce this model of Large Extra Dimensions (LED)—the ADD model—more detailed.

2.2.1 Compactified dimensions and the Planck scale

The theory describing space and time on the classical level is Einstein's famous theory of General Relativity, see Ref. [53] for instance. Gravitational effects are connected to the geometry of space through Einstein's equation. Following the sign convention used in Ref. [54], the equation reads in four dimensions

$$R^{(4)}_{\mu\nu} - \tfrac{1}{2} g^{(4)}_{\mu\nu} R^{(4)} = -8\pi G_\mathrm{N} T^{(4)}_{\mu\nu}, \tag{2.17}$$

where $R^{(4)}_{\mu\nu}$, $R^{(4)} = g^{(4)\mu\nu} R^{(4)}_{\mu\nu}$, and $T^{(4)}_{\mu\nu}$ are the 4-dimensional Ricci tensor, Ricci scalar, and energy-momentum tensor, respectively. (We omit the cosmological constant.) The dynamics of gravity are governed by $g_{AB}(x)$, the 4+n dimensional metric tensor, chosen here with the $(+ - \cdots -)$ signature.

Newton's coupling G_N has the units of $(\mathrm{mass})^{-2}$ and defines the Planck scale $\mathrm{M_{PL}} = 1/\sqrt{G_\mathrm{N}}$. Absorbing the factor 8π yields the reduced Planck scale $\overline{\mathrm{M}}_\mathrm{PL} = 1/\sqrt{8\pi G_\mathrm{N}}$. The generalization from four dimensions to a spacetime with additional n spatial dimensions is straight forward through dimensional analysis:

$$R^{(4+n)}_{AB} - \tfrac{1}{2} g^{(4+n)}_{AB} R^{(4+n)} = -\frac{T^{(4+n)}_{AB}}{\overline{\mathrm{M}}_\star^{2+n}}, \tag{2.18}$$

where $\overline{\mathrm{M}}_\star$ is the (4+n)-dimensional reduced Planck mass. Ordinary 4-dimensional Minkowski indices are denoted as μ, ν, etc.; while 4+n-dimensional indices are denoted as A, B, etc.; and the n extra dimensions are labeled with i, j, etc.

Since four-dimensional General Relativity has been verified experimentally on several orders of magnitude, extra dimensions must be hidden from observation at the length scales already tested. Following Ref. [52], the approach chosen here is compactification,

but alternative mechanisms exist [55]. We assume that the extra dimensions are 1) orthogonal to the ordinary 4-dimensional space where the SM is confined to and 2) the product of n 1-dimensional spheres of radius r: $S^1 \times S^1 \times S^1 \times \cdots$ (an n-dimensional torus). Arcs on the spheres serve as coordinates y_i in the extra dimensions. With this choice, any field in the extra dimensions must be $2\pi r$ periodic in y_i. $2\pi r$ is referred to as the size of one extra dimension and $V_n = (2\pi r)^n$ as the volume of the compactified space. Note that an n-torus can have a flat metric (the ordinary Euclidean metric), contrary to an n-sphere.

The effect that n compactified extra dimension have on the fundamental and the effective reduced Planck scales $\overline{\mathrm{M}}_\star$ and $\overline{\mathrm{M}}_{\mathrm{PL}}$, can be examined following the argument of Ref. [56]:

The action corresponding to the homogenous Einstein equation ($T_{AB} = 0$) is the Einstein-Hilbert (EH) action:

$$S_{\mathrm{EH}} = \frac{1}{2}\overline{\mathrm{M}}_\star^{2+n} \int \mathrm{d}x^{4+n} \sqrt{|g^{(4+n)}|} R^{(4+n)}, \tag{2.19}$$

where $g^{(4+n)} = \det g_{AB}^{(4+n)}$. If all matter is confined to the 4-dimensional brane at $y_i = 0$, the Einstein equation (2.18) yields $R = 0$ in the extra dimensions and therefore [56]

$$R^{(4+n)} = R^{(4)}, \qquad |g^{(4+n)}| = |g^{(4)}|. \tag{2.20}$$

Consequently, the integrand in (2.19) does not depend on y_i, and the extra dimensions can be integrated out for a large-enough integration volume (i.e. for a distance scale $\gg r$):

$$S_{\mathrm{EH}} = \frac{1}{2}\overline{\mathrm{M}}_\star^{2+n} (2\pi r)^n \int \mathrm{d}x^4 \sqrt{|g^{(4)}|} R^{(4)}. \tag{2.21}$$

This action exactly is the EH action of traditional 4-dimensional spacetime

$$S_{\mathrm{EH}} = \frac{1}{2}\overline{\mathrm{M}}_{\mathrm{PL}}^2 \int \mathrm{d}x^4 \sqrt{|g^{(4)}|} R^{(4)} \tag{2.22}$$

if the reduced Planck scales are related as

$$\overline{\mathrm{M}}_{\mathrm{PL}} = f \overline{\mathrm{M}}_\star \quad \text{with} \quad f = (2\pi r \overline{\mathrm{M}}_\star)^{n/2}. \tag{2.23}$$

The consequence of this relation is that the true scale of quantum gravity $\sim \overline{\mathrm{M}}_\star$ can be much smaller than the observed large effective 4-dimensional scale $\overline{\mathrm{M}}_{\mathrm{PL}}$ if only f in (2.23) is sufficiently large. For f to be large, the size of the extra dimensions $2\pi r$ must large compared to $1/\overline{\mathrm{M}}_\star$.

In Table 2.2, we list the radii associated with $\overline{\mathrm{M}}_\star = 1\,\mathrm{TeV} \sim \Lambda_{\mathrm{EW}}$. For $n = 1$, the radius of the extra dimension is of the order of an astronomic unit. Since this is the characteristic length scale of one of the most prominent applications of Newton's laws of Gravity with three spatial dimensions—Kepler's laws of planetary motion—this scenario of extra dimensions is clearly ruled out. For $n = 2$, the radius r is at the order of magnitude where current experiments search for deviations from Newton's

n	1	2	3	4	5
r	$2 \times 10^{11}\,\mathrm{m}$	$200\,\mu\mathrm{m}$	$2 \times 10^{-9}\,\mathrm{m}$	$6 \times 10^{-12}\,\mathrm{m}$	$2 \times 10^{-13}\,\mathrm{m}$

Table 2.2: Radius r of n extra dimensions with $\overline{\mathrm{M}}_\star = 1\,\mathrm{TeV}$

law of gravitation ($V_g \sim 1/r$) at small distances. For example, Ref. [57] finds that Newton's law is valid down to $r \approx 50\,\mu\mathrm{m}$, and therefore rules out the model with the parameters in Table 2.2. For a slightly increased $\overline{\mathrm{M}}_\star$, the model is compatible with this limit, though. For $n \geq 3$, the model is far beyond the reach of current small-distance tests. But, as already indicated in Ref. [52], the model is still testable in TeV-scale collider experiments such as the LHC.

Absorbing the factor $(2\pi)^n$ in (2.23), a (4+n)-dimensional Planck mass can be defined as [54]

$$\mathrm{M}_\star = (2\pi)^{n/(n+2)}\overline{\mathrm{M}}_\star. \tag{2.24}$$

Likewise, comparing (2.17) and (2.18), a (4+n)-dimensional version of Newton's coupling can be defined:

$$G_\mathrm{N}^{(4+n)} = \frac{1}{8\pi}\frac{1}{\overline{\mathrm{M}}_\star^{n+2}} = \frac{(2\pi)^n}{8\pi}\frac{1}{\mathrm{M}_\star^{n+2}}. \tag{2.25}$$

Alternative definitions of the coupling and Planck masses frequently are used in the literature, such as in the experimental studies in Ref. [57, 58]. For a review of this notation see Ref. [59].

2.2.2 Gravitons in 4+n dimensions

As a merit of the compactification, gravitational interactions between SM particles may be testable at LHC energies. There is no consents on how a fundamental quantum theory including gravity may look like; prominent candidates are String Theory, Loop Quantum Gravity, or the Asymptotic-Safety Scenario (see Ref. [60] for introductory reviews on the two former theories and Chapter 9 for asymptotic safety). In the low-energy limit, an effective quantum theory basing on the classical gravitational-field formalism can be formulated [61]:

Generally, $g_{AB}(z)$ in (2.18) can be decomposed into a constant background metric η_{AB} and a fluctuation $h_{AB}(z)$:

$$g_{AB}(z) = \eta_{AB} + \frac{2}{\overline{\mathrm{M}}_\star^{(n+2)/2}} h_{AB}(z), \tag{2.26}$$

where we denote the (4+n)-dimensional coordinates as z^A. If h_{AB} can be regarded as a small perturbation from η_{AB} the Einstein equation (2.18) can be linearized in h_{AB}.

As all fields must be $2\pi r$-periodic in the coordinates of the extra dimensions,

$h_{AB}(z^A \equiv (x^\mu, y^i))$ can be written as a Fourier series

$$h_{AB}(x,y) = \sum_{k_1=-\infty}^{\infty} \cdots \sum_{k_n=-\infty}^{\infty} \frac{h_{AB}^{(\boldsymbol{k})}(x)}{\sqrt{V_n}} \exp\left(\mathrm{i}\frac{k^j y_j}{r}\right) \tag{2.27}$$
$$\text{with } \boldsymbol{k} = (k_1, \ldots, k_n),$$

known as a Kaluza-Klein (KK) expansion [62]. We denote the 4-dimensional coordinates on the SM brane as x^μ and the extra-dimensional coordinates as y^i.

The tensor $h_{AB}(z)$, living on the entire (4+n)-dimensional space is therefore equivalent to an infinite tower of KK modes $h_{AB}^{(\boldsymbol{k})}(x)$, depending on the four-dimensional coordinates only. The components of $h_{AB}^{(\boldsymbol{k})}(x)$ transform as tensors, vectors, and scalars in the 4-dimensional subspace. Decomposed in these representations, the linearized Einstein equation yields for $\boldsymbol{k}^2 \neq 0$ [54]

$$(\Box + \boldsymbol{k}^2/r^2)\, G_{\mu\nu}^{(\boldsymbol{k})} = \frac{1}{\overline{\mathrm{M}}_{\mathrm{PL}}} \left[-T_{\mu\nu} + \left(\frac{\partial_\mu \partial_\nu}{\boldsymbol{k}^2/r^2} + \eta_{\mu\nu} \right) \frac{T_\lambda^\lambda}{3} \right] \tag{2.28a}$$

$$(\Box + \boldsymbol{k}^2/r^2)\, V_{\mu i}^{(\boldsymbol{k})} = 0 \tag{2.28b}$$

$$(\Box + \boldsymbol{k}^2/r^2)\, S_{ij}^{(\boldsymbol{k})} = 0 \tag{2.28c}$$

$$(\Box + \boldsymbol{k}^2/r^2) H^{(\boldsymbol{k})} = \frac{1}{\overline{\mathrm{M}}_{\mathrm{PL}}} \sqrt{\frac{n-1}{3(n+2)}} T_\lambda^\lambda. \tag{2.28d}$$

Here the fields are in unitary gauge, all non-physical states are gauged to zero at any spacetime point [54]. The decomposition of $h_{AB}^{(\boldsymbol{k})}$ is enlisted in (A.11) in Appendix A. For massless matter, the trace T_λ^λ is zero. This is a good approximation for most interactions at colliders such as the Drell-Yan process discussed later.

With $T_\lambda^\lambda = 0$, the sole mode in (2.28) coupling to matter is $G_{\mu\nu}^{(\boldsymbol{k})}$. The latter is subject to several constraints[3]; taking these into account, $G_{\mu\nu}^{(\boldsymbol{k})}$ has five degrees of freedom—the appropriate number for a massive spin-2 state. Thus, upon quantization, the fluctuation of the (4+n)-dimensional metric h_{AB} can be associated with an (infinite) KK tower of spin-2 gravitons on the SM brane with masses

$$m_{(\boldsymbol{k})}^2 = \frac{\boldsymbol{k}^2}{r^2}. \tag{2.29}$$

We argued that the size of the extra dimensions must be large compared to the EW scale. This means that the mass gap between neighboring KK states $\sim 1/r$ is small compared to typical $\mathcal{O}$(TeV) collider energies, and that large numbers of KK modes typically contribute in these processes. It is therefore appropriate to replace summations over KK states by integrals over a continuous index k. The number of KK states with $k \leq |\boldsymbol{k}| \leq k + dk$ is [54]

$$dN = S_{n-1} k^{n-1}\, dk, \tag{2.30}$$

[3]Zero trace of $G_{\mu\nu}^{(\boldsymbol{k})}$ and Lorenz conditions for $G_{\mu\nu}^{(\boldsymbol{k})}$.

where

$$S_{n-1} = \frac{2\pi^{n/2}}{\Gamma(n/2)} \tag{2.31}$$

is the (n-1)-dimensional surface of the n-dimensional unity sphere. With $k = mr$ using (2.24) and (2.23), a KK sum can therefore replaced by an integration as per

$$\frac{1}{\overline{\mathrm{M}}_{\mathrm{PL}}^2} \sum_{k_1=-\infty}^{\infty} \cdots \sum_{k_n=-\infty}^{\infty} \quad \to \quad \frac{S_{n-1}}{\mathrm{M}_\star^{n+2}} \int_0^\infty dm\, m^{(n-1)}. \tag{2.32}$$

Although the individual KK gravitons couple to matter with a suppression of $1/\overline{\mathrm{M}}_{\mathrm{PL}}$ just as in the 4-dimensional case, gravitational interactions are enhanced here as the KK towers contribute collectively to typical observables such as the cross sections for real-graviton production or virtual-graviton exchange. Note that the prefactor of the left-over integral in (2.32) is indeed given by the fundamental coupling $G_{\mathrm{N}}^{(4+n)} \propto 1/\mathrm{M}_\star^{n+2}$. In fact, virtual-graviton amplitudes are not only enhanced by the sum over the KK states, they typically diverge for $n \geq 2$ unless the high-mass modes are cutoff or dampened. This divergence is a manifestation of the problematic high-energy behavior of Einstein Gravity. Since m corresponds to the (4+n)-dimensional graviton's momentum perpendicular to the SM brane [cf. (2.27)], a high m implies a high momentum of the associated (4+n)-dimensional graviton. A frequently employed way to calculate finite amplitudes is to assume that the KK sums are rendered finite by a higher-scale mechanism (String Theory, e.g.) and to parametrize the dimensionful sum by an effective scale Λ_{eff}. In Part III, we will employ such a high-scale mechanism, Asymptotic Safety, to calculate finite virtual-graviton amplitudes.

Part II

Stops and flavor at the LHC

3 Introduction: Sparticles as probes for flavor dynamics

In the second part of this thesis, we discuss a specific phenomenological topic in the MSSM. The reasoning and structure is outlined in the following.

The R-parity-conserving MSSM introduced in Chapter 2 can resolve the SM's hierarchy problem, provides cold or warm dark-matter candidates, and exhibits an incidental unification of the gauge couplings [63]. With these features it is one of the key candidates of BSM physics searched for at the LHC [64, 65]. Owing to its soft SUSY-breaking, the MSSM has a significantly increased number of flavor-violating couplings compared to the SM. These couplings render the MSSM highly discriminative with respect to theories of flavor-breaking; predictions in agreement with the SM Yukawa structure can be challenged experimentally in the MSSM.

In Chapter 4 we demonstrate how the prediction for the squark mass matrices vary exemplarily for a popular mechanism of flavor-breaking (horizontal symmetries). In the same chapter we also briefly review experimental bounds on the flavor structure of the squark masses, and find that parts of the up-type squark mass matrix $\mathcal{M}_U^2$ involving top-flavor essentially are unbounded. Since the predictions for these terms vary distinctly, their measurement would hint at the source of flavor violation.

The LHC potentially produces on-shell sparticles; hence, one can also strive to investigate the mixing structure of the squark mass matrices by measuring (tree-level) flavor-changing neutral currents (FCNCs) in sparticle decays. With R-parity conservation, sparticles have to be produced in even numbers and decay in cascades to typically high-energetic SM particles and LSPs. The LSP usually is neutral (a neutralino $\tilde{\chi}_1^0$, gravitino $\tilde{G}$, or sneutrino $\tilde{\nu}_1$) and leaves the detector without being detected. In such a setting, a measurement of FCNC branching ratios is severely aggravated:

- The LSPs cannot be detected and generate characteristic large missing transverse energy ($\not{E}_T$). In consequence, the kinematics of the interacting sparticles cannot be fully reconstructed. (See Appendix A for definitions of frequently-used collider variables such as $\not{E}_T$.)

- The agreement of the 7-TeV and 8-TeV LHC findings with the SM predictions implies that the typical mass scale of non-split SUSY cannot be lower than the TeV scale [66]. This high mass scale limits the total number of sparticle produced in the LHC program. (Stops still can be relatively light and thus allow for sizable event numbers.)

- The generally high-energetic gluons and quarks, produced at the end of a squark cascade, generate large hadron showers that are registered as collimated high-p_T jets in the detectors.

The capabilities of identifying the flavor of a jet's initial quark (flavor-tagging) is limited in the dense environment of a high-luminosity hadron collider. Only b-jets and c-jets (τ-jets) can be tagged with noticeable efficiencies. b-jets can be tagged with efficiencies of up to 80% [67], dependent on the accepted miss-tagging rate. For charm-jets, the tagging performance is worse. ATLAS expects the c-tagging efficiency to reach up to 40% in the low-luminosity 7-TeV data [68]. Due to the increased particle densities, the tagging performances drop with increasing jet p_T [64].

In Chapter 5, we introduce a specific scenario, where the partly unconstrained top-flavor–mixing entries of $\mathcal{M}_U^2$ can be bounded with directly produced sparticles despite these limitations: The lighter top squark (stop) $\tilde{t}_1$ can be such light that its decay to other third-generation quarks or squarks can be forbidden kinematically. In this case, the light stop's decay rate would be controlled by its dominant FCNC decay mode. Hence, the associated lifetime is sensitive to the stop's off-diagonal flavor structure. While a measurement of a subleading branching fraction becomes more involved the smaller the flavor-mixing coupling is, a lifetime would be more accessible for extraordinarily small flavor-mixing couplings. Minimal Flavor Violation, discussed in Chapter 4, exhibits a characteristic decoupling of the third generation from the first two generations of squarks. With this flavor pattern, the lifetime of $\tilde{t}_1$ can be such small that $\tilde{t}_1$ can even decay significantly displaced from its production vertex [69]. We discuss the LHC phenomenology of the decay $\tilde{t}_1 \to \tilde{\chi}_1^0 c$ for stop pairs, produced in association with top pairs, assuming that $\tilde{\chi}_1^0$ is the LSP.

In Chapter 6, we extend the discussion to a scenario where the LSP is a gravitino. The parameter space in this case is highly constrained by early 7-TeV LHC data.

4 Flavor in the MSSM

In the following, we briefly review the bounds on the MSSM's flavor structure, available at the time of writing. We further demonstrate how the prediction of unconstrained parts of the squark mass matrices can differ among different predictions of the flavor structure, and introduce the concept of Minimal Flavor Violation.

4.1 Constraints on the squark mass matrices

Sparticles can contribute at the loop order to SM amplitudes. The SM predictions for FCNC phenomena such as neutral-meson oscillations and rare decays are at the loop level too, they are further only are EW processes and CKM suppressed. In consequence, FCNC data impose severe constraints on the flavor structure of the TeV-scale MSSM. For illustration, Figure 4.1 shows typical box graphs for the EW SM amplitude for B_d-$\bar{B}_d$ oscillation as well as MSSM contributions. As apparent in the mass-insertion approximation [70], amplitudes with external quarks q_I, and q_J constrain the IJ-entries of the RR, RR, and LR sub-blocks of squark mass matrices $\mathcal{M}_d^2$ and $\mathcal{M}_u^2$.

Commonly, bounds on the off–flavor-diagonal entries of $\mathcal{M}_q^2$ ($q = u$, d) are stated in terms of dimensionless $(\delta^q_{\rm AB})_{IJ}$, defined as

$$(\delta^q_{\rm AB})_{IJ} = \frac{(\mathcal{M}^2_{q,\rm AB})_{IJ}}{\tilde{M}^2} \tag{4.1}$$

in the super-CKM basis, for A, B = L, R and I, J = 1–3. $\tilde{M}$ is the characteristic energy scale for the squark mass matrix entry $(\mathcal{M}^2_{q,\rm AB})_{IJ}$. Frequent choices for this scale are the arithmetic mean $\tilde{M}_a^2 = \frac{1}{6}\mathrm{Tr}\left(\mathcal{M}_q^2\right)$ and the geometric mean $\tilde{M}_g^2 = \sqrt{(\mathcal{M}^2_{q,\rm AA})_{II}(\mathcal{M}^2_{q,\rm BB})_{JJ}}$.

In Table 4.1 we list experimental constraints on the individual flavor-mixing $(\delta^q_{\rm AB})_{IJ}$ ($I \neq J$), each obtained assuming that all other $(\delta^q_{\rm AB})_{IJ}$ are zero. The bounds on the down-type squark sector generally are tighter than those on the up-type squark sector.

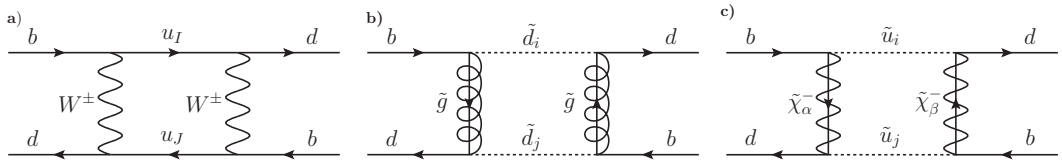

Figure 4.1: Typical box graphs generating B_d-$\bar{B}_d$ mixing. (a) EW SM graph. (b) QCD MSSM graph . (c) MSSM chargino graph. With I, J = 1–3; i, j = 1–6; α, β = 1, 2.

Down-squark sector					
Process	Ref.	Mixing param.	Bound	Mixing param.	Bound
K-$\bar{K}$ mixing	[70, 71]	$\sqrt{\lvert\mathrm{Re}\left(\delta^d_{\mathrm{LL}}\right)^2_{12}\rvert}$	4.0×10^{-2}	$\sqrt{\lvert\mathrm{Re}\left(\delta^d_{\mathrm{LL}}\right)_{12}\left(\delta^d_{\mathrm{RR}}\right)_{12}\rvert}$	2.8×10^{-3}
		$\sqrt{\lvert\mathrm{Re}\left(\delta^d_{\mathrm{LR}}\right)^2_{12}\rvert}$	4.4×10^{-3}		
		$\sqrt{\lvert\mathrm{Im}\left(\delta^d_{\mathrm{LL}}\right)^2_{12}\rvert}$	3.2×10^{-3}	$\sqrt{\lvert\mathrm{Im}\left(\delta^d_{\mathrm{LL}}\right)_{12}\left(\delta^d_{\mathrm{RR}}\right)_{12}\rvert}$	2.2×10^{-4}
		$\sqrt{\lvert\mathrm{Im}\left(\delta^d_{\mathrm{LR}}\right)^2_{12}\rvert}$	3.5×10^{-4}		
B_d-$\bar{B}_d$ mixing	[71]	$\sqrt{\lvert\mathrm{Re}\left(\delta^d_{\mathrm{LL}}\right)^2_{13}\rvert}$	9.8×10^{-2}	$\sqrt{\lvert\mathrm{Re}\left(\delta^d_{\mathrm{LL}}\right)_{13}\left(\delta^d_{\mathrm{RR}}\right)_{13}\rvert}$	1.8×10^{-2}
		$\sqrt{\lvert\mathrm{Re}\left(\delta^d_{\mathrm{LR}}\right)^2_{13}\rvert}$	3.3×10^{-2}		
	[72]	$\sqrt{\lvert\mathrm{Im}\left(\delta^d_{\mathrm{LL}}\right)^2_{13}\rvert}$	0.2	$\sqrt{\lvert\mathrm{Im}\left(\delta^d_{\mathrm{LR}}\right)^2_{13}\rvert}$	5×10^{-2}
$b\to s\gamma$	[73]	$\lvert\left(\delta^d_{\mathrm{LR}}\right)_{23}\rvert$	8.3×10^{-3}	$\lvert\left(\delta^d_{\mathrm{RL}}\right)_{23}\rvert$	1.1×10^{-2}
B_s-$\bar{B}_s$ mixing, $b\to s\gamma$	[74]	$\lvert\left(\delta^d_{\mathrm{LL}}\right)_{23}\rvert$	0.6^a	$\lvert\left(\delta^d_{\mathrm{RR}}\right)_{23}\rvert$	0.8^a

(a: with only one δ contributing; much tighter bounds with correlations. $\tan\beta = 3$.)

Up-squark sector					
Process	Ref.	Mixing param.	Bound	Mixing param.	Bound
D-$\bar{D}$ mixing	[75]	$\lvert(\delta^u_{\mathrm{LL}})_{12}\rvert$	4.9×10^{-2}	$\lvert(\delta^u_{\mathrm{RR}})_{12}\rvert$	4.9×10^{-2}
		$\lvert(\delta^u_{\mathrm{LR}})_{12}\rvert$	8.0×10^{-2}	$\lvert(\delta^u_{\mathrm{RL}})_{12}\rvert$	8.0×10^{-2}
K-$\bar{K}$ mixing	[76]	$\sqrt{\lvert\mathrm{Re}\,(\delta^u_{\mathrm{LL}})^2_{12}\rvert}$	0.1	$\sqrt{\lvert\mathrm{Im}\,(\delta^u_{\mathrm{LL}})^2_{12}\rvert}$	1.5×10^{-2}
		$\lvert\mathrm{Im}\,(\delta^u_{\mathrm{LL}})_{12}\rvert$	0.2		
B_d-$\bar{B}_d$ mixing	[77]	$\sqrt{\lvert\mathrm{Re}\,(\delta^u_{\mathrm{LL}})^2_{13}\rvert}$	0.3	$\sqrt{\lvert\mathrm{Re}\,(\delta^u_{\mathrm{LL}})_{13}\,(\delta^u_{\mathrm{LL}})_{23}\rvert}$	0.3
		$\sqrt{\lvert\mathrm{Im}\,(\delta^u_{\mathrm{LL}})^2_{13}\rvert}$	0.4	$\sqrt{\lvert\mathrm{Re}\,(\delta^u_{\mathrm{LL}})_{13}\,(\delta^u_{\mathrm{RL}})_{31}\rvert}$	0.4
No CCB	[78]	$\lvert(\delta^u_{\mathrm{LR}})_{13}\rvert$	0.6	$\lvert(\delta^u_{\mathrm{RL}})_{13}\rvert$	0.6
$b\to s\ell^+\ell^-$	[79]	$\lvert(\delta^u_{\mathrm{LR}})_{23}\rvert$	0.2		
No CCB	[78]	$\lvert(\delta^u_{\mathrm{LR}})_{23}\rvert$	0.6	$\lvert(\delta^u_{\mathrm{RL}})_{23}\rvert$	0.6

Table 4.1: Constraints on flavor mixing in the squark masses. For $\tilde{M} = m_{\tilde{g}} = m_{h_u} = 500\,\mathrm{GeV}$. The chargino-induced bounds for the $(\delta^u_{\mathrm{AB}})_{I3}$ ($I = 1, 2$) further depend on the chargino mass structure; refer to the original publications for details. CCB bound as in (4.2).

The apparent reason for this is that most observed flavor-mixing phenomena are in the down-quark sector, with the exception of charm FCNCs. (SUSY-)QCD graphs involving gluinos and squarks are α_s enhanced, and therefore usually give more severe bounds compared to chargino graphs. In consequence, the QCD-induced bounds on δ_d are generically stronger than chargino-induced bounds on δ_u, especially if the relevant sparticle masses are comparable.

Note that flavor mixing in $\mathcal{M}^2_{u,\mathrm{LL}}$ and $\mathcal{M}^2_{d,\mathrm{LL}}$ is governed by the same soft SUSY-breaking term, m^2_Q. Therefore, the small flavor-mixing in $\mathcal{M}^2_{d,\mathrm{LL}}$ implies that the mixing in $\mathcal{M}^2_{u,\mathrm{LL}}$ is suppressed as well. Care must be taken in the explicit conversion of individual bounds, since in the super-CKM basis, m^2_Q contributes as m^2_Q and $\mathsf{V}^\dagger_{\mathrm{CKM}}\mathsf{m}^2_Q\mathsf{V}_{\mathrm{CKM}}$ to $\mathcal{M}^2_{u,\mathrm{LL}}$ and $\mathcal{M}^2_{d,\mathrm{LL}}$ respectively.

Requiring a well-behaved scalar potential yields theoretical bounds on the LR-mixing off-diagonal squark mass entries: For the vacuum neither to be color or charge breaking (CCB) nor unbounded from below (UFB), the LR-mixing insertions have to fulfill [78]

$$|(\delta^u_{\mathrm{LR}})_{IJ}| \overset{\mathrm{CCB}}{\leq} m_K \frac{\left[2\tilde{M}^2_{(u)} + m^2_{h_u}\right]^{1/2}}{\tilde{M}^2_{(u)}}, \quad |(\delta^u_{\mathrm{LR}})_{IJ}| \overset{\mathrm{UFB}}{\leq} m_K \frac{\left[2\tilde{M}^2_{(u)} + 2\tilde{M}^2_{(\ell)}\right]^{1/2}}{\tilde{M}^2_{(u)}}, \quad (4.2)$$

exemplarily in the up-type sector. Here, $\tilde{M}^2_{(f)}$ is the average of the squared soft $\tilde{f}$ masses, $K = \max(I, J)$, and m_K is the mass up-type quark K.

Stop sector

In the following, we focus on the stop part of $\mathcal{M}^2_u$. Remarkably, there is no direct experimental constraint on $(\delta^u_{\mathrm{LL}})_{23}$, $(\delta^u_{\mathrm{RR}})_{I3}$, or $(\delta^u_{\mathrm{RL}})_{I3}$ $(I = 1, 2)$, see Table 4.1. $(\delta^u_{\mathrm{LL}})_{23}$ would be constrained through chargino corrections to B_s-$\bar{B}_s$ mixing. Yet, the contribution to the observables ΔM_s and $\sin 2\beta_s$ is found to be negligible numerically [80]. [$(\delta^u_{\mathrm{LL}})_{23}$ is indirectly constrained through the $\left(\delta^d_{\mathrm{LL}}\right)_{IJ}$, nevertheless.] For the other insertions, an experimental constraint would involve a chargino coupling through its higgsino component to a right-handed light quark (s or d). These couplings are suppressed by small $\mathsf{V}_{\mathrm{CKM}}$ entries or Yukawa couplings; in consequence, they yield no relevant contributions to observables in the B systems [77]. Because of the largeness of m_t, CCB and UFB bounds on $(\delta^u_{\mathrm{RL}})_{I3}$ are weak (≈ 0.6).

Supplementary to FCNCs in the B sector, prompt rare top decays $t \to (\gamma/Z/g)q$ with $q = u$, c would constrain the flavor-mixing $(\delta^u_{\mathrm{AB}})_{I3}$ experimentally, if they were measured. In the SM, the individual branching fractions of these decays are severely suppressed to $\mathcal{O}(10^{-14})$ and $\mathcal{O}(10^{-12})$ for EW bosons and gluons, respectively [81]. In the MSSM, the amplitudes can be significantly enhanced through gluino penguin graphs. In a parameter-space scan [79], branching ratios of up to 7×10^{-8}, 1×10^{-7}, and 7×10^{-7} for the decays to γc, Zc, and gc are found to be in agreement with the bounds in Table 4.1. The largest values stem from the largest allowed $(\delta^u_{\mathrm{RL}})_{23}$.

Although the branching fractions thus are very sensitive to the stop flavor structure, the experimental bounds are far above the expected values at the time of writing.

Most severe is the bound on the branching fraction $\mathcal{B}(t \to Zq)$, which the CMS collaboration finds to be below 2×10^{-3} [82]. The LHC is expected to be sensitive down to $\mathcal{B}(t \to \gamma q) \approx 5 \times 10^{-6}$ and $\mathcal{B}(t \to gq) \approx 2 \times 10^{-5}$, with a center-of-mass energy $\sqrt{s} = 14\,\text{TeV}$ and an integrated luminosity ($\mathcal{L}_{\text{int}}$) of $100\,\text{fb}^{-1}$ [83]. Consequently, the rare–top-decay rate to charms presumably is not accessible experimentally in the SM or MSSM at the LHC. (An analogous argument holds for decays to up quarks.)

4.2 The origin of flavor violation

A realistic mechanism to explain flavor violation in the squark and quark sectors must 1) explain the symmetry breaking itself, 2) why there are such small hierarchical numbers involved—CKM-matrix entries, small Yukawa couplings, and in case of SUSY small flavor–off-diagonal $(\delta^q_{\text{AB}})_{IJ}$'s. 3) Finally it also has to produce masses plus CKM angles and phases compatible with the experimental findings at the EW scale.

A highly regarded hypothesis is the existence of a high-scale horizontal flavor symmetry group. We first introduce the formalism focusing on the SM sector and extend the discussion to the MSSM afterwards. The horizontal group $\mathcal{H}$ differentiates between the three generations, i.e. the generations transform according to different representations of $\mathcal{H}$ or have different charges [14]. With additional scalar fields transforming non-trivially under $\mathcal{H}$, the SM fields form $\mathcal{H}$-invariant higher-dimensional operators. The order at which a particular operator appears depends on the representations the participating fields are assigned to. In the simplest case, $\mathcal{H}$ is a U(1) and there is one scalar ϕ of (negative) horizontal unit-charge ($Q_H(\phi) = -1$). Exemplarily, if the SM's third-generational gauge eigenstates (cf. Table 1.1) and the SM Higgs doublet H are charged as $Q_H(q^3_{\text{L}}) = 0$, $Q_H(\bar{u}^3_{\text{R}} = \bar{t}_{\text{R}}) = 0$, $Q_H(\bar{d}^3_{\text{R}} = \bar{b}_{\text{R}}) = 2$, and $Q_H(H) = 0$, the leading $\mathcal{H}$-invariant Yukawa-like interaction terms would be a dimension-6 down-type and a dimension-4 up-type term:

$$\mathcal{L}_{\mathcal{H}\text{Y}} = -C_{d,33} \left(\frac{\phi}{M}\right)^2 H^* q^3_{\text{L}} \bar{b}_{\text{R}} - C_{u,33} \left(\frac{\phi}{M}\right)^0 H \circ q^3_{\text{L}} \bar{t}_{\text{R}}. \tag{4.3}$$

Here M is a characteristic large scale, for which the effective-theory description is meaningful, and the $C_{q,ij}$ are equal-order effective couplings. As before, $A \circ B$ denotes the antisymmetric product $A_\alpha \epsilon_{\alpha\beta} B_\beta$ (α, $\beta = 1$, 2). If ϕ acquires a VEV or background value $\langle\phi\rangle$, the horizontal symmetry is broken. Powers of the small ratio $\epsilon = \langle\phi\rangle/M$ appearing in the newly formed dimension-4 term generate a hierarchical Yukawa coupling, based on the Q_H assignments of the fields involved.

In such a construction, the benefits of having more flavor-violating couplings in the MSSM compared to the SM are apparent: A measure for the predictivity of a model is the number of parameter choices (charges) in relation to the number of quantities it predicts. If $\mathcal{H}$ is a inner symmetry of the theory, commuting with supersymmetry transformations, the superpartners transform uniformly under $\mathcal{H}$ transformations (have equal Q_H charges). The charge and representation choices are significantly constrained by requiring a correct V_{CKM} and SM-fermion mass hierarchy. Yet, the predictions for the squark mass structure significantly vary with $\mathcal{H}$ and representation assignments in

combination with SUSY-breaking mechanisms, and thus allow to test different flavor hypothesises.

Considerable effort has been devoted to the analysis of minimal horizontal-symmetry groups that increases the predictivity by requiring fewer ad-hoc charge or representation choices, see Ref. [84] e.g. As an example of the soft terms' sensitivity to $\mathcal{H}$, the entries of the weakly-constrained soft term m_U^2 can be of the order of [85]

$$\mathsf{m}_U^2 \propto \begin{pmatrix} 1 & \lambda^2 & \lambda^3 \\ \lambda^2 & 1 & \lambda \\ \lambda^3 & \lambda & 1 \end{pmatrix} \qquad \text{or} \qquad \mathsf{m}_U^2 \propto \begin{pmatrix} 1 & \lambda^2 & \lambda^3 \\ \lambda^2 & 1 & \lambda^5 \\ \lambda^3 & \lambda^5 & 1 \end{pmatrix}, \tag{4.4}$$

for $\mathcal{H} = \mathrm{U}(1)$ or $\mathcal{H} = \mathrm{U}(1) \times \mathrm{U}(1)$, respectively—given that they can be written as $\mathcal{H}$-invariant higher-dimensional operators as in (4.3). The small parameter λ is the small Cabibbo angle controlling the hierarchy of $\mathsf{V}_{\mathrm{CKM}}$, cf. (1.8). Note how the 2-3 entries differ distinctly while reproducing quark masses and mixing.

The effect a horizontal symmetry has on the soft SUSY-breaking terms crucially depends on the SUSY-breaking mechanism. (See Ref. [16, 40] for introductions to different mechanisms.) In the example yielding (4.4), we assume that the soft SUSY-breaking terms can be written as $\mathcal{H}$-invariant higher-dimensional operators along the lines of (4.3), i.e. that SUSY is broken before $\mathcal{H}$-breaking takes place. Most certainly, SUSY-breaking is mediated to the visible sector at a scale $\Lambda_s > M$ in gravity-mediated SUSY breaking with $\Lambda_s \sim \mathrm{M}_{\mathrm{PL}}$. Yet, with GMSB, exemplarily, the scale of SUSY-breaking mediation can be quite low: $\Lambda_s \sim M_m \sim \mathcal{O}(50\,\mathrm{TeV})$ [16], with the messenger mass scale M_m. In this case $\langle\phi\rangle > M_m$ is feasible, i.e. flavor breaking can take place before SUSY breaking. Effective operators such as in (4.3) then can only be constructed for the supersymmetric superpotential $\mathcal{W}$ with an appropriate left-chiral superfield $\Phi \subset \phi$, where $\langle\phi\rangle$ leaves the supersymmetry intact. In such a case, the horizontal symmetry only generates the Yukawa structure, but has no influence on the terms in $\mathcal{L}_{\mathrm{soft}}$ at the messenger scale. In GMSB models, the soft terms are generated through gauge interactions and are flavor blind in the basic models therefore:

$$\mathsf{m}_U^2 \propto \mathbb{1}_3. \tag{4.5}$$

Note that these soft terms yield a non-diagonal flavor structure through Yukawa contributions in RG running from M_m down to Λ_{EW}, nevertheless.

The flavor structures of hybrids SUSY-breaking mechanisms are also discussed in the literature [86]. As an alternative to horizontal symmetries, flavor can also be broken radiatively, cf. Ref. [87] for a realistic model.

4.3 Minimal Flavor Violation

In low-scale phenomenology, a modest question is if the SM flavor structure, i.e. its Yukawa couplings, is the only source of flavor violation in a particular BSM model. Such a model is said to exhibit Minimal Flavor Violation (MFV) [88]. In a

minimally flavor violating model, FCNC observables would generically be protected from BSM contributions through the hierarchy of the SM Yukawas. (MFV nevertheless is challenged by precision measurements in the B_s sector, cf. Ref. [89], e.g.) Note that most benchmark models extensively used in collider studies exhibit MFV: mSUGRA [90], mGMSB [46], AMSB [91].

MFV can be regarded as an extreme case of the horizontal-symmetry pattern discussed in the previous section: If $\mathcal{H} = \mathcal{G}_{\text{flav}} = \text{SU}(3)^5$, with $\mathcal{G}_{\text{flav}}$ as discussed in Section 1.2, all three generations of the MSSM super fields Q, U, and D would belong to the same representations of $\mathcal{H}$, consistent with the assignments in (1.5). The SM Yukawa couplings can be identified with dimensionless background values of the additional non-trivially transforming fields, equivalent to $\langle\phi\rangle/M$. With these assignments, the symmetry of the Yukawa mass terms would be restored if the Yukawa couplings were transforming as

$$\mathsf{Y}_u \sim (\mathbf{3}, \bar{\mathbf{3}}, \mathbf{1})_q, \qquad \mathsf{Y}_d \sim (\mathbf{3}, \mathbf{1}, \bar{\mathbf{3}})_q, \qquad \mathsf{Y}_e \sim (\mathbf{3}, \bar{\mathbf{3}})_\ell. \tag{4.6}$$

Consequently, if the MSSM exhibits MFV, any of the soft SUSY-breaking sfermion terms in (2.4) is a $\mathcal{G}_{\text{flav}}$-symmetric contraction of Yukawa matrices and sfermion fields. Specifically, the soft couplings contributing to the up-type squark mass matrix in (2.12) are writable as an expansion in Y_u and Y_d:

$$\mathsf{m}_Q^2 = \tilde{m}^2 \left(a_1 \mathbb{1}_3 + b_1 \mathsf{Y}_u \mathsf{Y}_u^\dagger + b_2 \mathsf{Y}_d \mathsf{Y}_d^\dagger + b_3 \mathsf{Y}_d \mathsf{Y}_d^\dagger \mathsf{Y}_u \mathsf{Y}_u^\dagger + b_4 \mathsf{Y}_u \mathsf{Y}_u^\dagger \mathsf{Y}_d \mathsf{Y}_d^\dagger + \dots \right) \tag{4.7a}$$

$$\mathsf{m}_U^2 = \tilde{m}^2 \left(a_2 \mathbb{1}_3 + b_5 \mathsf{Y}_u^\dagger \mathsf{Y}_u + \dots \right) \tag{4.7b}$$

$$\mathsf{A}_u = A \left(c_1 \mathbb{1}_3 + d_1 \mathsf{Y}_d \mathsf{Y}_d^\dagger + \dots \right) \mathsf{Y}_u. \tag{4.7c}$$

Here the a_i, b_i are real and the c_i, d_i are real if CP violation exclusively stems from the CKM phases. The a_i and c_i are the expansion coefficients of the lowest-dimensional $\mathcal{G}_{\text{flav}}$-invariant operator, the b_i and d_i those of the higher-dimensional ones. $\tilde{m}$ and A are typical mass scales.

The bilinear soft couplings m_Q^2 and m_U^2 are Hermitean matrices. Technically, the MFV hypothesis does not constrain these terms' flavor structure at all: There exists a finite expansion to the second power in $\mathsf{X}_u = \mathsf{Y}_u^\dagger \mathsf{Y}_u$ and $\mathsf{X}_d = \mathsf{Y}_d^\dagger \mathsf{Y}_d$ for any Hermitean 3×3 matrix by the virtue of the Cayley-Hamilton identities [92]. Yet, because of the strong hierarchy of Y_u and Y_d [cf. (1.7)], the expansion of an arbitrarily textured Hermitean matrix would require large a_i and b_i with large cancellations among the terms. Following Ref. [92], the MFV categorization therefore can be retained by requiring that for a minimally flavor violating theory, the coefficients a_i and b_i become smaller with increasing dimension of the mass term.

A crucial observation for this thesis is that—in diagonal-Y_u basis—all leading entries in (4.7) mixing the third with the first two generation are severely CKM and Yukawa suppressed [69]. As discussed in the next chapter, this suppression potentially can make these entries experimentally accessible.

5 Probing flavor with long-lived light stops

We established in the last chapter that the flavor structure of the top's superpartners, the stops $\tilde{t}_1$ and $\tilde{t}_2$, is remarkably weakly bounded. Very generally, this can be traced to the extraordinary large top mass, preventing the formation of top-flavored hadrons and suppressing top-production cross sections.

In the following (Section 5.1), we discuss that the largeness of the top mass on the other side implies that the light stop generally is one of the lightest sparticles. We establish that this lightness can imply that flavor-diagonal $\tilde{t}_1$-decays could be kinematically closed. In Section 5.2 we discuss that in this case the lifetime of $\tilde{t}_1$ is sensitive to the stop's flavor-mixing structure. In MFV, $\tilde{t}_1$ can have such a long life that its decay may take place significantly displaced from its production vertex. We discuss this displaced decay for stop pairs produced in association with top pairs at the LHC in Section 5.3.

5.1 Stop masses

While the third generation of quarks is the heaviest one, the opposite is generally assumed for the third generation of squarks. We discuss two theoretical and two phenomenological reasons now.

5.1.1 Renormalization-group running

The large third generation's Yukawa couplings λ_t and λ_b have a significant influence on the RG evolution of the soft couplings A_u, m_Q^2, and m_U^2—refer to Appendix A for one-loop β-functions. The large third-generational Yukawa couplings favor a light stop sector in GUT-like scenarios:

Neglecting flavor–off-diagonal entries, the β-functions for the above-mentioned soft terms receive negative contributions from gauginos, most notably from gluinos. For $(\mathsf{m}_Q^2)_{II}$ and $(\mathsf{m}_U^2)_{II}$ ($I = 1$–3), a positive term $\propto \lambda_{u_I}^2$ competes with the negative gaugino terms [16]:

$$\beta\Big((\mathsf{m}_U^2)_{II}\Big) = \frac{d}{dt}(\mathsf{m}_U^2)_{II} \subset \frac{1}{8\pi^2}\left(2\lambda_{u_I}^2 S_i - \frac{16}{3} g_s^2 |M_3|^2\right), \tag{5.1}$$

exemplarily, with S_i being a sum of squared soft masses and the RG time $t = \ln(\mu/\mu_0)$. With negligible first-generation Yukawa couplings, the β functions for $(\mathsf{m}_U^2)_{II}$ and $(\mathsf{m}_Q^2)_{JJ}$ ($J = 1$–2), evaluated at a random scale, therefore are smaller than those of the third generation. If the soft terms are unified at a certain high scale, $(\mathsf{m}_Q^2)_{33}$ and $(\mathsf{m}_U^2)_{33}$ are smaller than $(\mathsf{m}_Q^2)_{II}$ and $(\mathsf{m}_U^2)_{JJ}$, ($J = 1, 2$) at the TeV scale. In the β-functions for the A_u-terms, contributions proportional to Yukawa couplings compete or enhance the gaugino contributions, dependent on $\mathrm{sign}(\mathsf{A}_u^{II})$.

The situation in the down-sector is similar; since $\lambda_b \ll \lambda_t$ for most values of $\tan\beta$, the effect usually is larger in the up-type sector. The RG effects are larger the further away the unification scale is from the EW scale. Hence they generally are more pronounced in gravity-mediation models than in GMSB models.

5.1.2 LR mixing

While the general mass scale of the stop sector may be lower than that of first two generation of squarks, the stop sector also exhibits a generically enhanced LR-mixing, see $\mathcal{M}^2_{U,\mathrm{LR}}$ in (2.13c). This enhancement occurs if the A_u-term is smaller than or exhibits a structure similar to Y_u, such as in MFV, baring cancellations between the A_u and Y_u terms in $\mathcal{M}^2_{U,\mathrm{LR}}$. Note that A_u^{IJ} ($I,\, J = 1,\, 2$) is significantly constrained through the requirement of a well-behaved vacuum along the lines of (4.2). We consider the third generation to be the sole generation with significant LR-mixing. The implied mass splitting between $\tilde{t}_1$ and $\tilde{t}_2$ lowers the mass of $\tilde{t}_1$, as readily can be seen by equating the Eigenvalues of the stop mass matrix, constrained to the flavor-diagonal contributions and with $m^2_{\tilde{t}} \approx (\mathcal{M}^2_{U,\mathrm{LL}})_{33} \approx (\mathcal{M}^2_{U,\mathrm{RR}})_{33}$, $m^2_{\mathrm{LR}} = (\mathcal{M}^2_{U,\mathrm{LR}})_{33}$ for simplicity:

$$\mathcal{M}^2_{\mathrm{stop}} = \begin{pmatrix} m^2_{\tilde{t}} & m^2_{\mathrm{LR}} \\ (m^2_{\mathrm{LR}})^* & m^2_{\tilde{t}} \end{pmatrix} \tag{5.2}$$

$$\Rightarrow \qquad m^2_{\tilde{t}_{1,2}} = m^2_{\tilde{t}} \pm \Delta m^2_{\tilde{t}} \qquad \text{with} \qquad \Delta m^2_{\tilde{t}} = |m^2_{\mathrm{LR}}|. \tag{5.3}$$

5.1.3 Higgs-mass corrections

The Higgs masses are subject to significant radiative corrections from Yukawa-induced fermion-sfermion loops, Higgs-higgsino loops, and gauge-boson–gaugino loops. We consider them in the phenomenologically preferred decoupling limit, see (2.8).

The largest contribution stems from the stop-top sector. At one loop it is [93, 94]

$$\delta m^2_h \approx \frac{3 G_F m_t^4}{\sqrt{2}\pi^2} \left[\ln\left(\frac{m^2_{\tilde{t}}}{m^2_t}\right) + \frac{X_t^2}{m^2_{\tilde{t}}} \left(1 - \frac{X_t^2}{12 m^2_{\tilde{t}}}\right)\right], \tag{5.4}$$

where $m^2_{\tilde{t}} = (\mathsf{m}^2_Q)_{33} = (\mathsf{m}^2_U)_{33}$ and $X_t = (\mathcal{M}^2_{U,\mathrm{LR}})_{33}/m_t$. The dominance of this term stems from the overall factor $m_t^4 \gg m_Z^4,\, m_b^4$.

The tree-level mass of the light Higgs can be approximated by its maximum value m_Z, unless $\tan\beta$ is close to one. Significant radiative corrections thus are required to lift the mass from $\mathcal{O}(m_Z)$ to the experimentally preferred value of $m_h = (125.9 \pm 0.4)\,\mathrm{GeV}$ [7]. Approximating the radiative corrections by the one-loop contribution (5.4), bounds on the stop mass scale can be derived. Without any LR-mixing, a high stop mass scale of $\mathcal{O}(1.2\,\mathrm{TeV})$ is necessary to lift m_h to 125 GeV. Yet, if the second term in (5.4) incorporating LR-mixing is close to its maximum at $X_t = \sqrt{6} m_{\tilde{t}}$, the requirement $m_z^2 + \delta m_h^2 \approx (125\,\mathrm{GeV})^2$ does not constrain $m_{\tilde{t}_1}$ from below at all, cf. Ref. [94].

A very light $\tilde{t}_1$ is compatible with the experimentally favored Higgs mass as long as $\tan\beta \neq 1$ and as long as there is a large LR-mixing, implying a large mass splitting between $\tilde{t}_1$ and $\tilde{t}_2$.

Note that the stop sector cannot be arbitrarily heavy, because it would generate a new, "little" hierarchy problem [95]: Neglecting stop-LR mixing for simplicity, the soft Higgs mass parameter $m^2_{h_u}$ receives radiative corrections $\propto (m^2_{\tilde{t}} - m^2_t)$. However this soft mass parameter has to adds up with $m^2_{h_d}$ and the superpotential parameter μ^2 to give a quantity of $\mathcal{O}(m^2_Z)$ to guarantee EW symmetry breaking:

$$m^2_{h_u} \sin^2\beta - m^2_{h_d} \cos^2\beta - |\mu|^2 \cos 2\beta = \frac{1}{2} M^2_Z \cos 2\beta. \tag{5.5}$$

For a large stop mass sector the required cancellations are unnatural.

5.1.4 Direct-search limits

The lighter stop's mass $m_{\tilde{t}_1}$ is constrained by direct searches for stops as performed at the LHC. Searches are usually carried out assuming the dominance of the flavor-diagonal two-body stop decays

$$\tilde{t}_1 \to \tilde{\chi}^0_i t, \qquad\qquad \tilde{t}_1 \to \tilde{\chi}^+_j b \tag{5.6}$$

with large mass gaps between the particles. The neutralinos and charginos decay in cascades to SM particles and LSPs. The $\tilde{\chi}^0_1$s escape detection, yielding a collider signature including multiple high-p_T bottoms and tops plus $\not{E}_T$. A recent analysis of the CMS data from 2012 ($\mathcal{L}_{\text{int}} \approx 20\,\text{fb}^{-1}$, $\sqrt{s} = 8\,\text{TeV}$)—recorded in such a channel with one isolated lepton, jets, and $\not{E}_T$—yields a lower bound of $m_{\tilde{t}_1} \approx 650\,\text{GeV}$ [96], assuming a very light $\tilde{\chi}^0_1$ and a decoupling of the remaining sparticle spectrum.

Such bounds on stop masses far above the SM spectrum rely on a sufficient mass splitting between the key products of the decay chains to optimize the signal/background ratio. If all decay products are relatively soft, though, analyses become more involved and most frequently less sensitive [see Ref. [97] for the b-channel in (5.6), exemplarily].

An interesting scenario emerges if the decays in (5.6) is hypothesized to be closed kinematically, i.e. if

$$m_{\tilde{t}_1} < m_{\tilde{\chi}^0_1} + m_t \qquad\qquad m_{\tilde{t}_1} < m_{\tilde{\chi}^+_1} + m_b. \tag{5.7}$$

In this case, decay channels that are suppressed in the generic case can dominate. On tree level, these are generation-changing two-body decays or generation-conserving three-body decays such as

$$\tilde{t}_1 \to \tilde{\chi}^0_1 c, \qquad \tilde{t}_1 \to \tilde{\chi}^0_1 u, \qquad \text{and} \qquad \tilde{t}_1 \to \tilde{\chi}^0_1 b W^+. \tag{5.8}$$

Searches for stops assuming the dominance of the first decay mode have been performed by the experiments at LEP ($\sqrt{s} = 209\,\text{GeV}$) [99], Tevatron ($\sqrt{s} = 1.96\,\text{TeV}$) [100], and recently at the LHC ($\sqrt{s} = 8\,\text{TeV}$) [98]. The resulting exclusion limits are summarized

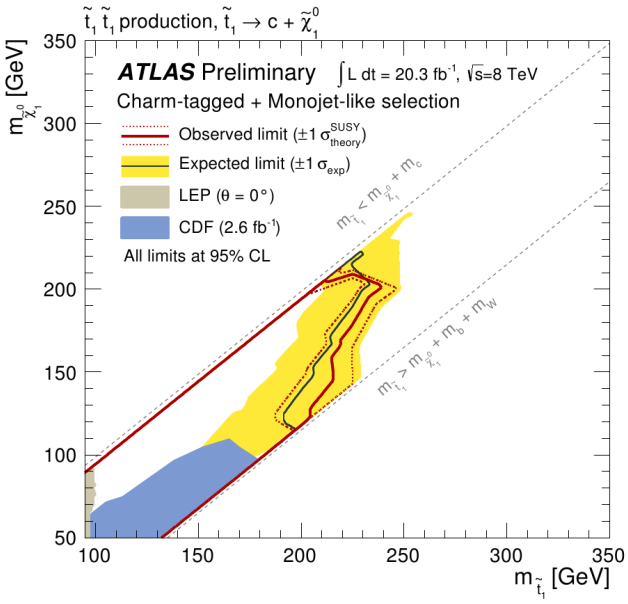

Figure 5.1: Exclusion limits in the $m_{\tilde{t}_1}$-$m_{\tilde{\chi}_1^0}$ plane. Figure from Ref. [98].

in Figure 5.1. The findings discussed in Section 5.3 are obtained prior to the LHC data taking, and assume only the CDF constraint to hold. In this case, the stop mass can be as light as the LEP bound ($m_{\tilde{t}_1} \approx 100\,\text{GeV}$) if

$$\Delta m = m_{\tilde{t}_1} - m_{\tilde{\chi}_1^0} \tag{5.9}$$

drops below $\mathcal{O}(30\,\text{GeV})$. The reason for this is the much cleaner experimental environment of the lepton collider LEP. Note that contrary to the CDF result, the ATLAS constraint as depicted in Figure 5.1 does not solely rely on the identification of the charmed decay remnants to signal a $\tilde{t}_1\tilde{t}_1^*$ event but also requires a hard mono jet from significant initial-state radiation [101]. It is therefore sensitive also for Δm much smaller than 30 GeV. Even taking the ATLAS search into account, $\tilde{t}_1$ constrained through (5.7) can be significantly lighter than in the generic case with flavor-diagonal decays.

5.2 FCNC stop decays

With MFV and a generic MSSM spectrum where stops decay predominantly through the flavor-diagonal channels in (5.6), a measurement of flavor–off-diagonal stop decays is challenging due to the generic CKM and down-type Yukawa suppression of the corresponding decay modes, as discussed below.

Generally, a tree-level charge-conserving two-body stop decay $\tilde{t}_1 \to \tilde{\chi}_1^0 u_I$ is governed by the following interaction Lagrangian:

$$\mathcal{L}_{u_I\tilde{t}_1\tilde{\chi}_1^0} = \overline{\tilde{\chi}_1^0}(y_{I,\text{L}}\,\text{P}_\text{L} + y_{I,\text{R}}\,\text{P}_\text{R})u_I\tilde{t}_1^* + \text{h.c.} \tag{5.10}$$

	$\tilde{t}_\mathrm{L}$	$\tilde{t}_\mathrm{R}$
$\tilde{H}_u^0$	$\lambda_c\lambda_b^2 V_{cb}V_{tb}^* \sim 4\times10^{-7}t_\beta^2$	$\lambda_c\lambda_t\lambda_b^2 V_{cb}V_{tb}^* \frac{Av_u}{\tilde{m}} \sim 4\times10^{-7}t_\beta^2 a_u$
Bino	$\sqrt{2}g'Y_Q\lambda_b^2 V_{cb}V_{tb}^* \sim 3\times10^{-6}t_\beta^2$	$\sqrt{2}g'Y_Q\lambda_t\lambda_b^2 V_{cb}V_{tb}^* \frac{Av_u}{\tilde{m}} \sim 3\times10^{-6}t_\beta^2 a_u$
Wino	$\sqrt{2}I_3\lambda_b^2 V_{cb}V_{tb}^* \sim 2\times10^{-5}t_\beta^2$	$\sqrt{2}I_3\lambda_t\lambda_b^2 V_{cb}V_{tb}^* \frac{Av_u}{\tilde{m}} \sim 2\times10^{-5}t_\beta^2 a_u$

Table 5.1: Minimally flavor violating couplings of the gauge eigenstates of $\tilde{t}$, c, and $\tilde{\chi}^0$. With $t_\beta \equiv \tan\beta$ and $a_u \equiv Av_u/\tilde{m}^2$. Y_Q (I_3) is the charm's hypercharge (3rd isospin component). From Ref. [69].

Here, the fields are mass eigenstates. The couplings y_L and y_R comprise the stop and neutralino diagonalization matrices Z_u and Z_N as well as EW gauge couplings and the Yukawa coupling λ_I of u_I:

$$y_{I,\mathrm{L}} = -g\sqrt{2}\left(\frac{\mathrm{s_W}}{6\,\mathrm{c_W}}\mathsf{Z}_N^{11*} + \frac{1}{2}\mathsf{Z}_N^{12*}\right)\mathsf{Z}_u^{I1*} - \lambda_I \mathsf{Z}_N^{14*}\mathsf{Z}_u^{I+3,1*} \tag{5.11a}$$

$$y_{I,\mathrm{R}} = -g\sqrt{2}\,\frac{2\,\mathrm{s_W}}{3\,\mathrm{c_W}}\,\mathsf{Z}_N^{11}\mathsf{Z}_u^{I+3,1*} - \lambda_I \mathsf{Z}_N^{14}\mathsf{Z}_u^{I1*}. \tag{5.11b}$$

With these definitions and $Y_I = \sqrt{|y_{I,\mathrm{L}}|^2 + |y_{I,\mathrm{R}}|^2}$, the partial decay rate for $\tilde{t}_1 \to \tilde{\chi}_1^0 u_I$ is

$$\Gamma(\tilde{t}_1 \to \tilde{\chi}_1^0 u_I) = \frac{Y_I^2 m_{\tilde{t}_1}}{16\pi}\left(1 - \frac{m_{\tilde{\chi}_1^0}^2}{m_{\tilde{t}_1}^2}\right)^2, \tag{5.12}$$

assuming that the quark mass is negligible for the phase space volume. The characteristic suppression of the flavor-mixing decay modes in MFV is apparent when analysing all relevant couplings of the suppressed decays such as $\tilde{t}_1 \to \tilde{\chi}_1^0 c$ ($I = 2$) in the gauge bases and the MFV-expansion (4.7). All couplings between the components of $\tilde{\chi}_1^0$, $\tilde{t}_{\mathrm{R/L}}$, and $c_{\mathrm{R/L}}$ are suppressed by at least [69]

$$\lambda_b^2 |V_{cb}V_{tb}^*| \sim 4\times10^{-5}\tan^2\beta. \tag{5.13}$$

The suppression can be even smaller by a factor of $\lambda_c \approx 10^{-2}$ if $\tilde{\chi}_1^0$ is higgsino-like, see Table 5.1 for a complete list. A replacement $V_{cb} \leftrightarrow V_{ub}$ yields equivalent expressions for the decay to $u_{\mathrm{R/L}}$, which thus is suppressed even further by a factor of $|V_{ub}/V_{cb}| \approx 10^{-1}$. In the transformation to the mass eigenbases, the suppression factors are inherited to Y_I.

Neglecting all numeric factors such as the expansion coefficients in (4.7) and assuming $m_{\tilde{t}_1} \gg m_t$, a rough upper estimate on the branching fraction of $\tilde{t}_1 \to \tilde{\chi}_1^0 c$ is given by the means of the factor in (5.13) for wino-like $\tilde{\chi}_1^0$ and $\tilde{\chi}_1^\pm$:

$$\mathcal{B}(\tilde{t}_1 \to \tilde{\chi}_1^0 c) \approx \frac{\Gamma(\tilde{t}_1 \to \tilde{\chi}_1^0 c)}{\Gamma(\tilde{t}_1 \to \tilde{\chi}_1^0 t) + \Gamma(\tilde{t}_1 \to \tilde{\chi}_1^+ b)} \sim 10^{-9}\tan^4\beta. \tag{5.14}$$

With extreme values of $\tan\beta$ ($\approx 60 = m_t/m_b$, evaluated at the top-scale [16]), this branching fraction can reach the %-level; with $\tan\beta = 10$, it is at the order of 10^{-5}. A rare FCNC stop decay in predominant $\tilde{t}_1\tilde{t}_1^*$ production would lead to a signature similar to high-p_T single-top production with additional $\not{E}_T$. (Single-top production is dominated by $u_I b \to d_J t$.) For an integrated luminosity of $\mathcal{L}_{\text{int}} = 100\,\text{fb}^{-1}$, 1.3×10^4 stop pairs with $m_{\tilde{t}_1} = 650\,\text{GeV}$ can be produced at $\sqrt{s} = 14\,\text{TeV}$ (cf. Figure 6.4 for cross sections). Therefore, even with optimal parameters and perfect signal separation from the background, a rare stop decay with MFV is not accessible at the LHC if $\tan\beta \lesssim 15$. In reality, the chances to observe a stop FCNC decay are significantly reduced by background, potentially small MFV expansion coefficients (see a discussion thereof in Ref. [69]), the neutralino composition, and the generic nuisances in MSSM FCNC events as listed in Chapter 3. We therefore assume that in a "typical" MFV scenario, a rare decay $\tilde{t}_1 \to \tilde{\chi}_1^0 c$ cannot be observed—unless $\tan\beta$ is extremely large.

Yet, the potential lightness of $\tilde{t}_1$ allows for an alternative scenario, where the chances to observe $\tilde{t}_1 \to \tilde{\chi}_1^0 c$ can in fact be larger the smaller $Y \equiv Y_2$ is. The spectrum could be structured such that the flavor-diagonal decay modes are kinematically closed. In this case the FCNC decay $\tilde{t} \to \tilde{\chi}_1^0 c$ can be the dominant stop decay channel. If this is so, the decay rate $\Gamma_{\tilde{t}_1}$ would be proportional to Y. Due to the smallness of Y, the decay rate may even be small enough so that light stops travels measurable distances inside the LHC detectors prior to their decays [69]. Lifetimes of $\mathcal{O}$(ps) are viable—the order of the lifetime of B-mesons.

To ensure the dominance of $\tilde{t}_1 \to \tilde{\chi}_1^0 c$ with small Y, the mass constraints in (5.7) need to be further tightened to also suppress the 4-body decays

$$\tilde{t}_1 \to \tilde{\chi}_1^0 b\, \ell^+ \nu_\ell \qquad \text{and} \qquad \tilde{t}_1 \to \tilde{\chi}_1^0 b\, u_I \bar{d}_I; \tag{5.15}$$

Δm, the mass difference between $\tilde{t}_1$ and $\tilde{\chi}_1^0$, must not exceed $\mathcal{O}$(few 5 GeV), where the explicit number dependents on the slepton and chargino spectra [69, 102]. With such a small $\Delta m \ll m_{\tilde{t}_1}$ and a dominant decay to $\tilde{\chi}_1^0 c$, the total decay rate of a stop with MFV is [69]

$$\Gamma_{\tilde{t}_1} = \frac{(Y\Delta m)^2}{4\pi m_{\tilde{t}_1}}. \tag{5.16}$$

In the next section, we will discuss the anatomy of this decay for stop pairs produced in association with top pairs.

5.3 Long-lived stops at the LHC—the $\tilde{t}_1\tilde{t}_1\bar{t}\bar{t}$-channel

The predominant production channel of light stops at a hadron collider (pp or $\bar{p}p$ with p=proton) is $\tilde{t}_1\tilde{t}_1^*$-pair production through gluon fusion and quark-antiquark annihilation. The signature of such a distop event with predominant stop decays to $\tilde{\chi}_1^0 c$ would consist of two (charmed) jets plus $\not{E}_T$, given that t $\tilde{\chi}_1^0$ is the LSP leaving the detector unseen. Though the cross section for light stop pair production is significant—up to hundreds of pb at the LHC with 14 TeV [103], see also Figure 6.4—the associated signature is subject to a pronounced SM background, dominated by $W(\to \tau\nu_\tau)$ +

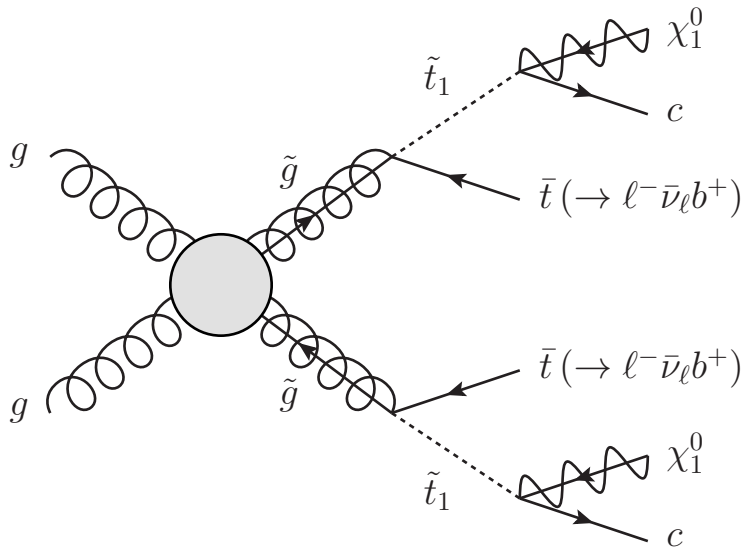

Figure 5.2: Schematic Feynman diagram for stop decays in the $\tilde{t}_1\tilde{t}_1\overline{t}\overline{t}$ channel. The blob summarizes the three graphs contributing to $gg \to \tilde{g}\tilde{g}$ at tree level (s-, t-, and u-channel). There is an equivalent graph for a quark-antiquark initial state (s-channel gluon exchange).

jets and QCD processes [104]. (In the latter case, $\not{E}_T$ is generated either by detector effects—by the detector's limited jet-energy resolution, for example—or by decay chains involving neutrinos.) As established in the last section, a small mass splitting between $m_{\tilde{t}_1}$ and $\tilde{\chi}^0$ is a necessity for a dominance of $\tilde{t}_1 \to \tilde{\chi}_1^0 c$. Since the small Δm leaves little kinetic energy for additional p_T of the stops' decay remnants, the signal cannot be discriminated well from the background by the means of cuts on the jets' p_T spectra. Higher-order effects such as significant initial-state radiation can allow to separate $\tilde{t}_1\tilde{t}_1^*$ events from SM background, though [101].

Instead of relying primarily on high-p_T cuts, we exploit the gluino's Majorana nature to discriminate MSSM events from their SM background [105] in the following. If the decays are allowed kinematically, gluinos can decay both via $\tilde{g} \to t\tilde{t}_1^*$ or $\tilde{g} \to \overline{t}\tilde{t}_1$ with equal branching ratios. Assuming that the rest of the squarks is very heavy, a pair of gluinos thus would decay with a cumulative branching fraction of 50% to $\tilde{t}_1\tilde{t}_1\overline{t}\overline{t}$ or $\tilde{t}_1^*\tilde{t}_1^* tt$, leading to a distinct signature of two like-sign tops (plus two soft charmed jets and $\not{E}_T$). Constrained to semi-leptonic top decays, this would result in a signal of

$$\ell^+\ell^+ + 4 \text{ jets} + \not{E}_T \quad \text{or} \quad \ell^-\ell^- + 4 \text{ jets} + \not{E}_T, \tag{5.17}$$

where $\ell = e$, μ and the two hardest jets are b-tagged. This signal is found to have a controlled SM background, dominated by $t\bar{t}$-pair production. [105] The signal decay chain is depicted in Figure 5.2.

We will discuss the stops decay characteristics, especially its displaced decay, in a numerical study, originally published in Ref. [2]. To simplify the analysis, we assume that all sparticles masses except those of $\tilde{g}$, $\tilde{t}_1$, and $\tilde{\chi}_1^0$ are above $\mathcal{O}$(TeV). We use

MadGrap/MadEvent 4.4.23 [106] to calculate cross sections and to generate $\tilde{t}_1\tilde{t}_1\overline{tt}$ and $\tilde{t}_1^*\tilde{t}_1^*tt$ events. We use the CTEQ6L1 parton distribution functions (PDFs) [107] and set the factorization and renormalization scales μ_F and μ_R to $m_{\tilde{g}}$. With $m_{\tilde{t}_1} = \mathcal{O}(100\,\text{GeV})$ and $m_{\tilde{g}} = 500\,\text{GeV}$ (1000 GeV), LHC cross sections of 5 pb (0.2 pb) arise, for a center-of-mass energy $\sqrt{s} = 14\,\text{TeV}$. Since $\tilde{t}_1$ is light compared to $\tilde{g}$, the cross section only shows a mild dependence on $m_{\tilde{t}_1}$. This is directly understandable in the narrow-width approximation (NWA) [108], approximating the gluinos to be produced on-shell. Due to the applicability of the NWA, we use K-factors of 1.5–2, found for $\tilde{g}\tilde{g}$ production [109], to account for presumably sizable next-to–leading-order (NLO) enhancements of the cross section. The cross sections are reduced by ~ 0.15 if a $\sqrt{s} = 10\,\text{TeV}$ is considered.

5.3.1 Stop kinematics and decays

The decay lengths d_i of both stops ($i = 1, 2$) in $\tilde{t}_1\tilde{t}_1\overline{tt}$ events on average are given by

$$d_i = \frac{(\beta\gamma)_i}{\Gamma_{\tilde{t}_1}} = \frac{4\pi p_i}{(\Delta m Y)^2}, \tag{5.18}$$

where $(\beta\gamma)_i = p_i/m_{\tilde{t}_1}$ is the boost factor related to the transformation of a resting $\tilde{t}_1$ to an inertial system where it has a 3-momentum with absolute value p_i. Thus, when the stop momentum is known, the decay length can be used to extract $(\Delta m Y)$.[1] If Δm were known also, the Y could be measured.

The characteristics of the stop decays inside a detector depend crucially on the stop kinematics—the stops' boost factors and the stops' angular distributions. For the benchmark point with $m_{\tilde{g}} = 500\,\text{GeV}$ (1000 GeV) and $m_{\tilde{t}_1} = 100\,\text{GeV}$, we show the distribution of the stop boost factors $(\beta\gamma)$ in Figure 5.3. In the vast majority of the sampled events (92%, for $m_{\tilde{g}} = 500\,\text{GeV}$), both stops have $(\beta\gamma) > 1$; i.e., they are significantly boosted. This approximate lower threshold is understandable qualitatively since a predominant contribution to the cross section stems from resonant gluinos with $m_{\tilde{g}} \approx 2(m_{\tilde{t}_1} + m_t)$. Upon gluino decay, the $\tilde{t}$ and $\bar{t}$ receive a kinetic energy roughly equal to their mass. This corresponds to $(\beta\gamma) \approx 1$, which is smeared out by the relative boost between the partonic center-of-mass system and laboratory system, and by the gluinos' kinetic energies.

In the events with $(\beta\gamma)_1 \geq (\beta\gamma)_2 > 1$, the majority of stops is in the central detector region with small pseudorapidities $|\eta_i| \lesssim 1$, see Figure 5.4. In 85% of the events for $m_{\tilde{g}} = 500\,\text{GeV}$, both stops would be inside the inner detectors of ATLAS and CMS [65, 110] with $|\eta_i| \leq 2.5$. As can be seen in Figure 5.5, these stops also are separated in $\delta\eta = |\eta_1 - \eta_2|$ and

$$\delta R = \sqrt{|\eta_1 - \eta_2|^2 + |\phi_1 - \phi_2|^2} \qquad \text{with} \quad |\phi_1 - \phi_2| \leq \pi, \tag{5.19}$$

where the ϕ_i are the azimuthal angle of the stop momenta in the laboratory frame.

[1] To be more precise, distributions of d_i and p_i have to be known to extract the averaged quantities.

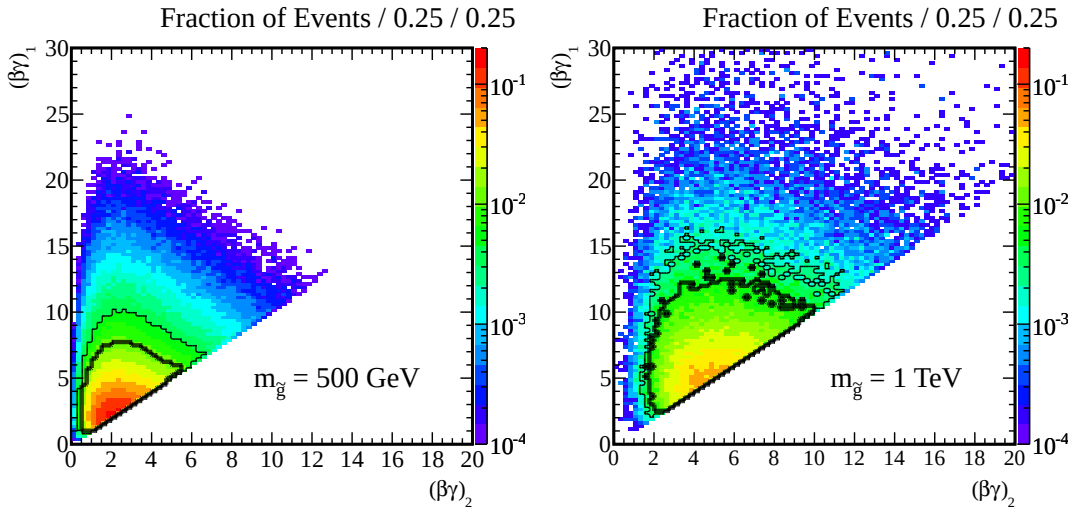

Figure 5.3: Distribution of stop boost factors in $\tilde{t}_1\tilde{t}_1\overline{t}\overline{t}$ events ($\sqrt{s} = 14\,\text{TeV}$) with $m_{\tilde{g}} = 500\,\text{GeV}$ (1 TeV) and $m_{\tilde{t}_1} = 100\,\text{GeV}$. $(\beta\gamma)_1 \geq (\beta\gamma)_2$ in each event. The tick (thin) contour contains 80% (90%) of all events. From Ref. [2].

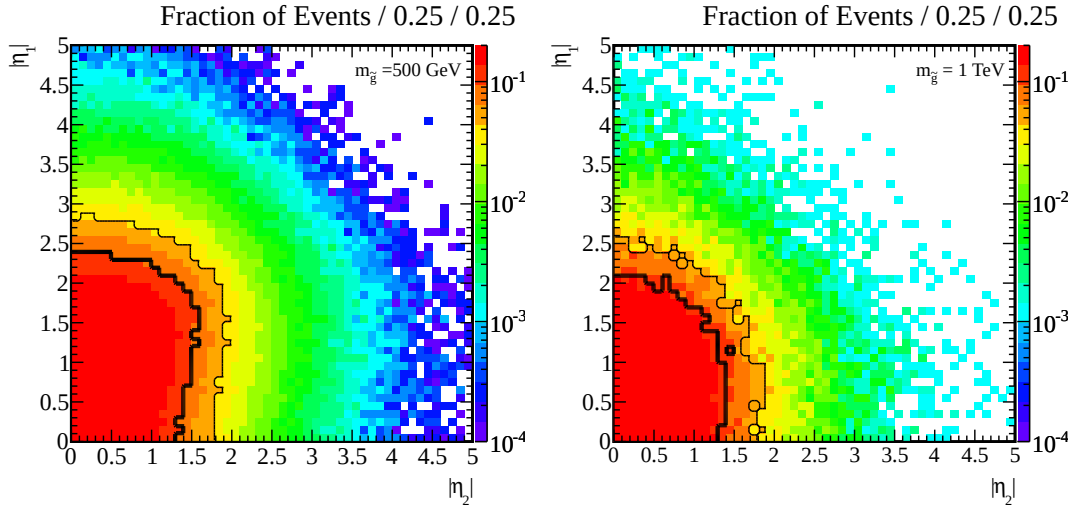

Figure 5.4: Distribution of the stop pseudo rapidities η_i with $(\beta\gamma)_1 \geq (\beta\gamma)_2 > 1$ in $\tilde{t}_1\tilde{t}_1\overline{t}\overline{t}$ events ($\sqrt{s} = 14\,\text{TeV}$) with $m_{\tilde{g}} = 500\,\text{GeV}$ (1 TeV) and $m_{\tilde{t}_1} = 100\,\text{GeV}$. The tick (thin) contour contains 80% (90%) of all events shown. From Ref. [2].

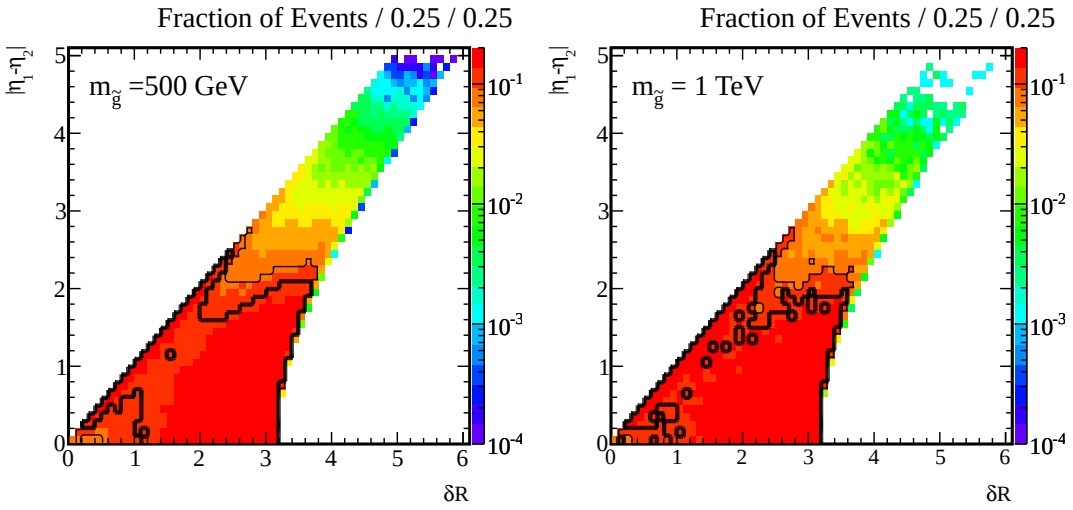

Figure 5.5: Angular distribution of the stops in $\tilde{t}_1\tilde{t}_1\bar{t}\bar{t}$ events ($\sqrt{s} = 14\,\text{TeV}$) with $m_{\tilde{g}} = 500\,\text{GeV}$ (1 TeV) and $m_{\tilde{t}_1} = 100\,\text{GeV}$, $(\beta\gamma)_1 \geq (\beta\gamma)_2 > 1$, and $|\eta_i| \leq 2.5$. The tick (thin) contour contains 80% (90%) of all events shown. From Ref. [2].

Based on the distributions in Figure 5.3, we know that the stops in our scenario typically have boost factors of $\mathcal{O}(1-10)$. With (5.18) this yields that a typical scale of the stops' decay lengths is a few hundred micrometers [2]:

$$d_i \approx 500\,\mu\text{m} \times \frac{(\beta\gamma)}{5} \left(\frac{100\,\text{GeV}}{m_{\tilde{t}_1}}\right) \left(\frac{0.05}{\Delta m/m_{\tilde{t}_1}}\right)^2 \left(\frac{10^{-5}}{Y}\right)^2 \tag{5.20}$$

Stops with decay lengths of this magnitude decay inside the LHC's beam pipe before they reach detector material.[2] Thus, what can be measured at best in these cases are impact parameters of the stops' decay products.

We define the transverse impact parameter b of a particle to be the distance of that point on the particle's extrapolated trajectory which is closest to the beam axis. (We neglect the bending effect of the magnetic field inside the detector and assume the trajectory to be a straight line; see also Figure A.1.) With this construction, the impact parameter constitutes a lower bound on the decay length, $b_i \leq d_i$. Even if the underlying parameters such as $(\Delta m Y)$ cannot be reconstructed completely, a mere observation of non-zero charm impact parameter, originating from a stop candidate, would strongly support MFV with the characteristically small coupling of stops to the other generations.

We sample the b distribution of the charmed stop-decay remnants in the $\tilde{t}_1\tilde{t}_1\bar{t}\bar{t}$ channel with $m_{\tilde{g}} = 500\,\text{GeV}$, $m_{\tilde{t}_1} = 100\,\text{GeV}$, and $\Delta m = 5\,\text{GeV}$. We use PYTHIA 6.4.19 [111] to hadronize parton-level events generated with MADEVENT. The stops' hadronization is performed with PYTHIA's string fragmentation model [111, 112] as is the

[2] Exemplarily, the innermost layer of the ATLAS pixel detector has a distance of $\sim 5\,\text{cm}$ to the beam axis [110].

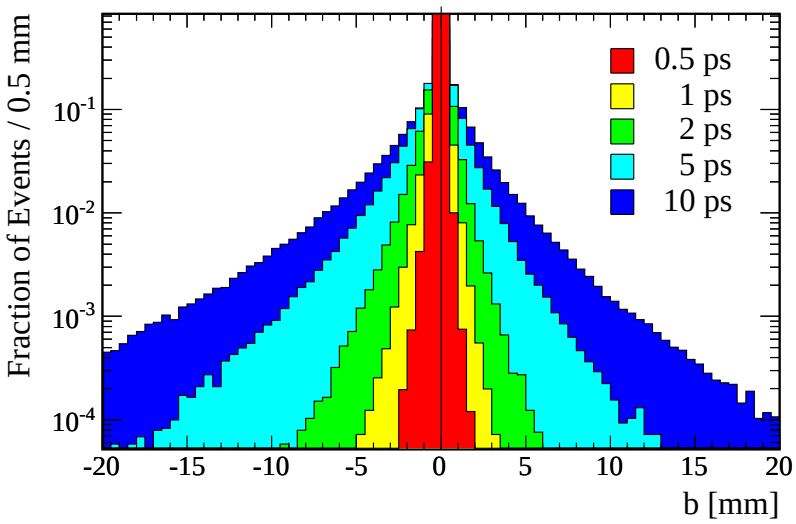

Figure 5.6: Distribution of transversal impact parameters b of the charmed stop-decay remnants in $\tilde{t}_1\tilde{t}_1\overline{t}\overline{t}$ events ($\sqrt{s} = 14\,\text{TeV}$) with $m_{\tilde{g}} = 500\,\text{GeV}$ and $m_{\tilde{t}_1} = 100\,\text{GeV}$. The b associated with the higher-p_T (lower-p_T) charm is chosen to be positive (negative). From Ref. [2].

hadronization of the stops' decay products. The decay itself is calculated in the spectator model with the individual stop lifetimes being sampled according to an exponential distribution with $\tau = 1/\Gamma_{\tilde{t}_1}$. Figure 5.6 shows the b-distribution for various average stop lifetimes. The sign of the impact parameters in the figure are assigned such that b is positive for the higher-p_T charm (b_1) and negative for the one with lower p_T (b_2). The asymmetry of the distribution $(\langle|b_1|\rangle - \langle|b_2|\rangle)/(\langle|b_1|\rangle + \langle|b_2|\rangle)$ is 24%. [2]

In the setup discussed above, the impact-parameter distribution of the charmed stop decay products scales linearly with the mean stop lifetime. We find [2]

$$\langle b\rangle \simeq 180\,\mu\text{m} \times \left(\frac{\tau}{\text{ps}}\right). \tag{5.21}$$

While the distribution of decay lengths is sensitive to the initial boost of the stop, these boosts' influence of the distribution of impact parameters is marginal. The reason for this is that the enlargement of the decay length in the laboratory frame associated with an additional boost is compensated by a corresponding suppression of the angle between the stop and charm trajectories in the calculation of the impact parameter. (This compensation is exact if m_c is negligible, see also Ref. [113].) The shape of the distribution and the result in (5.21) thus are to some extent independent of $m_{\tilde{g}}$ and $m_{\tilde{t}_1}$. The distribution is further only weakly dependent on Δm, since the angle between the stop and charm trajectories in the laboratory frame is independent on the charm momentum if m_c is negligible compared to Δm.

The flavor-changing coupling Y may well be significantly smaller than the typical

value of 10^{-5} associated with $\mathcal{O}(100\,\mu\text{m})$ decay distances in (5.20). Dependent on the numerical size of the coefficients b_i in the MFV expansion and on the wino and higgsino contributions to the neutralino, Y may be significantly smaller (cf. Table 5.1). Two additional scenarios may arise: With Y being one magnitude smaller,

$$\frac{\Delta m}{m_{\tilde{t}_1}} Y \lesssim 5 \times 10^{-8}, \tag{5.22}$$

the mean decay length becomes $\mathcal{O}(\text{few cm})$. In this case, the hadronized stops interact with detector material [114] and decay inside the inner detectors, optimally leaving tracks with kinks.

If the decay is suppressed even further,

$$\frac{\Delta m}{m_{\tilde{t}_1}} Y \lesssim 5 \times 10^{-9}, \tag{5.23}$$

the average decay length becomes $\mathcal{O}(\text{few m})$. In this scenario, the largest fraction of the hadronized stops would traverse the inner detector and eventually stop inside the hadronic calorimeter. A recent CMS analysis of 7-TeV and 8-TeV data [115] rules out stop masses below 818 GeV in this case.

5.3.2 Cuts and event count

As already stated, the $\tilde{t}_1\tilde{t}_1\overline{t}\overline{t}$ and $\tilde{t}_1^*\tilde{t}_1^*tt$ channels yield a particularly spectacular signal with controlled background if both tops decay semi-leptonically, cf. (5.17). In Ref. [105], the MSSM signal is isolated in this channel by the means of minimal-p_T cuts on the leptons (20 GeV) and jets (50 GeV), a cut on $\not{E}_T > 100\,\text{GeV}$, and the requirement that two combinations of leptons and b-jets yield invariant masses consistent with tops. In our scenario, the two jets stemming from the stop decays are considerably softer than those studied the benchmark scenario of Ref. [105], due to the smallness of Δm. We therefore expect a sizable drop in the event count through the 50-GeV cuts on these jets. Though the small momentum of few GeV the charm quark has in the stop rest frame can be enhanced through the boosts to the laboratory frame, a large number of charms remain soft with $p_T < 50\,\text{GeV}$. In Figure 5.7, we show the p_T distribution of the event-wise lower-p_T charms[3], generated with $m_{\tilde{g}} = 500\,\text{GeV}$ and $m_{\tilde{t}_1} = 100\,\text{GeV}$, for different values of Δm. As can be seen in the figure, even for $\Delta m = 30\,\text{GeV}$, only in $\sim 1/4$ of the events both charms pass a $p_T > 50\,\text{GeV}$ cut. A complete list of the corresponding fractions for the different values of Δm and different p_T cuts is enlisted in table. 5.2.

Constraining the signal to semi-leptonic top decays yields a reduction of the total event rate by a factor of $(2/9)^2 \approx 0.05$. With the signal cross section of 7.5 pb (0.4 pb) for $m_{\tilde{g}} = 500\,\text{GeV}$ (1000 GeV) and $m_{\tilde{t}_1} = 100\,\text{GeV}$, on can expect in total 36 000 (2 000)

[3]Note that we work with charms on quark-level here, while the analysis of the impact parameters based on charmed hadrons. The numbers presented here are considered to be a rough and simple estimate, without accounting for details such as jet algorithms.

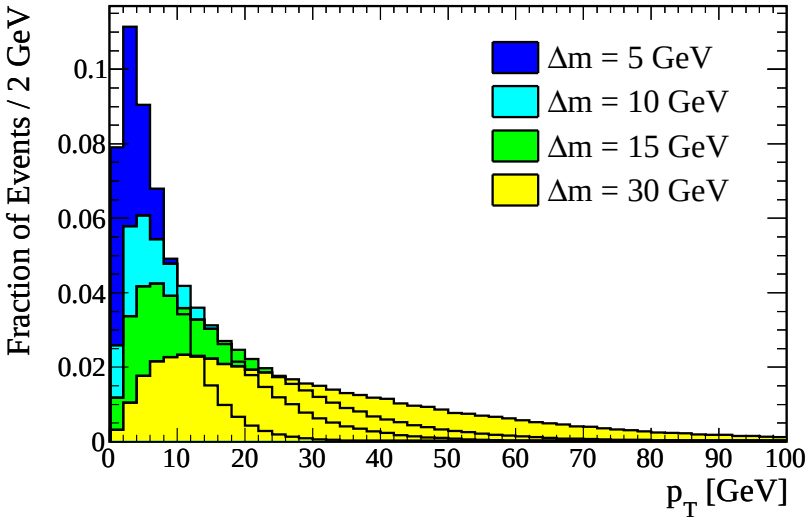

Figure 5.7: The p_T distribution of the lower-p_T charm stemming from stop decays in $\tilde{t}_1\tilde{t}_1\overline{t}\overline{t}$ events ($\sqrt{s} = 14\,\text{TeV}$) with $m_{\tilde{g}} = 500\,\text{GeV}$ and $m_{\tilde{t}_1} = 100\,\text{GeV}$ ($m_{\tilde{\chi}_1^0} = m_{\tilde{t}_1} - \Delta m$). From Ref. [2].

Δm \ p_T^{min}	30 GeV	35 GeV	40 GeV	50 GeV
5 GeV	0.4%	0.2%	0.08%	0.02%
10 GeV	7%	4%	2%	1%
15 GeV	18%	13%	9%	4%
30 GeV	45%	38%	32%	22%

Table 5.2: The fraction of $\tilde{t}_1\tilde{t}_1\overline{t}\overline{t}$ events with $m_{\tilde{g}} = 500\,\text{GeV}$, $m_{\tilde{t}_1} = 100\,\text{GeV}$, and $\sqrt{s} = 14\,\text{TeV}$ where both charm quarks survive a p_T cut for different values of p_T^{min} and Δm. From Ref. [2].

semi-leptonic $\tilde{t}_1\tilde{t}_1\overline{t}\overline{t}$ and $\tilde{t}_1^*\tilde{t}_1^*tt$ events at the LHC at 14 TeV for an integrated luminosity of 100 fb^{-1}. Requiring $\not{E}_T > 100\,\text{GeV}$ and $p_T^\ell > 20\,\text{GeV}$, $p_T^b > 50\,\text{GeV}$ (for both leptons and bottoms respectively) yields a reduction factor of ≈ 0.4 of the event count, which is further reduced to 0.26 assuming a 80% b-tagging efficiency. Thus the event count is reduced to about 10 000 (5000), without applying the charm-p_T cuts in Table 5.2. The latter account for the largest signal-event reduction, unless Δm is very large (30 GeV).

Requiring tagging of both charm jets would further reduce the event count significantly. Such an identification of the light flavor of the stop-decay remnants is not required to support the MFV hypothesis. The characteristic property of MFV tested here is the smallness of the stop's coupling to both light generations of up-type quarks. Finding soft jets not originating from the primary interaction vertex and being incompatible with typical displacement textures of SM b-jets and c-jets[4] would be sufficient for a first hint to MFV in the stop sector. Due to the softness of the stop decay remnants and the associated low track multiplicities inside the jets, a D-meson reconstruction could be feasible nevertheless.

5.3.3 Summary and recent data

We established that light stops in $\tilde{t}_1\tilde{t}_1\overline{t}\overline{t}$ and $\tilde{t}_1^*\tilde{t}_1^*tt$ events typically are well separated spatially and have significant boost factors $\beta\gamma \sim 1$–10. These allow that a long-lived $\tilde{t}_1$ decays significantly displaced from its production vertex. Dependent on the stop's lifetime, the decay can result in nonzero impact parameters of the decay products, tracks with kinks in inner detectors, or in out-of-time decays inside the hadronic calorimeter systems. For lifetimes of $\mathcal{O}(1\,\text{ps})$, impact parameters of $\mathcal{O}(180\,\mu\text{m})$ for the charmed decay remnants are expected. The latter are soft, so that minimal-p_T cuts on them result in significant reduction of the event count.

Since these findings in the $\tilde{t}_1\tilde{t}_1\overline{t}\overline{t}$ channel were published in Ref. [2], significant data samples have been collected at the LHC that constrain the parameter space of the model discussed here. On the one hand, the lower bound on $m_{\tilde{t}_1}$ is lifted from the LEP bound of approximately 100 GeV to 230 GeV in a preliminary 8-TeV ATLAS analysis [98]—see Figure 5.1. Additionally, an inclusive CMS search for anomalous tt-pair production [116] limits the excess of the cross section $\sigma(pp \to tt)$ cross section to values below 370 fb. This rules out $m_{\tilde{g}} \lesssim 600\,\text{GeV}$ for $\sigma(pp \to tt) = 1/4\,\sigma(pp \to \tilde{g}\tilde{g})$, based on a NLO calculation of $\sigma(pp \to \tilde{g}\tilde{g})$ with Prospino2 9.2.09 [109].

[4] An important ingredient in b-tagging algorithms is the characteristic displaced decay of the b quark [64].

6 Subsequent gravitational neutralino decay

In the last chapter, we established how the $\tilde{t}_1$-$\tilde{\chi}_1^0$-c coupling Y in a minimally flavor-violating MSSM may be measured by the means of a macroscopic stop lifetime. We discussed how the decay $\tilde{t}_1 \to \tilde{\chi}_1^0 c$, with $\tilde{\chi}_1^0$ being the undetectable LSP, may be observed at the LHC. Since the charmed stop decay products are generally soft due to the requisite small mass gap $\Delta m = m_{\tilde{t}_1} - m_{\tilde{\chi}_1^0}$, high-$p_T$ jets plus $\not{E}_T$ is generally not a suitable signature to analyse the stop decays in our scenario. We discussed that there are chances to measure the decay in the $\mathcal{O}(\alpha_s^4)$ process $pp \to \tilde{t}_1\tilde{t}_1\overline{t}\overline{t}$, in particular if both tops decay semi-leptonically. Because of the high order in α_s, the small semi-leptonic top branching ratio, and the minimal-p_T cuts on the resulting jets, the number of selected events is small. An investigation of the stop lifetime is possible probably only at the later phases of the LHC program.

The situation drastically changes if a very light gravitino $\tilde{G}$ were the LSP instead of $\tilde{\chi}_1^0$, which may be the next-to–lightest supersymmetric particle (NLSP). In this case, $\tilde{\chi}_1^0$ can decay through

$$\tilde{\chi}_1^0 \to \tilde{G}\gamma, \tag{6.1}$$

given a non-vanishing bino or wino component in $\tilde{\chi}_1^0$. If such decays take place inside a detector, hard and potentially isolated photons—in addition to $\not{E}_T$ from the gravitinos—would cleanly signal a BSM event. Having two hard photons, potentially not pointing to the primary interaction point, plus $\not{E}_T$ would even allow to separate $\tilde{t}_1\tilde{t}_1^*$ events from SM background, which is difficult in the scenario with a $\tilde{\chi}_1^0$ LSP. Since the SM background such small, already early (negative) LHC searches for deviations from the SM reduce the available parameter space significantly.

In this chapter we investigate the constraints on the MFV long-lived stop scenario, derived from D$\emptyset$ and early 7-TeV ATLAS data [117, 118], assuming mass hierarchies as sketched in Figure 6.1, Scenario A. The results are originally published in Ref. [3]. Before discussing the bounds in Section 6.3, we review $\tilde{t}_1$ and $\tilde{\chi}_1^0$ decays in the presence of a light gravitino in Sections 6.1 and 6.2.

6.1 FCNC stop decays revisited

Gravitational interactions are severely suppressed generally by inverse powers of the reduced Planck mass $\overline{\mathrm{M}}_{\mathrm{PL}}$; however, gravitino interactions can be competitive to the other interactions of the MSSM if the gravitino is very light. In this case $\tilde{G}$ dominantly interacts through its goldstino component, which couples to the MSSM particles with

$$(m_{3/2}\overline{\mathrm{M}}_{\mathrm{PL}})^{-1}; \tag{6.2}$$

i.e., a very small gravitino mass $m_{3/2}$ partly offsets the Planck suppression of the gravitino coupling. The factor in (6.2), setting the scale of gravitino interactions, is

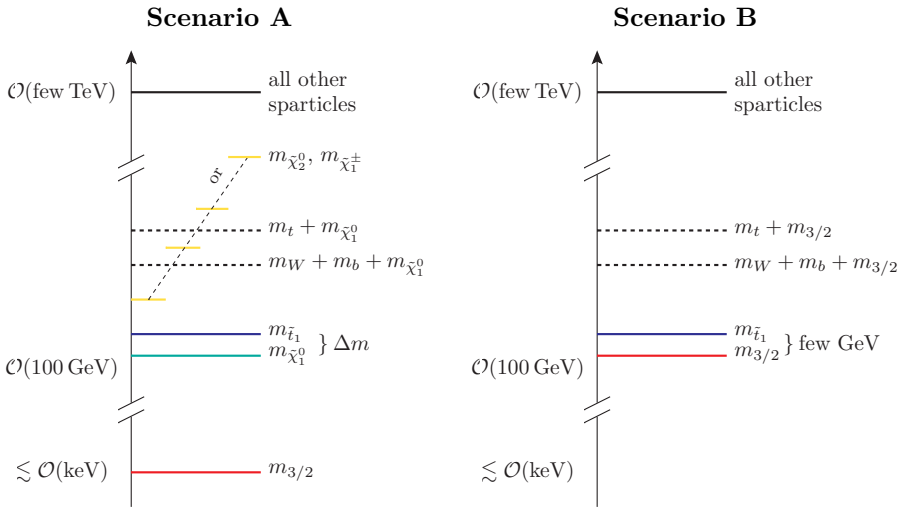

Figure 6.1: Mass hierarchies for which a dominant FCNC stop decay is discussed. Scenario B is disfavored, see the text.

universal for all MSSM particles. Therefore, if the neutralino decay in (6.1) is assumed to take place on the same time scale as the stop decay, $\tilde{t}_1 \to \tilde{G}X$ decays can be relevant for the stop decay pattern as well.

A stop $\tilde{t}_1$ may decay to gravitinos through the two-body decays

$$\tilde{t}_1 \to \tilde{G}u, \qquad \tilde{t}_1 \to \tilde{G}c, \qquad \tilde{t}_1 \to \tilde{G}t. \tag{6.3}$$

If the resonant decay to $\tilde{G}t$ is closed kinematically, the decay

$$\tilde{t}_1 \to \tilde{G}bW^+ \tag{6.4}$$

dominated by the exchange of a virtual t, can also contribute sizably.

Since the off-diagonal two-body decays in (6.3) are subject to the same MFV suppression as the equivalent decays to neutralinos, the flavor-diagonal decays usually dominate. Their partial decay rates are [119, 120]

$$\Gamma(\tilde{t}_1 \to \tilde{G}t) = \frac{1}{48\pi} \frac{m_{\tilde{t}_1}^5}{\overline{\mathrm{M}}_{\mathrm{PL}}^2 m_{3/2}^2} (1 - x_t^2)^4, \tag{6.5a}$$

$$\Gamma(\tilde{t}_1 \to \tilde{G}bW^+) = \frac{V_{tb}^2 \alpha_{\mathrm{em}}}{384\pi^2 \mathrm{s_W}^2} \frac{m_{\tilde{t}_1}^5}{\overline{\mathrm{M}}_{\mathrm{PL}}^2 m_{3/2}^2} \left[|\mathsf{Z}_u^{33}|^2 I(x_W^2, x_t^2) + |\mathsf{Z}_u^{63}|^2 J(x_W^2, x_t^2) \right], \tag{6.5b}$$

neglecting $m_{3/2}$ in the phase space integrals. Here, $x_A = m_A/m_{\tilde{t}_1}$. The contributing SM parameters can be found in Table 1.2. Due to the 3rd generation's decoupling from the lighter two generations in MFV, the stop rotation matrix entries satisfy $|\mathsf{Z}_u^{33}|^2 + |\mathsf{Z}_u^{63}|^2 \approx 1$. The phase space integrals I and J over W-boson and top propagators

can be found in (A.10) in the appendix. Note that the expression for the decay rate $\Gamma(\tilde{t}_1 \to \tilde{G}bW^+)$ is invalid for stop masses close to the top threshold, as it does not account for the non-zero top width—we only use this formula for $m_{\tilde{t}_1} < m_t$. The three-body decay rate is largest for a right-handed $\tilde{t}_1$, since the chirality-flipping top mass dominates the top propagator.

Of the two FCNC decays modes, $\tilde{t} \to \tilde{G}c$ is the dominant one due to $|V_{cb}| \approx 10 \times |V_{ub}|$. The decay rate can be written as [2]

$$\Gamma(\tilde{t} \to \tilde{G}c) = \frac{Y'^2}{48\pi} \frac{m_{\tilde{t}_1}^5}{\overline{\mathrm{M}}_{\mathrm{PL}}^2 m_{3/2}^2}, \tag{6.6}$$

where $Y' \sim \lambda_b^2 |V_{cb} V_{tb}^*|$ is defined equivalently to Y. For a bino-like $\tilde{\chi}_1^0$, Y and Y' are related according to [3]

$$\left|\frac{Y'}{Y}\right| \approx \frac{1}{\sqrt{2} g' Y_Q} \approx \begin{cases} 3 & \text{(right-handed } \tilde{t}_1\text{)} \\ 12 & \text{(left-handed } \tilde{t}_1\text{)} \end{cases}, \tag{6.7}$$

if $\tilde{t}_1$ is dominated by its R- or L-component. $Y_Q = \frac{1}{6}$ ($\frac{2}{3}$) is the hyper charge of $\tilde{t}_\mathrm{L}$ ($\tilde{t}_\mathrm{R}$).

Taking into account the gravitino modes only, we can construct a scenario equivalent to the one discussed in Section 5.2, with the $\tilde{\chi}_1^0$ LSP replaced by a $\tilde{G}$ LSP: We can suppress the flavor diagonal decay modes by demanding a small mass gap between a NLSP $m_{\tilde{t}_1}$ and a LSP $m_{3/2}$. The assumed mass hierarchy is depicted in Figure 6.1, Scenario B. With the required gravitino mass of $\mathcal{O}(m_{\tilde{t}_1})$, the stop decay length exceeds the length scales of a detector by far [2]. In consequence, the severe bounds for quasi-stable heavy new particles apply, constraining $m_{\tilde{t}_1}$ to be larger than 818 GeV [115].

In the following, we dismiss Scenario B and concentrate on the case where the relevant FCNC decay mode is $\tilde{t}_1 \to \tilde{\chi}_1^0 c$ with the mass relation

$$m_{3/2} \ll m_{\tilde{\chi}_1^0} \lesssim m_{\tilde{t}_1}, \quad \Delta m = m_{\tilde{t}_1} - m_{\tilde{\chi}_1^0} = \mathcal{O}(\text{few } 5\,\text{GeV}), \tag{6.8}$$

depicted in Figure 6.1, Scenario A. To identify the preferred region of the parameter space, where $\tilde{t}_1$ dominantly decays to $\tilde{\chi}_1^0 c$ and has a long life, we show the branching fraction $\mathcal{B}(\tilde{t}_1 \to \tilde{\chi}_1^0 c)$ and the stop lifetime $\tau_{\tilde{t}_1}$ in a Y-$m_{3/2}$ plane in Figure 6.2, for three different values of the stop mass and $\Delta m = 10\,\text{GeV}$. The figure is generated for a right-handed $\tilde{t}_1$, assuming the relation in (6.7) to hold. The figure does not change significantly when a left-handed $\tilde{t}_1$ is used, though. Gravitino masses larger than 4 keV are excluded if $\tilde{G}$ serves as a candidate for dark matter [33]. As visible from Figure 6.2, there is indeed a region compatible with a sizable $\mathcal{B}(\tilde{t}_1 \to \tilde{\chi}_1^0 c)$ and a macroscopic $\tau_{\tilde{t}_1}$, for all three stop masses shown and

$$m_{3/2} = \mathcal{O}(0.1\text{–}1\,\text{keV}), \qquad Y \lesssim \mathcal{O}(10^{-5}). \tag{6.9}$$

The minimal gravitino mass, necessary for a sizable $\mathcal{B}(\tilde{t}_1 \to \tilde{\chi}_1^0 c)$ grows with increasing $m_{\tilde{t}_1}$ because the widths for gravitational decays scale $\propto m_{\tilde{t}_1}^5$ while the width for $\tilde{t}_1 \to \tilde{\chi}_1^0 c$ scales $\propto m_{\tilde{t}_1}^{-1}$ only. Likewise, the weakness of the latter $m_{\tilde{t}_1}$ dependence is the reason for the weak $m_{\tilde{t}_1}$ dependence of $\tau_{\tilde{t}_1}$ in the large-Y region for the three stop masses in Figure 6.2.

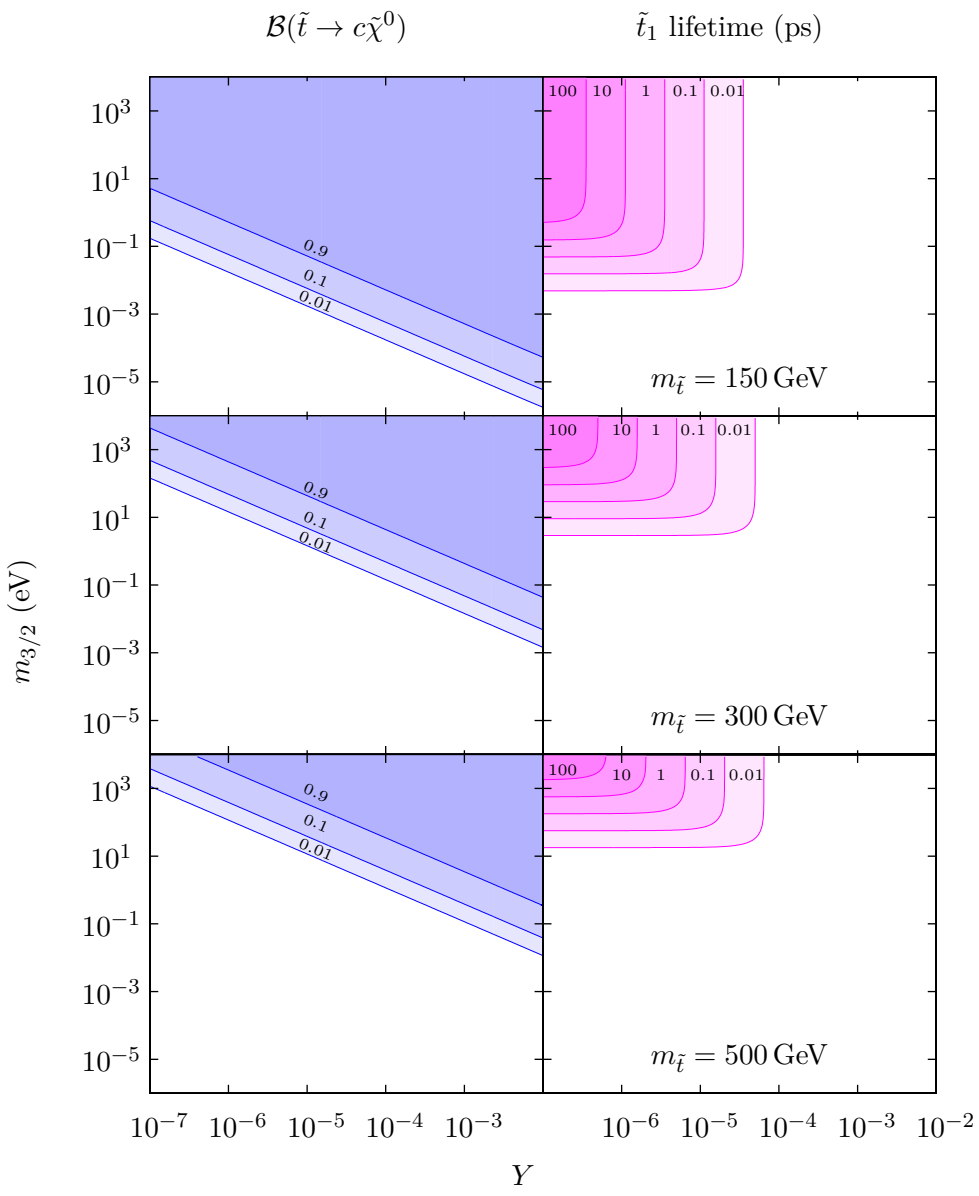

Figure 6.2: Isolines of light stop FCNC branching fractions (left) and lifetimes (right) in dependence of the gravitino mass $m_{3/2}$ and the flavor-changing coupling Y; for $m_{\tilde{t}_1} =$ 150 GeV, 300 GeV, and 500 GeV respectively (from top to bottom). A number in a shaded area indicate the minimal values allowed inside. Adapted from Ref. [3].

6.2 Neutralino decays

Comparing the value in (6.9) with the generic suppression factors in Table 5.1 yields that a wino-like $\tilde{\chi}^0$ is compatible with the scenario only for small $\tan\beta = \mathcal{O}(1)$, while there is more room for bino-like or higgsino-like $\tilde{\chi}^0$. A final judgement of the compatibility of (6.9) with different compositions of $\tilde{\chi}_1^0$ has to take the size of the MFV expansion parameters into account for a specific MFV model.

Irrespective of the favored value of Y in (6.9), a higgsino-like or wino-like $\tilde{\chi}_1^0$ is disfavored in our scenario for larger $m_{\tilde{\chi}_1^0}$ because of the mass hierarchies summarized in Figure 6.1, Scenario A, required for a dominance of $\tilde{t}_1 \to \tilde{\chi}_1^0 c$. If Δm in (6.8) exceeds m_b, there has to be a noticeable mass splitting

$$\Delta m_{\tilde{\chi}_1^\pm \tilde{\chi}_1^0} = m_{\tilde{\chi}_1^\pm} - m_{\tilde{\chi}_1^0} > \Delta m - m_b \tag{6.10}$$

to suppress $\tilde{t}_1 \to \tilde{\chi}_1^+ b$. Since the gaugino and chargino masses depend on the same MSSM parameters [see (2.10) and (2.9)], this mass relation constrains the neutralino composition.

For a light $\tilde{\chi}_1^0$ with $m_{\tilde{\chi}_1^0} = \mathcal{O}(m_Z)$, the required $\Delta m_{\tilde{\chi}_1^\pm \tilde{\chi}_1^0}$ can be generated with generic values of M_1, M_2, $\tan\beta$, and μ without much fine-tuning due to the $\mathcal{O}(m_Z)$ off-diagonal entries (blocks) in the mass matrices. However, with increasing $m_{\tilde{\chi}_1^0}$, $\Delta m_{\tilde{\chi}_1^\pm \tilde{\chi}_1^0}$ decreases for a wino-like or higgsino-like $\tilde{\chi}_1^0$ according to [121]

$$\Delta m_{\tilde{\chi}_1^\pm \tilde{\chi}_1^0} = \begin{cases} \mathcal{O}(m_Z^5/(M_1^2-\mu^2)^2) & \text{wino-like } \tilde{\chi}_1^0 \\ \mathcal{O}(m_Z^2/M_2) & \text{higgsino-like } \tilde{\chi}_1^0. \end{cases} \tag{6.11}$$

In the wino case with $m_{\tilde{\chi}_1^0} \approx |M_2| < |\mu|$, the degeneracy effect is most pronounced, and $\Delta m_{\tilde{\chi}_1^\pm \tilde{\chi}_1^0}$ drops below $\mathcal{O}(\mathrm{GeV})$ for $|\mu| \sim$ few 100 GeV unless there is a significant cancellation between the soft parameter M_1 and the superpotential parameter μ. For a bino-like $\tilde{\chi}^0$, no such parametrical mass degeneracy with a chargino state exists as there is no charged bino.

Our reason to introduce the light gravitino was to permit the decay of a $\tilde{\chi}_1^0$ to a photon. As the photon is a mixture of the SM's B and W gauge fields, the decay $\tilde{\chi}_1^0 \to \tilde{G}\gamma$ is only possible if $\tilde{\chi}^0$ has nonzero bino or wino components. In the light of the $\tilde{\chi}_1^0$-$\tilde{\chi}_1^\pm$ mass degeneracy discussed above, we focus on a bino-like $\tilde{\chi}_1^0$ in the following. As the photon is dominated by the B gauge boson, the bino-$\tilde{\chi}_1^0$ case is also the one where the branching ratio for $\tilde{\chi}_1^0 \to \gamma\tilde{G}$ is the largest. The bino two-body decay widths are [119, 122]

$$\Gamma(\tilde{\chi}_1^0 \to \gamma\tilde{G}) = \frac{{c_W}^2}{48\pi} \frac{m_{\tilde{\chi}_1^0}^5}{\overline{M}_{PL}^2 m_{3/2}^2}, \tag{6.12a}$$

$$\Gamma(\tilde{\chi}_1^0 \to Z\tilde{G}) = \frac{{s_W}^2}{48\pi} \frac{m_{\tilde{\chi}_1^0}^5}{\overline{M}_{PL}^2 m_{3/2}^2} \left(1 - \frac{m_Z^2}{m_{\tilde{\chi}_1^0}^2}\right)^4. \tag{6.12b}$$

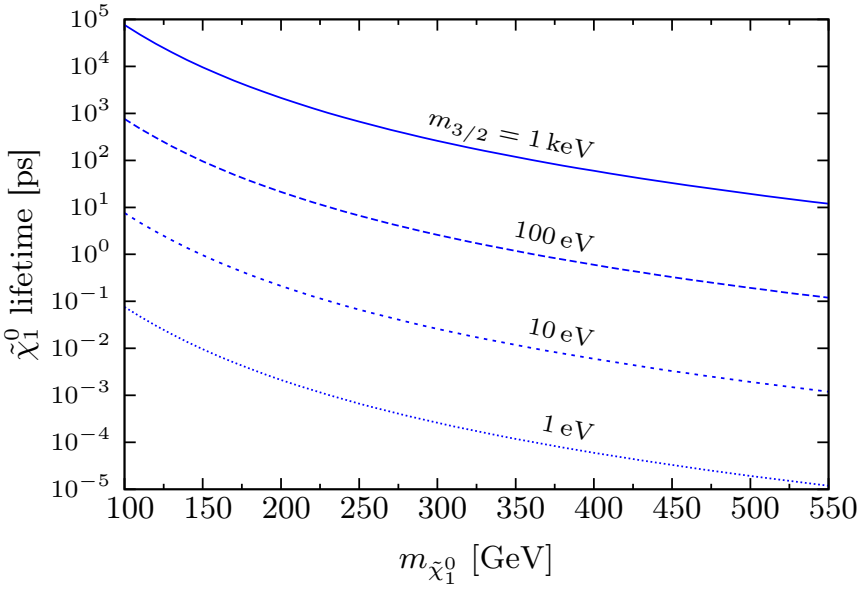

Figure 6.3: Lifetime of a bino-like $\tilde{\chi}^0$ in dependence of its mass, for several values of the gravitino mass $m_{3/2}$. Originally published in Ref. [3].

For reference, the lifetime of a bino-like $\tilde{\chi}_1^0$ is shown in Figure 6.3 for different values of $m_{3/2}$. As can be seen comparing Figures 6.2 and 6.3, requiring a stop dominantly decaying through $\tilde{t}_1 \to \tilde{\chi}_1^0 c$ with a $\mathcal{O}(\mathrm{ps})$ lifetime implies that $\tilde{\chi}_1^0$ has a lifetime of the same order of magnitude. We come back to this in Section 6.3.2.

6.3 Collider bounds from the $\tilde{t}_1\tilde{t}_1^*$-channel

The dominant source of light stops at pp or $p\bar{p}$ colliders is QCD-mediated $\tilde{t}_1\tilde{t}_1^*$ production. We show the NLO cross section for stop pair production, calculated with Prospino2 9.2.09 [103] and the built-in CTEQ6.6M PDFs [123], in Figure 6.4. With a decay chain of $\tilde{t}_1 \to \tilde{\chi}_1^0 c$ and $\tilde{\chi}_1^0 \to \tilde{G}(\gamma/Z)$, the stop pair decays to one of the following combinations:

$$\gamma\gamma + c\bar{c} + \tilde{G}\tilde{G}, \qquad \gamma Z + c\bar{c} + \tilde{G}\tilde{G}, \qquad ZZ + c\bar{c} + \tilde{G}\tilde{G} \tag{6.13}$$

As worked out in Section 5.3, the charms generated with a small Δm in $\tilde{t} \to \tilde{\chi}_1^0 c$ are generally too soft to be efficiently used in minimal-p_T-based event-selection cuts. This is true even more in the $\tilde{t}_1\tilde{t}_1^*$ channel, compared to the $\tilde{t}_1\tilde{t}_1 t\bar{t}$ channel, as the charms receive an extra boost from the gluino decay in the latter channel, see Figure 5.3. Only focusing on the bosons and gravitinos, bounds on our scenarios are imposed by searches in the $\gamma\gamma\not{E}_T$, $\gamma Z\not{E}_T$, and $ZZ\not{E}_T$ channels. As the bino's branching fraction to $\gamma\tilde{G}$ is the largest ($\geq 75\%$) and as there is few SM background, we focus on the $\gamma\gamma\not{E}_T$ signature.

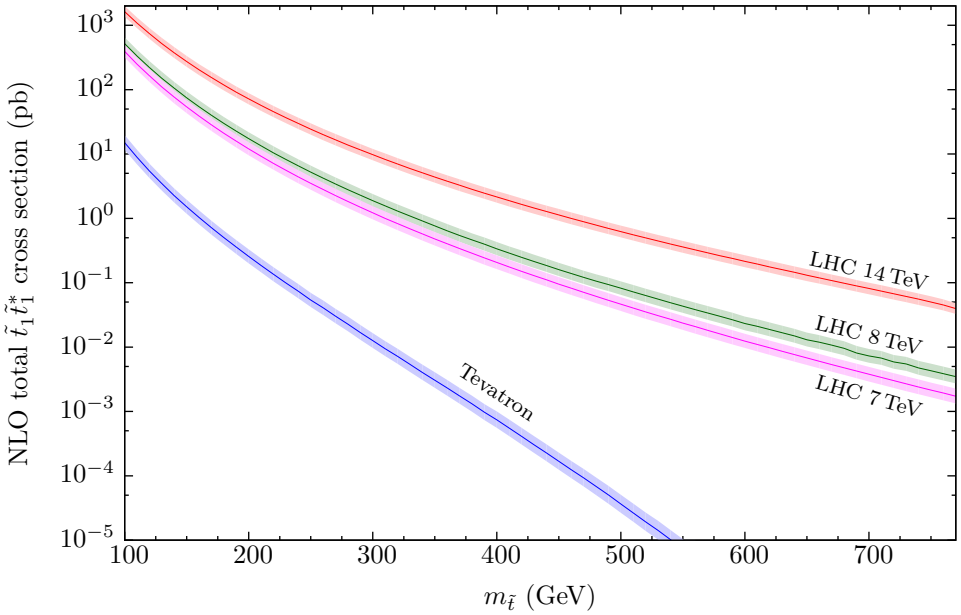

Figure 6.4: NLO cross sections for $\tilde{t}_1\tilde{t}_1^*$ pair production at hadron colliders with $\mu_R = \mu_F = m_{\tilde{t}_1}$. The bands correspond to $\frac{1}{2}m_{\tilde{t}_1} \leq \mu_R = \mu_F \leq 2m_{\tilde{t}_1}$.

SM background for $\gamma\gamma\not{E}_T$ can originate from hard processes with neutrinos in the final state (true $\not{E}_T$), or from mismeasurements in processes without original $\not{E}_T$ (fake $\not{E}_T$). In the case of true $\not{E}_T$, the dominant sources of background are the production of $W + \gamma$, W+jets, and $W + Z$, where the W and Z decay leptonically and where electrons or jets are misidentified as photons. The dominant source of fake $\not{E}_T$ are multijet events, where multiple jets are misidentified as photons. The smallness of the misidentification rate is partly off-set by the large cross section of multijet events.

To control the complexity of the discussion, we assume a split-SUSY spectrum, where all sparticles with the exception of $\tilde{G}$, $\tilde{\chi}_1^0$, and $\tilde{t}_1$ are very heavy and thus do not generate MSSM background (Scenario A in Figure 6.1). The sole potential source of MSSM background then is $\tilde{\chi}_1^0\tilde{\chi}_1^0$ pair production. With a vanishing higgsino-component of $\tilde{\chi}_1^0$, the cross section for $\tilde{\chi}_1^0\tilde{\chi}_1^0$ pair production vanishes even at $\mathcal{O}(\alpha_{\text{em}}^2\alpha_s)$, though. Therefore, with a pure bino-like $\tilde{\chi}_1^0$, there is essentially no MSSM background to our process.

6.3.1 Exclusion limits for $\mathcal{B}(\tilde{t}_1 \to \tilde{\chi}_1^0 c)$

Here we discuss exclusion limits on the branching fraction $\mathcal{B}(\tilde{t}_1 \to \tilde{\chi}_1^0 c)$ from D$\emptyset$ [117] and early 7-TeV ATLAS searches [118] in the $\gamma\gamma\not{E}_T$ channel (see also Table 6.1).

For each signal bin of the experimental studies the signal cross section for the $\gamma\gamma c\bar{c}\tilde{G}\tilde{G}$ final state can be calculated according to

$$\sigma_n = \epsilon_n \mathcal{B}(\tilde{t}_1 \to \tilde{\chi}_1^0 c)^2 \mathcal{B}(\tilde{\chi}_1^0 \to \tilde{G}\gamma)^2 \sigma^{\text{NLO}}_{\tilde{t}_1\tilde{t}_1^*}. \tag{6.14}$$

Search	Ref.	$\mathcal{L}_{\text{int}}$ (fb^{-1})	$\not{E}_T$ Bin [GeV]	Observed events	SM bgd events
D$\emptyset$	[117]	6.3 ± 0.4	$35 - 50$	18	11.9 ± 2.0
			$50 - 75$	3	5.0 ± 0.9
			> 75	1	1.9 ± 0.4
ATLAS	[118]	1.07 ± 0.04	> 125	5	4.1 ± 0.6

Table 6.1: ATLAS and D$\emptyset$ measurements and background (bgd) predictions in the $\gamma\gamma\not{E}_T$ channel constraining $\mathcal{B}(\tilde{t}_1 \to \tilde{\chi}_1^0 c)$.

Here n labels a signal bin, and $\sigma^{\text{NLO}}_{\tilde{t}_1\tilde{t}_1^*}$ denotes the total NLO cross section for stop pair production, calculated with Prospino2 using the CTEQ6.6M PDFs. ϵ_n denotes the efficiency for $\gamma\gamma\not{E}_T$ events to be registered in bin n. For the calculation of ϵ_n, 100 000 $\tilde{t}_1\tilde{t}_1^*$ events are generated with PYTHIA 6.4.25 [111] using the CTEQ6.6M PDFs, on a grid of stop masses with $\Delta m = 10\,\text{GeV}$. Using the hadron-level events, ϵ_n is calculated by the means of the simplified detector simulation Delphes 1.9 [124]. The details on the experimental cuts employed in this step are enlisted in Appendix B. Note that we assume here the displacement of the photons' origins from the primary interaction point is small enough to not significantly alter the photon identification efficiency.

Using (6.12) and (6.14) for the signal process and the background predictions of D$\emptyset$ and ATLAS (cf. Table 6.1), we calculate exclusion limits on $\mathcal{B}(\tilde{t}_1 \to \tilde{\chi}_1^0 c)$ at 95% confidence level. For this, we use the CL_S method [125] and use the prescription of Ref. [126] to project the ATLAS bound from $\mathcal{L}_{\text{int}} \approx 1\,\text{fb}^{-1}$ to $5\,\text{fb}^{-1}$. We treat errors on the luminosity and the background-event count as Gaussian nuisance parameters, but neglect theory uncertainties such as those of the PDF and scale choices.

The result is depicted in Figure 6.5, where the shaded regions are excluded. The ATLAS search gives bounds for stop masses up to $m_{\tilde{t}_1} = 560\,\text{GeV}$ (660 GeV projected). For larger masses a 100% branching fraction to $\tilde{\chi}_1^0 c$ is in agreement with the data [118]. The bounds show little dependence on the exact value of Δm as long it is in the range of few 5 GeV. It only contributes to the momentum the $\tilde{\chi}_1^0$s can acquire in the stop decays. As $m_{\tilde{\chi}_1^0} \gg \Delta m$, the variation of photon energies is small, as is the corresponding variation of the photons' p_T^{min}-cut efficiency.

In the region where only a very small $\mathcal{B}(\tilde{t}_1 \to \tilde{\chi}_1^0 c)$ is compatible with the $\gamma\gamma\not{E}_T$ searches, the dominant stop decay mode is $\tilde{t}_1 \to \tilde{G}t$, with $\mathcal{B}(\tilde{t}_1 \to \tilde{G}t) \approx 1 - \mathcal{B}(\tilde{t}_1 \to \tilde{\chi}_1^0 c)$. This region of the parameter space thus is sensitive to searches in the $t\bar{t}\not{E}_T$ channel. Such a search, with one top decaying semi-leptonically, is performed in $(1.07 \pm 0.04)\,\text{fb}^{-1}$ of 7-TeV data by ATLAS [127]. They observe 105 events with an SM expectation of 101 ± 16 events, after cuts. According to the study, masses above 300 GeV are compatible with any $\mathcal{B}(\tilde{t}_1 \to \tilde{G}t)$. For masses below 300 GeV, we calculate an exclusion

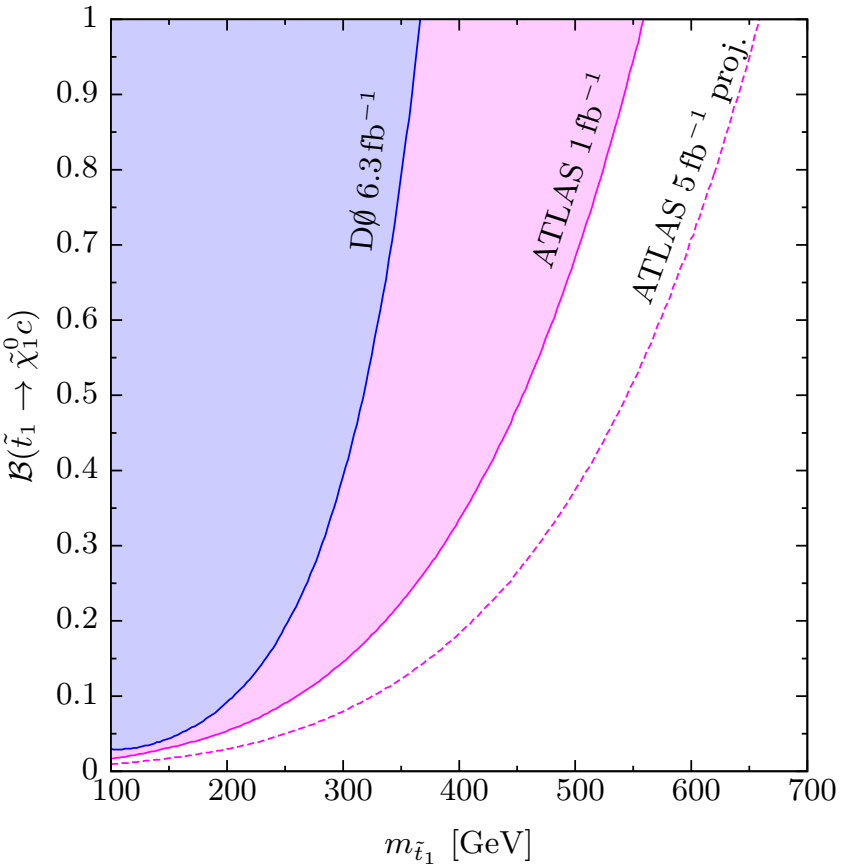

Figure 6.5: Bounds on the branching fraction $\mathcal{B}(\tilde{t}_1 \to \tilde{\chi}_1^0 c)$ assuming a bino-like $\tilde{\chi}^0$ and $\Delta m = 10\,\text{GeV}$, in dependence of the stop mass. The (colored) regions above the curves are excluded at 95% CL. From Ref. [3].

limit on $\mathcal{B}(\tilde{t}_1 \to \tilde{G}t)$ according to the procedure discussed in the beginning of this section; the adapted experimental cuts can be found in Appendix B. As the cut efficiency is drastically reduced for lighter stops, we find that also for $m_{\tilde{t}_1} < 300\,\text{GeV}$ this search does not constrain $\mathcal{B}(\tilde{t}_1 \to \tilde{\chi}_1^0 c)$.

6.3.2 Implications for Y, $m_{3/2}$, and the lifetimes

The bound in Figure 6.5 is largely independent on $m_{3/2}$ because of its negligible contribution to $\mathcal{B}(\tilde{\chi}_1^0 \to \tilde{G}\gamma)$. Yet, since $\mathcal{B}(\tilde{t}_1 \to \tilde{\chi}_1^0 c)$ does depend on $m_{3/2}$ and on Y, we can constrain the $m_{\tilde{t}_1}$-Y-$m_{3/2}$ parameter space with the exclusion limits just calculated. We do this by mapping the $m_{\tilde{t}_1}$-dependent limits on $\mathcal{B}(\tilde{t}_1 \to \tilde{\chi}_1^0 c)$ to limits on $m_{3/2}$ for characteristic values of Y (10^{-5}, 10^{-6}, and 10^{-7}). The result is shown in Figure 6.6. Here (5.16), (6.5), and (5.16) are used to calculate $\mathcal{B}(\tilde{t}_1 \to \tilde{\chi}_1^0 c)$ with $\Delta m = 10\,\text{GeV}$. Since (6.5b) diverges at $m_{\tilde{t}_1} \approx m_t$, we exclude the region $(m_t - 30\,\text{GeV}) \leq m_{\tilde{t}_1} \leq (m_t + 30\,\text{GeV})$ from the mapping and interpolate the result

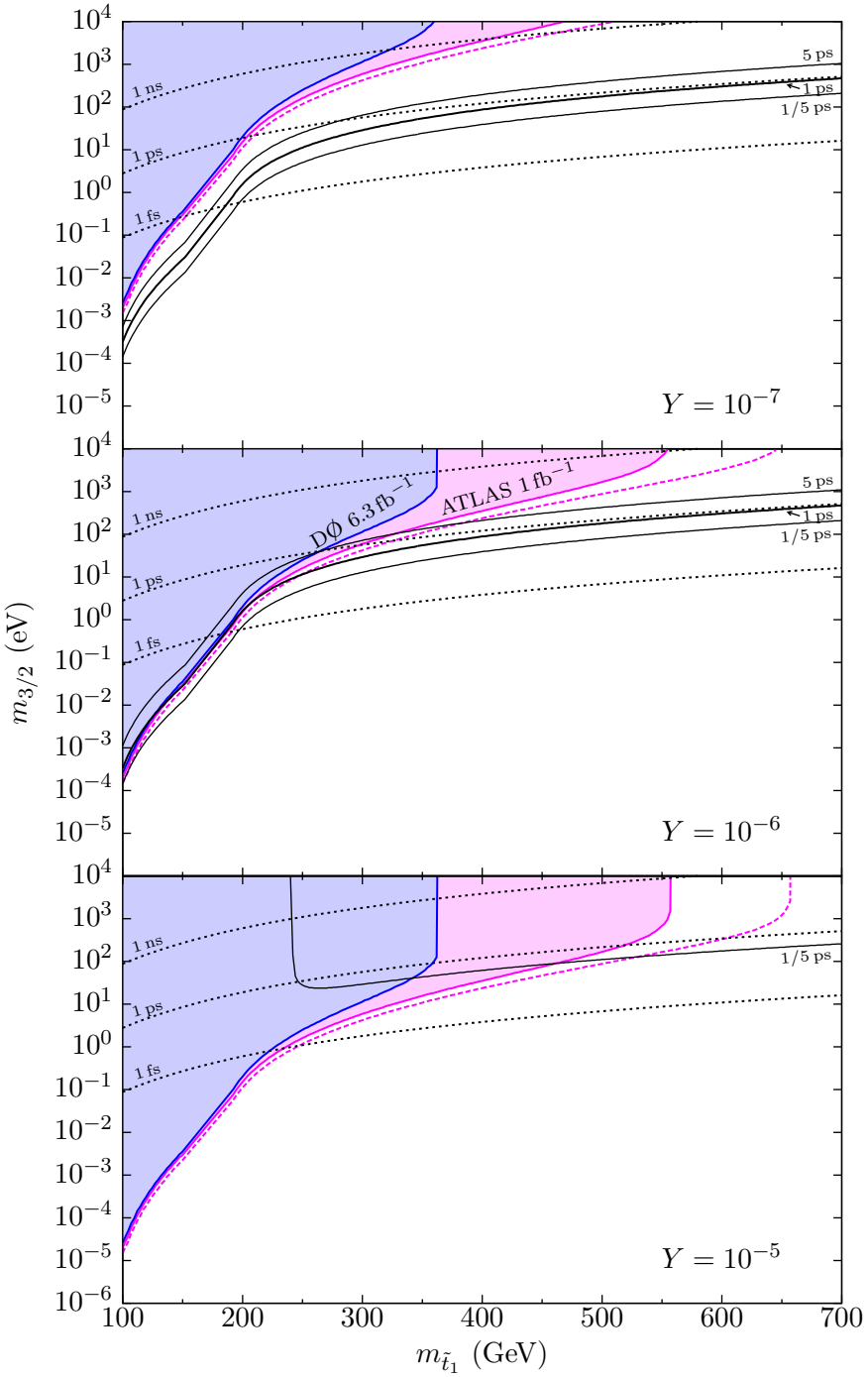

Figure 6.6: Cuts through the $m_{\tilde{t}_1}$-Y-$m_{3/2}$ parameter space for $Y = 10^{-7}$, 10^{-6}, and 10^{-5}. Pink (blue) region: excluded due to the 95%-CL bound on $\mathcal{B}(\tilde{t} \to \tilde{\chi}_1^0 c)$ derived from ATLAS [118] (DØ [117]) data. Dashed pink line: 5-fb^{-1} projection of the ATLAS region. Dotted black lines: $\tau_{\tilde{\chi}_1^0} = 1\,\text{fs}$, 1 ps, 5 ps. Solid black lines: $\tau_{\tilde{t}_1} = 1/5\,\text{ps}$, 1 ps, 5 ps. For $Y = 10^{-5}$, $\tau_{\tilde{t}_1}$ is smaller than 1 ps for all values of $m_{3/2}$. Adapted from Ref. [3].

in Figure 6.6. Up to Δm's influence on the cut-efficiency discussed above, Δm only contributes in the combination $(\Delta m Y)$ to the limits in Figure 6.6. Bounds for $\Delta m \neq 10\,\text{GeV}$ therefore can be obtained by rescaling Y.

In Figure 6.6, the limiting values of $m_{3/2}$ vary significantly with $m_{\tilde{t}_1}$. Yet, $m_{3/2}$ is the dominating factor for the $\tilde{\chi}_1^0$ and $\tilde{t}_1$ lifetimes $\tau_{\tilde{\chi}_1^0}$ and $\tau_{\tilde{t}_1}$ (for the latter only in the region where the FCNC decay $\tilde{t}_1 \to \tilde{\chi}_1^0 c$ has to be severely suppressed). Consequently, the allowed $\tilde{\chi}_1^0$ and $\tilde{t}_1$ lifetimes vary distinctly with $m_{\tilde{t}_1}$. For a first assessment, we add curves with constant $\tilde{\chi}_1^0$ lifetimes ($\tau_{\tilde{\chi}_1^0} = 1\,\text{fs}, 1\,\text{ps}, 5\,\text{ps}$; black dotted, bottom-up) and $\tilde{t}_1$ lifetimes ($\tau_{\tilde{t}_1} = 1/5\,\text{ps}, 1\,\text{ps}, 5\,\text{ps}$; black solid, bottom-up) in Figure 6.6. For $Y = 10^{-5}$, the largest value of Y, the FCNC decay width (5.16) alone is already sufficient to push $\tau_{\tilde{t}_1}$ below 1 ps. Thus, only the line for $\tau_{\tilde{t}_1} = 1/5\,\text{ps}$ can be drawn in this case.[1] Figure 6.6 allows to identify two different regions concerning the $\tilde{t}_1$ and $\tilde{\chi}_1^0$ lifetimes:

- For $m_{\tilde{t}_1} \lesssim 500\,\text{GeV}$, the stop must decay dominantly through its gravitino decay channels in order to comply with the $\gamma\gamma\not{E}_T$ searches. As $\tilde{G}$ couples with uniform strength to stops and neutralinos, both sparticles' lifetimes generically are of a common magnitude. The stop's dominant flavor-diagonal decay channels ($\tilde{t}_1 \to \tilde{G}bW^+$ for $m_{\tilde{t}_1} < m_t$ and $\tilde{t}_1 \to \tilde{G}t$ for $m_{\tilde{t}_1} > m_t$) are subject to a sizable phase space suppression that is nonexistent in the decay of a bino-like $\tilde{\chi}_1^0$. Consequently, for $m_{\tilde{t}_1} \lesssim 500\,\text{GeV}$, both particles' lifetimes fulfill

$$\tau_{\tilde{t}_1} \gtrsim \tau_{\tilde{\chi}_1^0}. \tag{6.15}$$

- For $m_{\tilde{t}_1} \gtrsim 500\,\text{GeV}$, the stop can decay dominantly through $\tilde{t}_1 \to \tilde{\chi}_1^0 c$. Coincidentally, in this $m_{\tilde{t}_1}$ regime, the phase space suppression becomes less pronounced; thus, $\Gamma(\tilde{t}_1 \to \tilde{G}t) \approx \Gamma_{\tilde{\chi}_1^0}$ where $\Gamma_{\tilde{\chi}_1^0} = 1/\tau_{\tilde{\chi}_1^0}$ is the total decay width of $\tilde{\chi}_1^0$. The lifetimes fulfill

$$\tau_{\tilde{t}_1} \lesssim \tau_{\tilde{\chi}_1^0}. \tag{6.16}$$

  For a domination of our signal decay $\tilde{t}_1 \to \tilde{\chi}_1^0 c$, the corresponding partial decay width must exceed $\Gamma(\tilde{t}_1 \to \tilde{G}t)$. Therefore we require

$$\tau_{\tilde{t}_1} \ll \tau_{\tilde{\chi}_1^0}. \tag{6.17}$$

The situation is visualized in Figure 6.7, where again colored regions are excluded. The black line labeled "$\mathcal{B} = 0$" depicts the smallest ratio that can be acquired, realized if both sparticles decay through their gravitino channels. The wearing-off of the phase space suppression of the gravitational stop decay widths forces this curve to approach the value of one for larger $m_{\tilde{t}_1}$. Figure 6.7 is largely insensitive to Y and the absolute values of the lifetimes—up to the decrease of the photon-identification efficiency, diminishing with increased displacement of the photon production vertex from the center of the detector. A more realistic simulation would account for these

[1] Note that for the two smaller values of Y, the exemplary $\tau_{\tilde{t}_1}$s are controlled by the gravitational decay modes. Therefore, the curves in the two uppermost panels coincide.

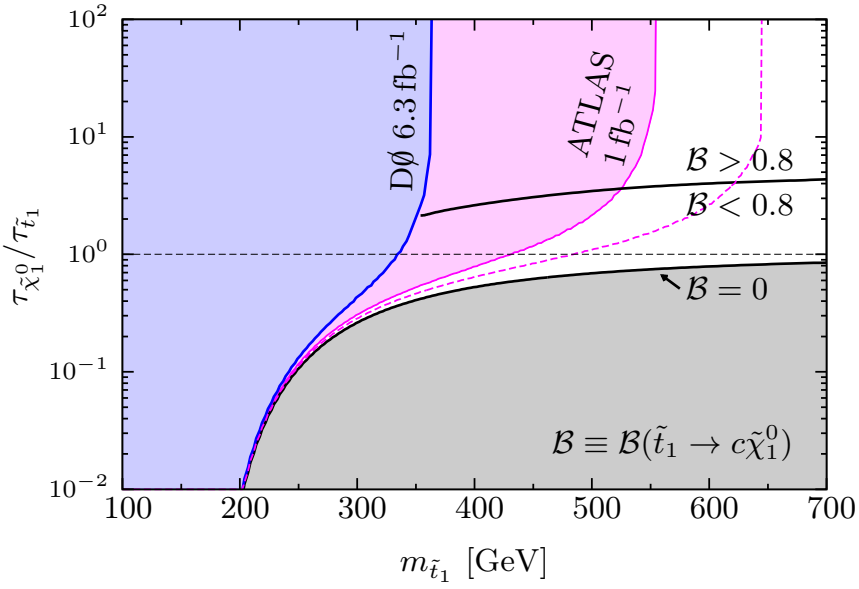

Figure 6.7: White region: allowed ratios of the light neutralino and stop lifetimes in dependence on $m_{\tilde{t}_1}$ (with $\Delta m = 10\,\text{GeV}$ and $Y = 10^{-6}$). Blue area: excluded by DØ data [117]. Pink area: excluded by ATLAS data [118] (dashed pink line: 5-fb^{-1} projection). Grey area: unphysical.

effects. More so as in the most interesting regime—where we can hope to access the stops flavor structure through its macroscopic decay length—the neutralino decay length necessarily has to be much larger than the one of the stop. An ATLAS simulations show that for several of the photon selection criteria used in the $\gamma\gamma\not{E}_T$ study discussed here, the efficiency to select a photon drops from $\mathcal{O}(85\%)$ to $\mathcal{O}(55\%)$ for longitudinal displacements of $\mathcal{O}(1\,\text{m})$ [64]. Yet, given this length scale, there is still room for photon displacements much smaller than that, still respecting (6.17) for stop decay lengths of $\mathcal{O}(\text{mm})$. (Note that only impact parameters of the photons are reconstructable, though, since in the decay $\tilde{\chi}_1^0 \to \tilde{G}\gamma$ all particles except the photons are undetectable.)

6.3.3 If there were a signal

If an excess in the $\gamma\gamma\not{E}_T$ channel were found, the events would had to be identified as originating from a $\tilde{t}_1\tilde{t}_1^*$ pair. It is not necessary to identify the charm in the non-pointing soft jet, originating from the stop decay, to support the MFV hypothesis. However to identify the $\tilde{t}_1\tilde{t}_1^*$ pair in the first place, it may be necessary. ATLAS expects the required c-tagging efficiency to reach up to 40% [68]. The overall $\tilde{t}_1$-$\tilde{\chi}_1^0$ mass could be reconstructed from the γ spectra by the means of the contratransverse mass distribution (M_{CT}^2) [128] for instance. The distribution of γ impact parameters, could be used to extract $m_{3/2}$. With $m_{\tilde{t}_1}$ and $m_{3/2}$, the distribution of $\tilde{t}_1$ impact parameters or decay distances can then be used to access ($\Delta m Y$).

At the time of writing, due to the outstanding performance of the LHC, the experiments were able to collect data samples much larger than the $1\,\mathrm{fb}^{-1}$ of ATLAS data used to derive the bounds discussed here. For the $\gamma\gamma\not{E}_T$ channel, ATLAS published searches in $5\,\mathrm{fb}^{-1}$ of 7-TeV data [129, 130], for pointing and non-pointing photons. Likewise, CMS published a search for multiple photons plus jets plus $\not{E}_T$ in $5\,\mathrm{fb}^{-1}$ of 7-TeV data [131] and a search for long-lived neutralinos decaying to photons [132].

These improved searches further constrain the available parameter space. They do not alter the overall picture significantly—cf. our 5-fb^{-1} projection: With a bino-like $\tilde{\chi}_1^0$ decaying to a photon, the "light" stop must have a mass larger than 500 GeV for decay $\tilde{t}_1 \to \tilde{\chi}_1^0 c$ to dominate. This dominance is mandatory for our central idea that we can measure a part of the MSSM's flavor structure that is inaccessible otherwise. In our scenario, within the stop mass region above $\mathcal{O}(500\,\mathrm{GeV})$, the neutralino lifetime must significantly exceed the stop's lifetime.

7 Conclusion of Part II

The unknown origin of flavor-symmetry breaking is one of the major puzzles in the SM and contributes the largest number of free parameters to the theory. The need for an explanation of the Yukawa structure is even more urgent now that a Higgs boson is observed, further supporting the Higgs mechanism experimentally.

The observation of sparticle states heralding a broken spacetime supersymmetry can help to identify the source of flavor-symmetry breaking. With approximately twice the particle content of the SM, the MSSM introduces copious new flavor-breaking couplings whose measurement would provide insight in both SUSY breaking and flavor breaking. Precision measurements of FCNC processes such as meson oscillations and rare decays constrain the structure of these new couplings at scales much smaller than the typical mass scale of the sparticles. Yet, these constraints are dependent on the overall SUSY mass scale and are insensitive to parts of the up-type squark mass matrix [$(\delta^u_{\mathrm{LL}})_{23}$, $(\delta^u_{\mathrm{RR}})_{I3}$, and $(\delta^u_{\mathrm{RL}})_{I3}$ for $I = 1, 2$]. We examined how these couplings can be constrained assuming that they are particularly small, as predicted in the MFV flavor pattern.

Stop branching fractions, sensitive to the unconstrained couplings, are expected to be at most of $\mathcal{O}(10^{-9} \times \tan^4\beta)$ in MFV for a generic sparticle spectrum. In the light of the lower bounds on the stop masses imposed by the LHC data from 2012, such a branching fraction is not accessible at the LHC unless $\tan\beta$ is very large. We examined a stop-lifetime measurement as an alternative to branching fraction measurements. A lifetime determination can be feasible if the stop's flavor-mixing is particularly small, as predicted in MFV. For a $\mathcal{O}$(ps) lifetime, the stops' decay remnants are expected to have transverse impact parameters of $\mathcal{O}(100\,\mu\mathrm{m})$. This scenario requires a close-to degeneracy between the masses of $\tilde{t}_1$ and $\tilde{\chi}^0_1$, constituting theoretical and experimental challenges.

On the experimental side, the SUSY events have to be efficiently separated from SM background. Since the stop's decay products are low energetic, minimal-p_T cuts on the hadronic remnants are ineffective and generally do not suffice for a signal separation. Yet a very clean signal is required to suppress bottom decays that also generate displaced charmed jets similar to displaced stop decays. We investigated two options for signal separation here: Firstly we exploited the gluino's Majorana nature to suppress the a SM signal. Secondly we hypothesized the existence of a light gravitino that allow for neutralino decays to hard photons with very little SM background. The first option is plagued from small event numbers, which is not the case for the second option. The latter requires a more fine-tuned sparticle spectrum but is testable with early LHC data. The mass of a stop dominantly decaying as $\tilde{t}_1 \to \tilde{\chi}^0_1 c \to \gamma\tilde{G}c$, for a bino-like $\tilde{\chi}^0_1$, is constrained to values above 560 GeV already by $1\,\mathrm{fb}^{-1}$ of 7-TeV data in the $\gamma\gamma\not{E}_T$ channel. A third option to isolate the signal, would be to require a hard

mono jet with maximum-p_T cuts on all other objects following Ref. [101]. This method is not discussed here in detail, but has been proved in an experimental search [98] to efficiently separate stop events from SM background irrespective the smallness of the $\tilde{t}_1$-$\tilde{\chi}_1^0$ mass difference.

A model-building challenge is to explain why the neutralino mass is almost degenerate with the light stop's mass. We required the smallness of $\Delta m = m_{\tilde{t}_1} - m_{\tilde{\chi}_1^0}$ to ensure the sensitivity of the stop lifetime to the flavor-structure. Such a small Δm is also favorable cosmologically, because it can reduce the $\tilde{\chi}_1^0$ CDM density through $\tilde{\chi}_1^0$-$\tilde{t}_1$ co-annihilation to the phenomenologically preferred value [133]. This co-annihilation usually is discussed in supergravity (SUGRA), and the reduction is most relevant for a bino-like $\tilde{\chi}_1^0$.

In the R-parity conserving MSSM, the tight bounds on the masses of gluinos and the first two generation's squarks, obtained from the 2011 and 2012 LHC data, push a common squark mass scale to the multiple-TeV order. The mass of the observed Higgs boson is large for a light MSSM Higgs, but for an average stop-mass scale much larger than 1 TeV, an increased fine-tuning is required to generate such a Higgs in the MSSM (the little hierarchy problem). The individual bounds on the stop masses are much weaker than on those on the other squarks, especially for the kind of spectra we discussed. To retain SUSY as a solution to the hierarchy problem, split-SUSY models, where parts of the spectrum are much lighter than the rest, consequently increasingly gain attention, cf. Ref. [134], e.g.

It may be that a light stop is the only supersymmetric particle that can be observed at the LHC along with an undetectable LSP. If this is so, the stop's flavor decomposition along with the mass is a precious messenger of the origin of SUSY-breaking and flavor-violation.

Part III

Drell-Yan leptons with asymptotically safe gravity

8 Introduction: Gravity effects at colliders

In Chapter 2, discussing the ADD model, we saw that the true scale of quantum gravity could be at the weak scale $\Lambda_{\mathrm{EW}} \sim 1\,\mathrm{TeV}$, not at the 4-dimensional Planck scale $\mathrm{M_{PL}} = 1/\sqrt{G_{\mathrm{N}}} \sim 10^{16}\,\mathrm{TeV}$ which is set by Newton's constant. In a $(4+n)$-dimensional theory, with n additional spatial dimensions compactified to a torus, the scale of quantum gravity $\mathrm{M}_\star$ is given by

$$\mathrm{M}_\star^{n+2} = \frac{\mathrm{M_{PL}^2}}{8\pi r^n}, \tag{8.1}$$

where r is the radius of the torus, assumed here to be universal. For $n \geq 2$, $\mathrm{M}_\star$ is of $\mathcal{O}(\mathrm{TeV})$ if r is below a few micrometers, see also Table 2.2. Since the SM is probed at length scales much smaller than $\mathcal{O}(\mu\mathrm{m})$, it is assumed to be confined on a 4-dimensional brane, but gravity fundamentally can be $(4+n)$-dimensional.

With the true Planck scale $\mathrm{M}_\star$ at the TeV-scale, gravity effects can be visible at the LHC. Since $1/r \ll \mathrm{M}_\star$, these effects are those of the fully $(4+n)$-dimensional gravity. Two kinds of effects frequently are discussed in the literature:

1. Particle scattering with virtual-graviton exchange or real-graviton production.
2. Production and decay of mini black holes (BHs).

They are usually, most robustly discussed in very distinct scenarios:

Effects of type 2, BH phenomena, are well understood in a semi-classical limit where the black-hole mass m_{BH} is larger than $M_{\mathrm{min}} = \text{few} \times \mathrm{M}_\star$ [135–137]. The parton-level cross section for the production of a spin-less BH then can be approximated by geometric considerations as [137]

$$\hat{\sigma} \approx \pi r_c^2(m_{\mathrm{BH}}^2 = \hat{s})\Theta(\sqrt{\hat{s}} - M_{\mathrm{min}}), \tag{8.2}$$

where $r_c(m_{\mathrm{BH}})$ is the BH's Schwarzschild radius [cf. (A.14)], $\sqrt{\hat{s}}$ the parton-level center-of-mass energy, and Θ the Heaviside function. BHs thus are best understood in the limit $\sqrt{\hat{s}} \gg \mathrm{M}_\star$.

Effects of type 1, real or virtual graviton contributions to SM scattering processes, generally are well-defined if the interactions take place in the low-energy limit of gravity as described in Section 2.2.2. This is the regime where gravitons are introduced as gravitational degrees of freedom in the first place. Real-graviton production is in this low-energy limit as long as the mass of the heaviest KK graviton that can be produced is well below the transition scale to the fundamental gravitational regime. The situation is different in case of virtual-graviton scattering, where complete KK towers contribute to the amplitudes. Involving arbitrarily high graviton masses, these KK sums are sensitive to the unknown high-energy regime of gravity and typically diverge for $n \geq 2$.

In the full theory, the KK sums supposedly would be regularized by the high-scale dynamics. Assuming such a regularization, a KK tower of virtual gravitons propagators can be taken as a finite, effective 4-SM-particle coupling $\propto 1/\Lambda_{\text{eff}}^4$ in the low-$\hat{s}$ limit, i.e. for $\sqrt{\hat{s}} \ll \Lambda_{\text{eff}}$.

Both signatures, BH production and graviton interactions, have in common that they are delicate to describe in regions where a full theory of strong quantum gravity is necessary to describe the phenomena. Yet this is a regime that could be probed at the LHC. With $M_\star$ at the TeV-scale, we have the unique opportunity to explore quantum gravity at the LHC, but there is no consents on how an appropriate theory may look like fundamentally. Even in the well-defined regimes sketched above, cross-section predictions steeply depend on the order-of-magnitude cut-off scales M_{min} and Λ_{eff}.

In the following, we discuss virtual-graviton scattering in one of the contending theories for fundamental quantum gravity, the Asymptotic-Safety Scenario. We introduce this scenario in Chapter 9 and discuss its effect on amplitudes for virtual-graviton exchange in Chapter 10. We apply the results to $pp \to \ell^+\ell^-$ scattering—the Drell-Yan process—at the LHC in Chapter 11. There, we also derive bounds on the model's parameters from 8-TeV CMS data using a new implementation of the process to PYTHIA 8. The asymptotically safe Drell-Yan process has been discussed also in Ref. [138]. Asymptotically safe real-graviton emission is discussed in Ref. [139], and the phenomenology of asymptotically safe BHs in Ref. [140].

9 Asymptotic Safety

In classical gravity, the homogeneous Einstein equation can be cast into a wave equation for small metric perturbations h_{AB}. It is straight forward conceptually to associate the solutions of this equation with quanta called gravitons, developing a theory of quantum gravity. Unfortunately, this quantum Einstein Gravity is perturbatively non-renormalizable, as has been established in Ref. [141] for pure gravity at the two-loop order and in Ref. [142] for gravity plus various kinds of matter at the one-loop order.

The perturbative non-renormalizability looms in the mass dimension of Newton's constant $G_{\mathrm{N}}^{(d)}$, which is $2-d$ in d dimensions and thus negative for $d > 2$. At a Feynman vertex involving $G_{\mathrm{N}}^{(d)}$ (see Ref. [54, 143] for Feynman rules, e.g.), the coupling's negative mass dimension is offset by a corresponding power of the involved momenta. In loop graphs, with integrals over all internal momenta, these extra powers of loop momenta lead to a ultraviolet (UV) behavior worse than that of established perturbatively renormalizable theories with dimensionless couplings such as quantum electrodynamics (QED).

9.1 A renormalizable theory of quantum gravity

Being perturbatively non-renormalizable, quantum Einstein Gravity could be free of UV divergences nevertheless, as pointed out by Weinberg [144]. The effective average action $\Gamma_{(\mu)}$, defining the quantum theory at a renormalization scale μ, could stay finite if evolves into a scale-invariant, finite-dimensional UV regime under RG running. $\Gamma_{(\mu)}$, interpreted as a vector in a "theory space" (cf. Ref. [145], e.g.), must evolve into a fixed point for $\mu \to \infty$ in geometrical terms. Reviews of this Asymptotic-Safety (AS) Scenario can be found in Ref. [145, 146].

Along a realistic RG trajectory to high energy scales, other operators and couplings in addition to those of the Einstein-Hilbert action S_{EH} (2.19) may become relevant to $\Gamma_{(\mu)}$. Yet, the general features of AS are visible already in the EH truncation, where $\Gamma_{(\mu)} = S_{\mathrm{EH}(\mu)}$ at all scales. In this case, with zero cosmological constant, the theory's RG evolution implies a running of the system's sole coupling, Newton's coupling $G(\mu)$. The coupling is related to its measured low-energy value $G_{\mathrm{N}}^{(d)}$, Newton's constant in d dimensions, as per

$$G(\mu) = Z^{-1}(\mu) G_{\mathrm{N}}^{(d)}, \tag{9.1}$$

where $Z^{-1}(\mu)$ is the graviton wave-function renormalization factor, with $Z^{-1}(\mu) \to 1$ for $\mu \to 0$.

As we want to discuss the coupling's behavior in the scale-invariant regime, it is appropriate to define a dimensionless coupling g:

$$g(\mu) := \mu^{d-2} G(\mu) = \mu^{d-2} Z^{-1}(\mu) G_{\mathrm{N}}^{(d)}. \tag{9.2}$$

The theory arrives at a fixed point once g becomes stationary along the RG trajectory, i.e., if its beta function

$$\beta(\mu) = \frac{d\,g(\mu)}{d\ln(\mu/\mu_0)} \tag{9.3}$$

is zero at a certain $\mu^\star$. With the graviton's anomalous dimension $\eta(\mu) = -\frac{d\ln Z}{d\ln(\mu/\mu_0)}$, the renomalization-group equation (RGE) for g reads

$$\beta(\mu) = \big[d - 2 + \eta(\mu)\big]g. \tag{9.4}$$

With $g^\star = g(\mu^\star)$, $\eta^\star = \eta(\mu^\star)$, the fixed-point condition thus is

$$0 = \beta(\mu^\star) = (d - 2 + \eta^\star)g^\star. \tag{9.5}$$

This equation apparently has two solutions: One is a non-interacting (Gaussian) fixed point with $g^\star = g_{\mathrm{G}} = 0$, analogous to the asymptotically free coupling of QCD. Yet in addition, also an interacting (non-Gaussian) fixed point may exist with

$$g^\star = g_{\mathrm{NG}} \neq 0 \quad \text{if} \quad \eta^\star = -d + 2. \tag{9.6}$$

In Ref. [147] it has been shown by the means of the exact RGE (ERGE) [148] with an optimized regulator R_k [149] that such a non-Gaussian fixed point indeed is approached in the Euclidean EH truncation for $\mu \to \infty$. The coupling's non-Gaussian critical exponent $\Theta_{\mathrm{NG}} = -\left.\frac{\partial\beta}{\partial g}\right|_{g_{\mathrm{NG}}}$ is positive for $d > 2$, and so the fixed point is UV attractive: $g - g_{\mathrm{NG}} \sim 1/\mu^{\Theta_{\mathrm{NG}}} \to 0$ for $\mu \to \infty$.

Explicitly, $\eta(g)$ and the coupling at the non-Gaussian fixed point $\bar{g}_{\mathrm{NG}}$ are for a rescaled $\bar{g} = g/c_d$ [147]

$$\eta(\bar{g}) = \frac{2(d-2)(d+2)\bar{g}}{2(d-2)\bar{g} - 1}, \qquad \bar{g}_{\mathrm{NG}} = \frac{1}{4d}, \tag{9.7}$$

with $c_d = \Gamma(d/2+2)(4\pi)^{d/2-1}$. Note that this expression for $\eta(\bar{g})$ cannot be calculated perturbatively in a polynomial expansion in the infrared (IR) limit $\bar{g} \approx 0$.

The critical exponents associated with this solution are [147]

$$\Theta_{\mathrm{G}} = 2 - d, \qquad \Theta_{\mathrm{NG}} = 2d\frac{d-2}{d+2}. \tag{9.8}$$

This Θ_{G} implies the appropriate IR scaling for $G(\mu)$ to acquire a nonzero low-energy value $G(\mu) = \mu^{d-2}g(\mu) \to G_{\mathrm{N}}^{(d)}$ for $\mu \to 0$.

Figure 9.1 illustrates the transition between the Gaussian fixed point in the IR regime to the non-Gaussian fixed point in the UV regime for four dimensions exemplary. As can be seen in the figure, the cross-over between the two scaling regimes takes place mainly in a compact region around a transition scale Λ_T, which we identified with $\mathrm{M_{PL}}$ in the figure. As conjectured, $g(\mu)$ stays finite even at scales beyond the Planck scale, and $G(\mu) = g(\mu)/\mu^2$ approaches zero.

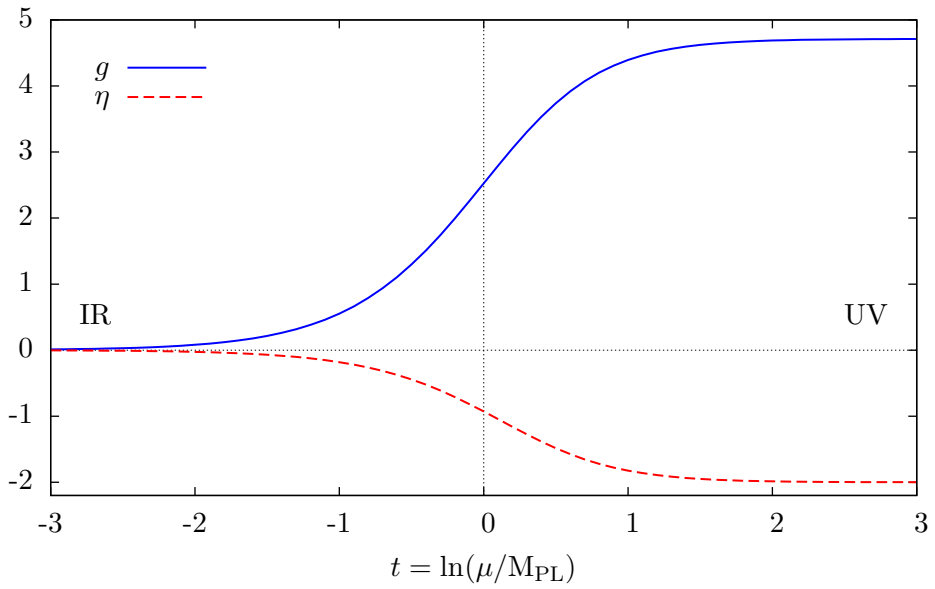

Figure 9.1: Scaling g and η in four Euclidean dimensions in the EH truncation without a cosmological constant. Figure as in Ref. [147].

The EH truncation with its running Newtonian coupling (and optionally a running cosmological constant Λ) features a promising UV behavior, but it is a priori unclear whether the truncation captures all relevant effects of quantum Einstein Gravity; in general the number of relevant operators and corresponding couplings is unknown. Studies of truncations allowing a larger set of operators in $\Gamma_{(\mu)}$ next to R and the volume element, such as the $f(R)$ truncation [150], found a similar fixed-point scaling in these models. Also fixed points have been found in models including matter fields (Gaussian fixed points for the matter couplings) [151].

While there is no proof for the existence of a fixed point in the untruncated case, we are encouraged by this support to look for LHC signatures of AS in the ADD model, such as the onset of the transition region.

9.2 Approximate renormalization-group running

The RGE (9.4) can be integrated analytically for the anomalous dimension in (9.7) to give an implicit function of g and μ, see Ref. [147]. However, the functional form of $\eta(g)$ in (9.7) is specific to the EH truncation, while the effect of a transition between a Gaussian IR and a non-Gaussian UV fixed-point regime is immanent to a larger set of effective average actions, as mentioned above.

For the calculation of amplitudes in RG-improved perturbation theory, it is worthwhile to construct effective, approximating functions $G(\mu)$ and $Z(\mu)$ explicitly depending on the renormalization scale μ. The transition between both fixed point regimes can be parametrized by the means of an effective transition scale Λ_T, analogous to the strong

scale Λ_{QCD}. Dependent on the effective average action and the approximation of Z^{-1} under consideration, Λ_T can be considered to be of the order of the fundamental Planck scale. Ultimately it has to be matched to the parameters of an underlying model or extracted from experimental data.

We use the following approximations introduced in Ref. [138]:

Quenched approximation

$$Z^{-1}_{(0)}(\mu;\Lambda_T) = \begin{cases} 1 & \text{if } \mu < \Lambda_T \\ \left(\frac{\Lambda_T}{\mu}\right)^{d-2} & \text{if } \mu \geq \Lambda_T \end{cases} \tag{9.9}$$

The anomalous dimension leading to this Z^{-1} is $\eta = (2-d)\Theta(\mu - \Lambda_T)$. In this approximation, the transition between Gaussian IR scaling and non-Gaussian UV scaling is approximated to happen instantly at a transition scale Λ_T.

Linear approximation

$$Z^{-1}_{(1)}(\mu;\Lambda_T) = \left[1 + \left(\frac{\mu}{\Lambda_T}\right)^{d-2}\right]^{-1} \tag{9.10}$$

Quadratic approximation

$$Z^{-1}_{(2)}(\mu;\Lambda_T) = \sqrt{1 + \left[\frac{1}{2}\left(\frac{\mu}{\Lambda_T}\right)^{d-2}\right]^2} - \frac{1}{2}\left(\frac{\mu}{\Lambda_T}\right)^{d-2} \tag{9.11}$$

The expressions for the linear and the quadratic approximation are solutions of (9.4) with (9.7) using the approximations $\Theta_{\mathrm{NG}}/\Theta_{\mathrm{G}} = -1$ and $\Theta_{\mathrm{NG}}/\Theta_{\mathrm{G}} = -2$, respectively (with additional small approximations irrelevant here). The ratio $\Theta_{\mathrm{NG}}/\Theta_{\mathrm{G}} = -2d/(d+2)$ measures the swiftness of the transition between the two scaling regimes and lies in the domain $(-4/3, -2)$ for any $d > 2$. The linear and quadratic approximations therefore constitute bounding cases for the exact cross-over behavior in the EH truncation.

The transition scales in $Z^{-1}_{(0)}$, $Z^{-1}_{(1)}$, and $Z^{-1}_{(2)}$ are specific to the individual approximations. For the comparison of observables calculated in different approximations, a suitable matching condition has to be defined. Such a matching is exemplarily provided in the UV limit $Z^{-1}(\mu) \approx \left(\frac{\Lambda_T}{\mu}\right)^{d-2}$, common to all three approximations. It allows to match the transition scales to a non-Gaussian fixed point and the IR value of the d-dimensional variant of either Newton's constant or the Planck mass through (2.25) and (9.2):

$$g_{\mathrm{NG}} = \Lambda_T^{d-2} G_{\mathrm{N}}^{(d)} = \frac{(2\pi)^{d-4}}{8\pi}\left(\frac{\Lambda_T}{\mathrm{M}_\star}\right)^{d-2}. \tag{9.12}$$

For illustration, Z^{-1} as well as the corresponding η are shown in the three approximation for a common transition scale Λ_T in Figure 9.2. Note how η converges to its asymptotic values at different paces in the linear and quadratic approximations. Also the transition is faster the larger d is in the linear and quadratic approximations: The larger d is, the earlier the fixed-point scaling ratio $(\mu/\Lambda_T)^{d-2}$ dominates the constant terms in (9.10) and (9.11).

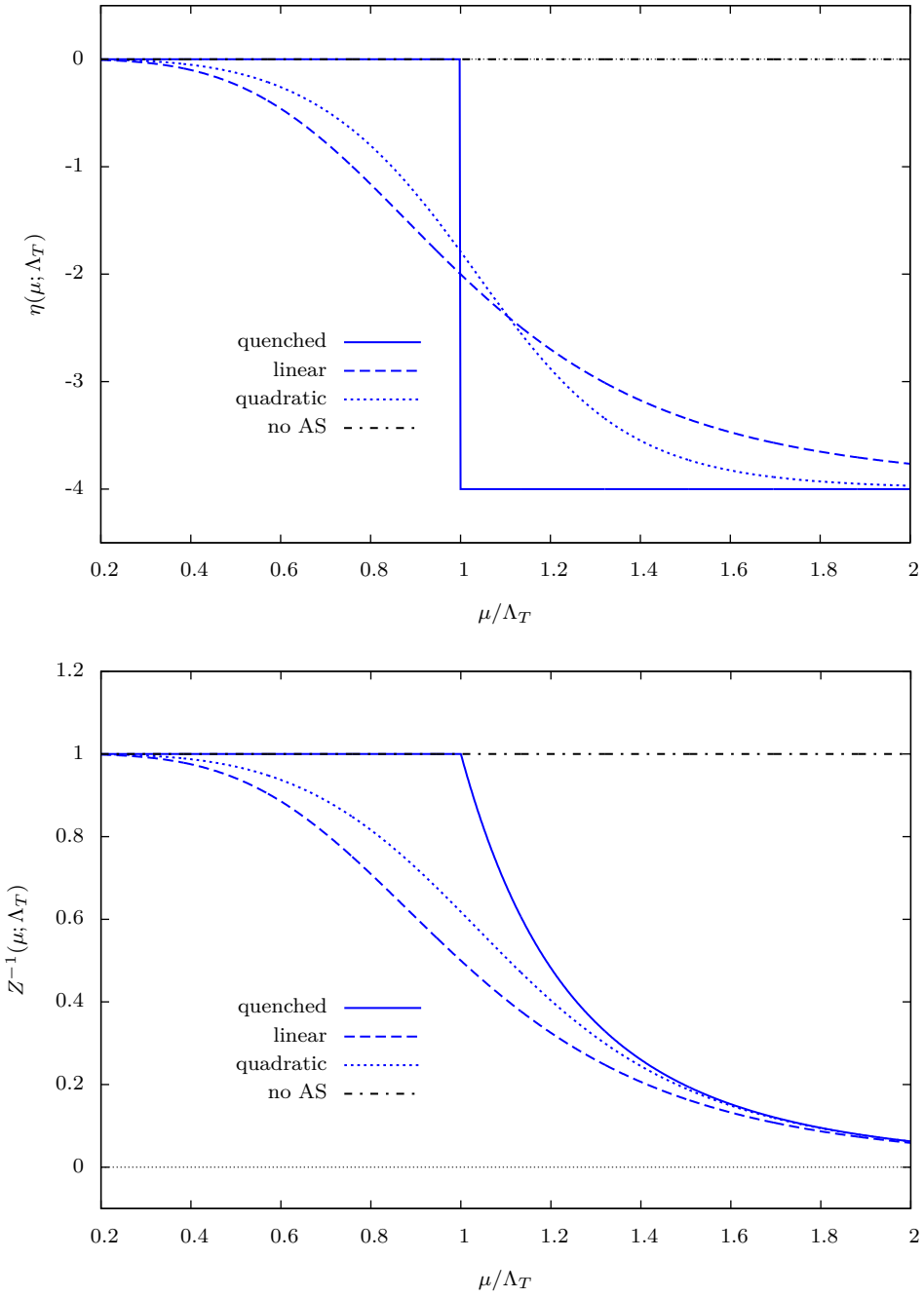

Figure 9.2: Anomalous dimension η (top panel) and graviton wave function normalization factor Z^{-1} (bottom panel) in the vicinity of the cross over scale Λ_T in the quenched, linear, and quadratic approximations for $d = 6$ dimensions.

10 Virtual gravitons in the s-channel

We will now discuss how the AS hypothesis can lead to meaningful scattering amplitudes, even if the involved energies approach or surpass the fundamental Planck scale. We focus on tree-level graviton exchange in the s-channel, as the s-channel is generically enhanced over t and u channels owing to its pole at $s = m^2$.

The Feynman graphs describing such a scattering at leading order in G_{N} are depicted in Figure 10.1, for $pp \to \ell^+\ell^-$ scattering exemplarily. Refer to Ref. [54, 143] for Feynman rules. The amplitude $\mathcal{A}$ can conveniently be decomposed as $\mathcal{A} = \mathcal{S}\mathcal{T}$, following the notation of Ref. [54]. $\mathcal{S}$ denotes the denominator of the graviton s-channel propagator summed over all KK modes,

$$\mathcal{S}(\hat{s}) = \frac{S_{n-1}}{\mathrm{M}_\star^{n+2}} \int_0^\infty dm \, \frac{m^{(n-1)}}{\hat{s} - m^2 + \mathrm{i}\epsilon}, \tag{10.1}$$

and $\mathcal{T} = T^{\mu\nu}T_{\mu\nu} - \frac{1}{n+2}T^\mu_\mu T^\nu_\nu$ comprises all tensor structure and external momenta. T^μ_μ is zero in the limit of massless external states, see Ref. [54], e.g. While $\mathcal{T}$ yields a well-behaved function of the external momenta upon squaring and spin-averaging, the KK sum in (10.1) is divergent for $n \geq 2$.

The effective average action is hypothesized to be free of UV divergences in the AS Scenario. Consequently the amplitude, calculated in RG-improved perturbation theory, should be finite too. The renormalization scale μ has to be of the order of the typical energies involved in the problem, $\sqrt{\hat{s}}$ and m in this case. Following the assumption of Ref. [138] that vertex corrections are negligible, the scale dependence of $\mathcal{A}$ enters through the renormalization factor of the [$(n+2)$-dimensional] graviton wave function $Z^{-1}(\mu, \Lambda_T)$ dressing the graviton propagator. Therefore, the RG-improved KK sum $\mathcal{S}$ is

$$\mathcal{S}(\hat{s}) = \frac{S_{n-1}}{\mathrm{M}_\star^{n+2}} \int_0^\infty dm \, Z^{-1}(\mu(\hat{s}, m), \Lambda_T) \frac{m^{(n-1)}}{\hat{s} - m^2 + \mathrm{i}\epsilon}. \tag{10.2}$$

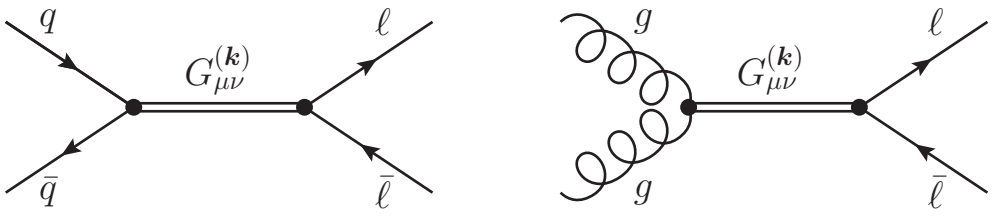

Figure 10.1: Tree-level Feynman graphs for the $\ell\bar{\ell}$ production at hadron colliders through the exchange of virtual KK graviton modes.

10.1 Renormalization-scale choices

The Drell-Yan amplitude has been studied in the AS scenario for the scale choices $\mu = \sqrt{\hat{s}}$, $\mu = m$, $\mu^2 = |\hat{s} - m^2|$, and $\mu^2 = \hat{s} + m^2$ in the literature [138, 152]:

- $\mu = \sqrt{\hat{s}}$ is a frequent renormalization-scale choice for s-channel dominated processes. Yet, with this μ, the Z^{-1} does not regularize the KK integral as it does not take account of those KK modes constituting the part of the $(4+n)$-dimensional graviton with high extra-dimensional momentum. $Z^{-1}(\hat{s}, \Lambda_T)$ can plainly be pulled out of the integral in (10.2). To obtain a finite amplitude, the integral must be regularized by other means, see Ref. [152].

- $\mu = m$ is motivated in the limit $\hat{s} \ll \Lambda_T^2$, where large momenta of the $(4+n)$-dimensional graviton stem from large values of m. At a hadron collider where the parton luminosities generically decrease steeply with $\sqrt{\hat{s}}$ approaching the collider's total center-of-mass energy $\sqrt{s}$ and where therefore the small-$\hat{s}$ region of the cross section is enhanced, this is a sound approximation for large Λ_T.

- Choosing $\mu^2 = |\hat{s} - m^2|$, the renormalization scale is identified with the propagator denominator. With this choice, the propagator's pole region is emphasized, as Z^{-1} is in the Gaussian regime if $\hat{s} \sim m^2$, even for $\hat{s} \gg \Lambda_T^2$ and $m \gg \Lambda_T$. For large $\hat{s}$, the KK sum in (10.2) has been found to scale $\propto \hat{s}$ for large $\hat{s}$ [138].

- With $\mu^2 = \hat{s} + m^2$, the renormalization scale corresponds to the momentum of the associated $(n+4)$-dimensional graviton.

We require two properties of the renormalization-scale identification: Firstly $\mathcal{S}(\hat{s})$, the KK sum in (10.2), should be regularized by $Z^{-1}(\mu)$. Secondly, since we postulate asymptotic safety, the KK sum must not spoil the unitarity of the scattering matrix in its large-$\hat{s}$ limit. To be consistent with the unitarity condition in $hh \to hh$ scattering, this implies, that $\mathcal{S}(\hat{s})$ have to scale $\propto 1/\hat{s}^2$ in for large $\hat{s}$, so that the s-channel S-wave–partial-wave amplitude for $hh \to hh$ [153, 154]

$$a_{0,s} \propto \hat{s}^2 \mathcal{S}(\hat{s}) \tag{10.3}$$

is finite for large $\hat{s}$. Note that the unitarity condition also puts limits the ratio $\Lambda_T/\mathrm{M}_\star$ which must not exceed 10–2 approximately, dependent on the number of extra dimensions and the Z^{-1} choice [153]. The ratio dictated by (9.12) in the EH truncation is in agreement with this limit, but it almost saturates the allowed range (more so for increasing n).

Of the four scale options, two have the two required properties: $\mu = m$ in the zero-$\hat{s}$ approximation and $\mu^2 = \hat{s} + m^2$ also for nonzero $\hat{s}$. In the following, we introduce our notation in a short discussion of $\mu = m$ and discuss $\mu^2 = \hat{s} + m^2$ at more length thereafter.

10.2 KK sum with $\mu^2 = m^2$

Defining the dimensionless variables $x^2 = m^2/\Lambda_T^2$ and $y^2 = \hat{s}/\Lambda_T^2$, the dimensionful scales $\mathrm{M}_\star$ and Λ_T can be removed from the KK integral:

$$\mathcal{S}(\hat{s}) = -\frac{S_{n-1}}{\mathrm{M}_\star^4}\left(\frac{\Lambda_T}{\mathrm{M}_\star}\right)^{n-2} C(\hat{s}/\Lambda_T^2) \tag{10.4}$$

with

$$C(y^2) = \int_0^\infty dx\, Z^{-1}(x,y)\frac{x^{(n-1)}}{x^2 - y^2 - \mathrm{i}\epsilon}. \tag{10.5}$$

For very small y^2, this integral can be approximated by its value at $y = 0$, $C(y^2) \approx C(0) = c_0$. In the three approximations for Z^{-1} introduced in Section 9.2, the c_0 are [138]

$$c_0^{(0)} = \int_0^1 dx\, x^{(n-3)} + \int_1^\infty dx\, x^{-5} = \frac{1}{n-2} + \frac{1}{4} \tag{10.6a}$$

$$c_0^{(1)} = \frac{1}{4}\Gamma\left(\frac{n-2}{n+2}\right)\Gamma\left(\frac{n+6}{n+2}\right) \tag{10.6b}$$

$$c_0^{(2)} = -\frac{\Gamma(1+2/(n+2))\Gamma\left(-4/(n+2)\right)}{(n+2)\Gamma\left(2-2/(n+2)\right)}, \tag{10.6c}$$

where the superscripts (0), (1), and (2) label expressions in the quenched, linear, and quadratic approximation, respectively.

With $C(y^2)$ approximated by c_0, the KK sum can be parametrized by the means of a single effective scale Λ_{eff}, reproducing the form of lowest-order effective theory [54, 143, 155] (see Ref. [156] for a review):

$$\mathcal{S}_{\mathrm{eff}} = -\frac{4\pi}{\Lambda_{\mathrm{eff}}^4}. \tag{10.7}$$

We refer to (10.7) as the Giudice-Rattazzi-Wells (GRW) parametrization in the following.

Transition scale matching

Apparently, the values of c_0 differ in the three approximations. For comparisons of the KK sums at $\hat{s} \ll \Lambda_T^2$, it is convenient to perform a matching of Λ_T in (10.4) at zero $\hat{s}$ so that

$$\mathcal{S}^{(0)}(\hat{s}=0) = \mathcal{S}^{(1)}(\hat{s}=0) = \mathcal{S}^{(2)}(\hat{s}=0). \tag{10.8}$$

Taking $\Lambda_T^{(0)}$ as the reference scale, the other scales $\Lambda_T^{(i)}$ $(i = 1, 2)$ are [138]

$$\Lambda_T^{(i)} = \left(\frac{c_0^{(0)}}{c_0^{(i)}}\right)^{1/(n-2)} \Lambda_T^{(0)} \tag{10.9}$$

Since the transition scales are associated with the non-Gaussian fixed-point coupling, the matching implies that different fixed points are acquired in the different approximation schemes as per (9.12).

Large-$\hat{s}$ behavior for $\mu = m$

The KK sum also is finite for $\hat{s} > 0$ with $\mu = m$. (Expressions for $C(y^2)$ in the quenched approximation can be found in Appendix C.) However, at large $\hat{s}$, $\mathcal{S}(\hat{s})$ falls off as $1/\hat{s}$. This is to slow to be compatible with the Higgs unitary bound. This is expected, since for large $\hat{s} > \Lambda_T^2$, the $(n+4)$-dimensional graviton associated with the KK tower should be treated in its UV limit. However, with $\mu = m$, the KK sum is in its IR domain if m^2 is small, irrespective $\hat{s}$.

10.3 KK sum with $\mu^2 = \hat{s} + m^2$—quenched approximation

With $\hat{s}$ at the order of Λ_T, the momentum of the $(4+n)$-dimensional graviton on the SM brane cannot be neglected in the renormalization-scale choice. Adapted to the dimensionless variables $x^2 = m^2/\Lambda_T^2$ and $y^2 = \hat{s}/\Lambda_T^2$, the approximated graviton wave function renormalization factors defined in section 9.2 read with $\mu = \Lambda_T\sqrt{x^2+y^2}$

$$Z_{(0)}^{-1}(x,y) = \begin{cases} 1 & \text{if } x^2 < 1 - y^2 \\ (x^2+y^2)^{-\frac{n+2}{2}} & \text{if } x^2 \geq 1 - y^2 \end{cases} \tag{10.10a}$$

$$Z_{(1)}^{-1}(x,y) = \left[1 + (x^2+y^2)^{\frac{n+2}{2}}\right]^{-1} \tag{10.10b}$$

$$Z_{(2)}^{-1}(x,y) = \sqrt{1 + \frac{1}{4}(x^2+y^2)^{n+2}} - \frac{1}{2}(x^2+y^2)^{\frac{n+2}{2}}. \tag{10.10c}$$

10.3.1 $\hat{s} + m^2$ propagator

Since $\sqrt{\hat{s}+m^2}$ is the momentum of a massless $(4+n)$-dimensional graviton, the KK sum in (10.1) has also been analyzed with the propagator proportional to the squared inverse of this momentum in the literature [138]. From a 4-dimensional perspective, this identification corresponds to replacing the Minkowskian propagator by an Euclidean one in the sum, leading to

$$C(y^2) = \int_0^\infty dx\, Z^{-1}(x,y)\frac{x^{(n-1)}}{x^2+y^2}. \tag{10.11}$$

(Note that this expression also corresponds to the KK sum over Minkowskian t- and u-channel propagators, with $\mu^2 = |\hat{t}| + m^2$ and $\mu^2 = |\hat{u}| + m^2$ respectively.)

The y^2-dependence of the KK sum in (10.11) in the quenched approximation is published on a numeric level in Ref. [138] for even n. We state the analytical expressions below. In the quenched approximation, the KK integral can conveniently be decomposed

as

$$C(y^2) = \int_0^{\sqrt{1-y^2}} dx\, \frac{x^{(n-1)}}{x^2+y^2} \quad + \int_{\sqrt{1-y^2}}^{\infty} dx\, \frac{x^{(n-1)}}{(x^2+y^2)^{\frac{n+4}{2}}} \tag{10.12a}$$

$$= C_{\mathrm{IR}}(y^2) + C_{\mathrm{UV}}(y^2), \tag{10.12b}$$

where

$$C_{\mathrm{IR}}(y^2) = \begin{cases} (-1)^{\frac{n}{2}} y^{n-3} \left[y \ln y + y f_{\mathrm{IR}}^{(n)}(y^2) \right] & \text{if } y^2 < 1,\ n \text{ even} \\ (-1)^{\frac{n-1}{2}} y^{n-3} \left(y \tan^{-1}\left(\frac{\sqrt{1-y^2}}{y} \right) + \sqrt{1-y^2}\, g_{\mathrm{IR}}^{(n)}(y^2) \right) & \text{if } y^2 < 1,\ n \text{ odd} \\ 0 & \text{if } y^2 \geq 1 \end{cases} \tag{10.13}$$

with the rational functions

$$f_{\mathrm{IR}}^{(n)}(y^2) = \sum_{\ell=1}^{\frac{n-2}{2}} \frac{(-1)^{\ell+1}}{2\ell} \left(\frac{1-y^2}{y^2} \right)^{\ell}, \tag{10.14a}$$

$$g_{\mathrm{IR}}^{(n)}(y^2) = \sum_{\ell=0}^{\frac{n-3}{2}} \frac{(-1)^{\ell+1}}{2\ell+1} \left(\frac{1-y^2}{y^2} \right)^{\ell} \tag{10.14b}$$

and

$$C_{\mathrm{UV}}(y^2) = \begin{cases} \frac{1}{n(n+2)y^4} \left(2 - (2+ny^2)(1-y^2)^{\frac{n}{2}} \right) & \text{if } y^2 < 1 \\ \frac{2}{n(n+2)y^4} & \text{if } y^2 \geq 1. \end{cases} \tag{10.15}$$

These results are consistent with those of Ref. [138], see Figure 10.2.

10.3.2 $\hat{s} - m^2 + \mathrm{i}\epsilon$ propagator

For the Minkowskian propagator in (10.5), $C(y^2)$ reads

$$C(y^2) = \int_0^{\sqrt{1-y^2}} dx\, \frac{x^{(n-1)}}{x^2-y^2-\mathrm{i}\epsilon} \quad + \int_{\sqrt{1-y^2}}^{\infty} dx\, \frac{x^{(n-1)}}{(x^2+y^2)^{\frac{n+2}{2}}(x^2-y^2-\mathrm{i}\epsilon)} \tag{10.16a}$$

$$= C_{\mathrm{IR}}(y^2) + C_{\mathrm{UV}}(y^2), \tag{10.16b}$$

where

$$\mathrm{Im}\, C(y^2) = \frac{\pi}{2} y^{n-2} Z_{(0)}^{-1}(x=y, y) = \begin{cases} \frac{\pi}{2} y^{n-2} & y^2 < \frac{1}{2} \\ \frac{\pi}{4\sqrt{2}^n} \frac{1}{y^4} & y^2 \geq \frac{1}{2} \end{cases} \tag{10.17}$$

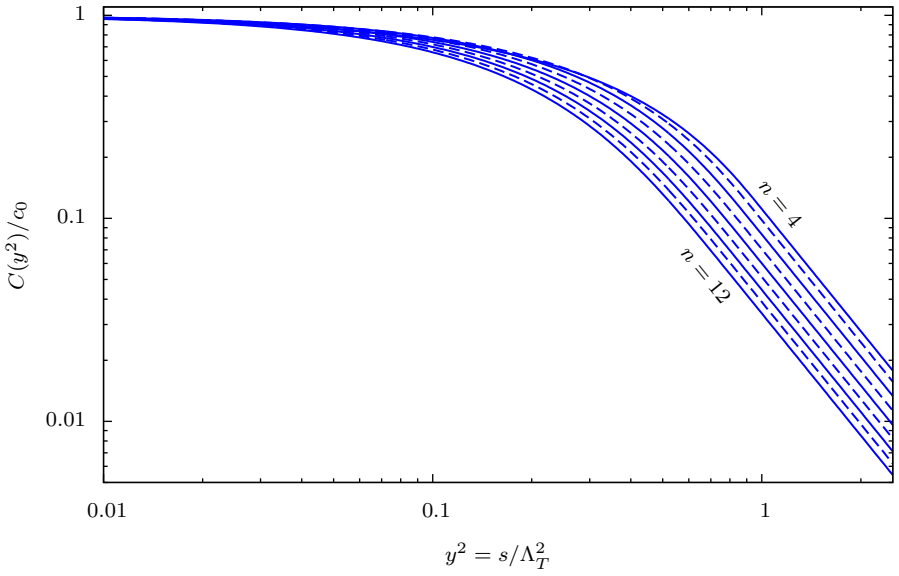

Figure 10.2: s dependence of the KK sum in quenched approximation with analytically continued propagator for $4 \leq n \leq 12$. Solid lines: even n; dashed lines: odd n. The normalized amplitudes decrease strictly with growing $n > 4$ for large $y^2 \gtrsim 1$. The figure reproduces the results of Ref. [138].

$$\mathrm{Re}\, C_{\mathrm{IR}}(y^2) = \begin{cases} y^{n-3}\left(y \ln\left(\frac{\sqrt{|1-2y^2|}}{y}\right) + y F_{\mathrm{IR}}(y^2)\right) & \text{if } y^2 < 1,\ n \text{ even} \\ y^{n-3}\left(-y \coth^{-1}\left(\frac{\sqrt{1-y^2}}{y}\right) + \sqrt{1-y^2} G_{\mathrm{IR}}(y^2)\right) & \text{if } y^2 < \frac{1}{2},\ n \text{ odd} \\ y^{n-3}\left(-y \tanh^{-1}\left(\frac{\sqrt{1-y^2}}{y}\right) + \sqrt{1-y^2} G_{\mathrm{IR}}(y^2)\right) & \text{if } \frac{1}{2} \leq y^2 < 1,\ n \text{ odd} \\ 0 & \text{if } y^2 \geq 1 \end{cases} \tag{10.18}$$

$$\mathrm{Re}\, C_{\mathrm{UV}}(y^2) = \begin{cases} \frac{1}{2\sqrt{2^n} y^4}\left(-\ln\sqrt{|1-2y^2|} + F_{\mathrm{UV}}(y^2)\right) & \text{if } y^2 < 1,\ n \text{ even} \\ \frac{1}{2\sqrt{2^n} y^4} F_{\mathrm{UV}}(1) & \text{if } y^2 \geq 1,\ n \text{ even} \\ \frac{1}{2\sqrt{2^n} y^4}\left(\coth^{-1}\sqrt{2-2y^2} - \sinh^{-1}(1) + G_{\mathrm{UV}}(y^2)\right) & \text{if } y^2 < \frac{1}{2},\ n \text{ odd} \\ \frac{1}{2\sqrt{2^n} y^4}\left(\tanh^{-1}\sqrt{2-2y^2} - \sinh^{-1}(1) + G_{\mathrm{UV}}(y^2)\right) & \text{if } \frac{1}{2} \leq y^2 < 1,\ n \text{ odd} \\ \frac{1}{2\sqrt{2^n} y^4}\left(-\sinh^{-1}(1) + G_{\mathrm{UV}}(1)\right) & \text{if } y^2 \geq 1,\ n \text{ odd} \end{cases} \tag{10.19}$$

with

$$F_{\mathrm{IR}}(y^2) = \sum_{\ell=1}^{\frac{n-2}{2}} \frac{1}{2\ell} \left(\frac{1-y^2}{y^2}\right)^{\ell}, \qquad G_{\mathrm{IR}}(y^2) = \sum_{\ell=0}^{\frac{n-3}{2}} \frac{1}{2\ell+1} \left(\frac{1-y^2}{y^2}\right)^{\ell} \tag{10.20}$$

$$F_{\mathrm{UV}}(y^2) = -\frac{\sqrt{2}^n}{4} \sum_{k=0}^{\frac{n-2}{2}} \binom{\frac{n}{2}-1}{k} \left(\frac{-1}{2}\right)^k \sum_{\ell=1}^{k+1} \frac{(2y^2)^\ell}{\ell}, \quad G_{\mathrm{UV}}(y^2): \text{ See Table 10.1.} \tag{10.21}$$

n	$G_{\mathrm{UV}}(y^2)$
1	$\sqrt{2}\left(-1+\sqrt{1-y^2}\right)$
3	$-\frac{\sqrt{2}}{3}\left[-1+\sqrt{1-y^2}\left(1+2y^2\right)\right]$
5	$\frac{\sqrt{2}}{15}\left[13+\sqrt{1-y^2}\left(-13-14y^2+12y^4\right)\right]$
7	$-\frac{\sqrt{2}}{105}\left[-139+\sqrt{1-y^2}\left(139+122y^2-276y^4+120y^6\right)\right]$
9	$\frac{\sqrt{2}}{315}\left[577+\sqrt{1-y^2}\left(-577-446y^2+2028y^4-1880y^6+560y^8\right)\right]$
11	$-\frac{\sqrt{2}}{3465}\left[-8587+\sqrt{1-y^2}\left(8587+6026y^2-49188y^4+72200y^6-44240y^8+10080y^{10}\right)\right]$

Table 10.1: $G_{\mathrm{UV}}(y^2)$ as defined in (10.19) for an odd number of extra dimensions.

The results for C_{IR} in (10.13) and (10.18) coincide with those published in Ref. [143], with modified limits of the integral. The expressions in (10.18) and (10.19) diverge individually for $y^2 \to 1/2$ since for $y^2 = 1/2$, the propagator's pole is at the transition point between the IR and UV regimes. At $y^2 = 1/2$, the pole region is split in between C_{IR} and C_{UV} whose sum is finite.

In Figure 10.3, $|C(y^2)|$ is shown for both propagator prescriptions for several values of n, normalized to c_0. In the large-y^2 limit, both sets of curves show the $1/s^2$ scaling in accordance with the unitarity condition. The curves deviate substantially from those in the zero-$\hat{s}$ approximation [$C(y^2)/c_0 = 1$] already for center of mass energies significantly below Λ_T, see also Ref. [138]. For the values of n shown, $C(y^2) \approx c_0$ is an apt approximation for the Minkowskian propagator if $y^2 < 1/2$; though, as discussed more detailed in the next section, this is unique to the quenched approximation just as the kinks at $y^2 = 1/2$. The kinks dominantly stem from $\mathrm{Im}\, C(y^2)$ in (10.17) and indicate the transition of the propagator's pole between the two fixed-point regimes. As the instant transition is unique to the quenched approximation and as $C(y^2)$ dominates the $m_{\ell\ell}$ distribution in dilepton events, the kinks indicate that collider predictions may have a sizable approximation-scheme dependence for a Minkowskian propagator.

Note that in the large-$\hat{s}$ limit, the dimensionful KK sum is proportional to the non-Gaussian fixed-point coupling g_{NG}:

$$\mathcal{S}(\hat{s})\big|_{\hat{s}>\Lambda_T^2} = S_{n-1} \left(\frac{\Lambda_T}{\mathrm{M}_\star}\right)^{n+2} \frac{A}{\hat{s}^2} = \frac{A}{16\,\Gamma(n/2)} \left(\frac{2}{\sqrt{\pi}}\right)^{n+2} \frac{g_{\mathrm{NG}}}{\hat{s}^2}, \tag{10.22}$$

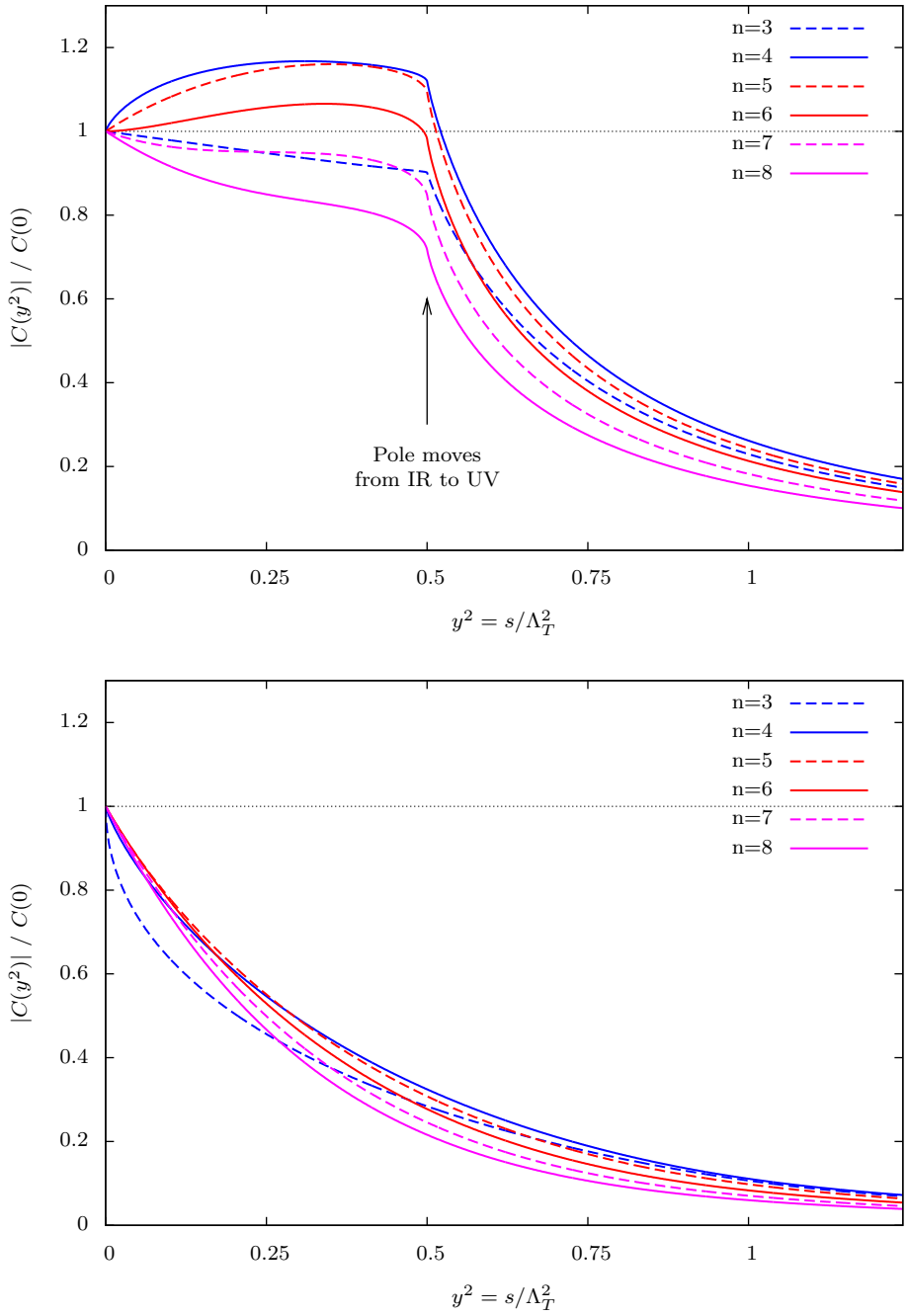

Figure 10.3: The absolute value of the dimensionless KK-summed s-channel propagator denominator for a Minkowskian (top panel) and a Euclidean (bottom panel) signature in dependence of the center of mass energy.

where A is the coefficient of $1/y^{-4}$ in the large-y regime of $C(y^2)$ [see (10.15), (10.17), and (10.19)].

10.4 Approximation-scheme dependence

To assess the approximation-scheme dependence of $C(y^2)$, the integrals in (10.11) and (10.16b) have been solved semi-numerically also in the linear and quadratic approximations (see Appendix C for details). The resulting $|C(y^2)|$ together with those in the quenched approximation are shown in Figure 10.4 for $n = 3$ and 6. The scheme-dependent transition scales are matched to $\Lambda_T^{(0)}$ according to (10.9).

As already discussed in Ref. [138], the scheme dependence is weak in the Euclidean case. The discrepancies in the large-$\hat{s}$ tail are driven by the ratio of the scales $\Lambda_T^{(i)}$—fixed in the low-energy matching—as

$$C^{(i)}(y^2) \overset{y\gg 1}{\approx} \frac{2}{n(n+2)y^4} \propto \frac{\left(\Lambda_T^{(i)}\right)^4}{\hat{s}^2} \tag{10.23}$$

in all three approximations. This large-$\hat{s}$ limit familiar for the quenched approximation holds for all three approximations, as for the renormalization scale choice employed, a large $\hat{s} \gtrsim \mathcal{O}(\text{few}\Lambda_T)$ guarantees that all $Z_{(i)}^{-1}$ are in the Gaussian fixed-point regime, i.e. equal $Z_{(0)}^{-1}|_{y>1}$ irrespective of the value of x.

For the Minkowskian propagator, the approximation-scheme dependence is more pronounced. This is expected since the largest contribution to the integral here comes from the pole region; i.e., the integral is qualitatively dominated by $Z^{-1}(x \approx y, y)$. For the scale choice employed, $\mu = \sqrt{x^2+y^2}\Lambda_T$, this implies that $|C(y^2 \approx 1/2)|$ is sensitive to the cross-over behavior of Z^{-1}. However, the cross-over region is the region where the approximated Z^{-1} differ, while the asymptotic behavior is fixed by the fixed-point conditions—see Figure 9.2. The link between $C(y^2)$ and $Z^{-1}(x \approx y, y)$ is directly accessible quantitatively for $\operatorname{Im} C(y^2)$, which dominates $|C(y^2)|$ for small n beyond a certain energy threshold, at $y^2 \gtrsim 1/4$ for $n = 3$ for example. $\operatorname{Im} C(y^2)$ is given in terms of $Z^{-1}(\mu)$ through the first relation in (10.17), which also holds in the linear and quenched approximations for $Z_{(1)}^{-1}$ and $Z_{(2)}^{-1}$, respectively[1]. The sensitivity of $\operatorname{Re} C(y^2)$ to the details of $Z^{-1}(x \approx y, y)$ can be understood qualitatively: In the vicinity of the pole, the contributions to the integral from both sides of the pole become arbitrarily large individually. They are opposite-signed and add up to a very small total integral—compared to the individual contributions. Due to the necessary large cancellation, small differences between the approximated Z^{-1}s can result in comparably large differences in the $\operatorname{Re} C(y^2)$s.

Phenomenological implications of this approximation-scheme dependence are discussed in the next chapter.

[1] The imaginary part of the propagator denominator is a δ-family for $\epsilon \to 0$; thus, the integration is trivial for $\operatorname{Im} C(y^2)$ [138].

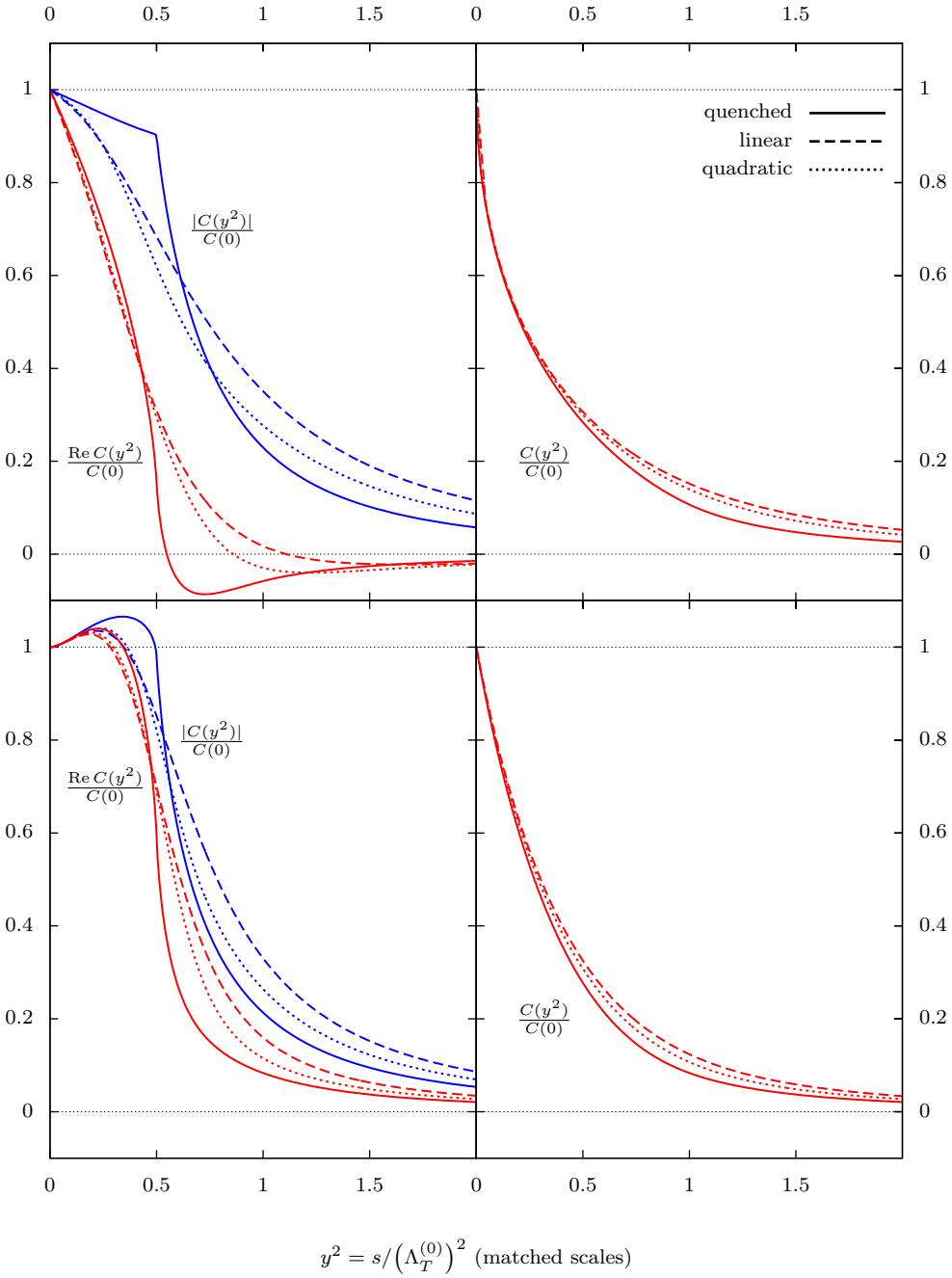

Figure 10.4: Normalized KK sum in the three approximations. Top: $n = 3$; bottom: $n = 6$; left: Minkowskian propagator; right: Euclidean propagator.

11 Drell-Yan leptons at the LHC

In the following chapter, we discuss how asymptotically safe graviton-exchange affects the phenomenology of dilepton events at the LHC ($pp \to \ell\bar{\ell}$). With gravitons coupling uniformly [$\propto G(\mu)$] to matter, the dilepton channel benefits from its lack of a QCD amplitude and from the detectors' excellent lepton-identification capabilities. The dilepton-channel and its experimental reach for gravity effects has been discussed in Ref. [54, 143, 155, 157, 158] in the effective-theory approach. Virtual-graviton contributions to other pair-production processes also are discussed in the literature: $pp \to \gamma\gamma/W^+W^-$ [159], $pp \to t\bar{t}$ [160], $pp \to$ dijet [161], and $pp \to hh$ [162]. Implications of AS on the LHC phenomenology of the Drell-Yan process also have been discussed in Ref. [138].

We discuss dilepton production using an implementation of the AS process in the multipurpose Monte-Carlo generator PYTHIA 8 [111, 162], developed in the course of this work. In Section 11.1, we review the relevant parton-level cross section formulae. In Section 11.2, we compare our predictions with results available in the literature [138, 163]. Afterwards, we reexamine the approximation-scheme dependence already discussed in the last chapter. Finally, we extract bounds on the model parameters from results of the LHC's 8-TeV run [164].

11.1 Parton-level cross sections

In tree-level $q\bar{q} \to \ell\bar{\ell}$ scattering, the graviton-induced amplitude $\mathcal{A} = \mathcal{S}\,\mathcal{T}$ interferes with the EW SM amplitude, given by s-channel photon and Z-boson exchange. The resulting cross section therefore consists of a pure SM term, a pure gravitational term, and an interference term. Differential in Mandelstam $\hat{t}$, the spin-averaged cross section is [54, 157]

$$\begin{aligned}\frac{d\sigma}{d\hat{t}}(q\bar{q} \to \ell\bar{\ell}) = \frac{d\sigma}{d\hat{t}}(q\bar{q} \to \ell\bar{\ell})_{\mathrm{SM}} &+ \frac{N_\ell \hat{s}^2}{512\pi}|\mathcal{S}(\hat{s})|^2 G_4(\hat{t}/\hat{s}) \\ &+ \frac{N_\ell \alpha_{\mathrm{em}}}{8} Q_q Q_\ell G_5(\hat{t}/\hat{s})\,\mathrm{Re}\,\mathcal{S}(\hat{s}) \\ &+ \frac{N_\ell \alpha_{\mathrm{em}}}{8}\,\frac{v_q v_\ell G_5(\hat{t}/\hat{s}) + a_q a_\ell G_6(\hat{t}/\hat{s})}{4{\mathrm{s_W}}^2{\mathrm{c_W}}^2} \\ &\quad \cdot \left[\frac{\hat{s}(\hat{s}-m_Z^2)}{(\hat{s}-m_Z^2)^2 + m_Z^2\Gamma_Z^2}\,\mathrm{Re}\,\mathcal{S}(\hat{s}) - \frac{\hat{s}\,m_Z\Gamma_Z}{(\hat{s}-m_Z^2)^2 + m_Z^2\Gamma_Z^2}\,\mathrm{Im}\,\mathcal{S}(\hat{s})\right].\end{aligned} \tag{11.1}$$

The notation and the normalization of the charges follow the convention used in the PYTHIA-8 implementation of the effective-theory cross section [163] in the GRW parametrization (10.7): N_ℓ is the number of unresolved lepton species; Q_f the electric

charge of f with $Q_{e^-} = -1$; $a_f = T_f$ and $v_f = T_f - 2Q_f \mathrm{s_W}^2$, where $T_f \leq \frac{1}{2}$ is the weak isospin of f. Other SM parameters can be found in Table 1.2. The $G_i(x)$ are polynomials abbreviating the phase-space and $\mathcal{T}$ momentum structure. They are listed in Appendix A. $\mathcal{S}(s)$ is the KK-summed graviton-propagator denominator as discussed in the last chapter [cf. (10.2), (10.4), and (10.7)]. The SM cross section can be found Ref. [113], e.g.

As there is no tree-level $gg \to \ell\bar{\ell}$ amplitude in the SM, the corresponding cross section is solely given by graviton exchange [54, 157]:

$$\frac{d\sigma}{d\hat{t}}(gg \to \ell\bar{\ell}) = \frac{N_\ell \hat{s}^2}{256\pi} |\mathcal{S}(s)|^2 G_{12}(\hat{t}/\hat{s}). \tag{11.2}$$

11.2 LHC phenomenology

To yield observables for hadron colliders, the parton-level cross sections have to be convoluted with PDFs; see Appendix A for a short introduction to the topic. The convolution is done here by PYTHIA 8.

The implementation of the AS processes bases on the existing effective-theory implementation in the GRW parametrization [163], which has explicitly been checked to agree with Refs [54, 113]. Details on the AS implementation such as understood switches and parameters can be found in Appendix D. For a validation of the code, $\mathcal{S}_{\text{eff}}$ in the GRW parametrization has been reimplemented in the AS code. The resulting effective-theory cross sections, differential in dilepton invariant mass

$$m_{\ell\ell}^2 = (p_\ell^\mu + p_{\bar{\ell}}^\mu)^2, \tag{11.3}$$

have been found to agree to those of the official implementation in PYTHIA 8.170. For comparison, $d\sigma/dm_{\ell\ell}$ for a 14-TeV LHC is shown in Figure 11.1 with the parameters employed in the distribution of Ref. [163]—In accordance with the reference, the parton-level cross section here is taken to be non-zero also for $\hat{s} > \Lambda_{\text{eff}}$. Further, the distributions with an asymptotically safe KK sum with Minkowskian and Euclidean propagator, as discussed in the last chapter, in the quenched approximation are depicted as well as the SM distribution. Input parameters are $\Lambda_{\text{eff}} = 2.8\,\text{TeV}$ and $\Lambda_T = 2.8\,\text{TeV}$ respectively[1], $n = 3$ and $\mathrm{M}_\star = \Lambda_T$ for the AS distributions, PDF renormalization and factorization scales $\mu_R = \sqrt{\hat{s}}$ and $\mu_F = p_{\ell,T}$ (the absolute value of the lepton's momentum component transverse to the beam axis), and the MRST2001LO PDF set [165]. The statistical error in each bin is smaller than 3%.

The leptons analyzed here and in the rest of the text are the "true" leptons of the Drell-Yan processes; no detector simulation and no further background next to the SM contribution in (11.1) are included. Also, advanced simulation features such as multiple interactions and initial-state showering are turned off to simplify the system. Note that, since $m_{\ell\ell}$ is a Lorenz scalar, the $d\sigma/dm_{\ell\ell}$ distributions are robust against

[1] $\Lambda_{\text{eff}} = 2.8\,\text{TeV}$ corresponds to $\Lambda_{\text{eff}}^H = 2.5\,\text{TeV}$ in the Hewett convention [152] used in Ref. [163] with the conversion factor $\sqrt[4]{\pi/2}$.

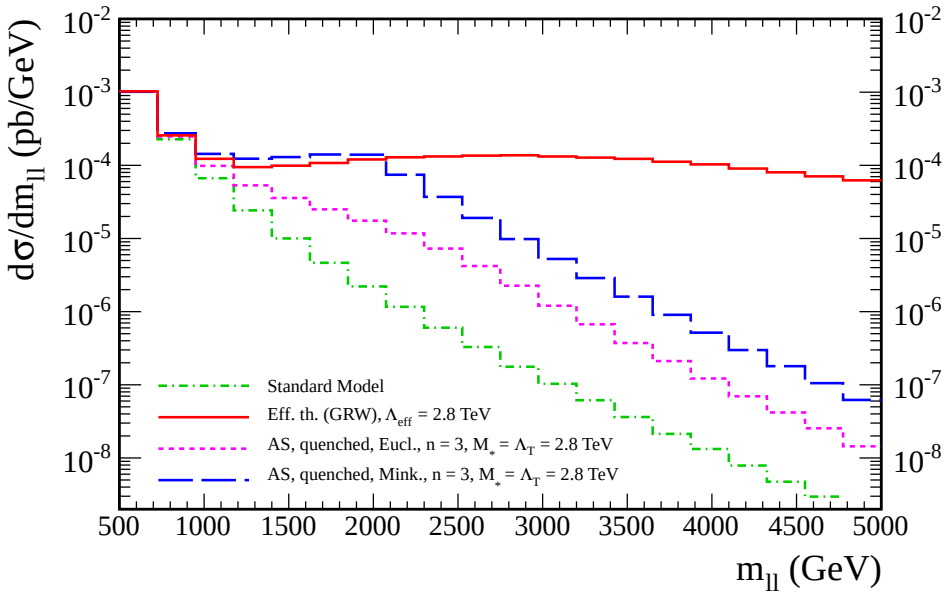

Figure 11.1: Graviton-enhanced dilepton invariant mass distribution for the LHC with 14 TeV center-of-mass energy and three lepton species. Parameters are chosen to reproduce the effective-theory reference distribution in Ref. [163]. See the text for further details.

boosts of the parton-level center of mass system perpendicular to the beam axis, the dominant effect of simulated initial-state radiation. On this level of simulation, $m_{\ell\ell}^2$ and $\hat{s}$ are identical.

The effective-theory distribution shown in Figure 11.1 generally agrees with the one published in Ref. [163], except being too small by roughly 6/7 in the highest bins. However, this is also the case for PYTHIA's standard effective-theory implementation by the authors of Ref. [163] and is therefore assumed to stem from a slight deviation of our parameter choices compared to the reference.

In addition to asserting that (11.1) and (11.2) have correctly been implemented, Figure 11.1 demonstrates several phenomena: Firstly, as well-known, the SM cross section dominates for small $m_{\ell\ell}$, but falls off steeply with increasing $m_{\ell\ell}$. Secondly, the effective-theory distribution is more or less flat in the resolution of the figure and for the small Λ_{eff} (relative to $\sqrt{s} = 14\,\text{TeV}$). Since the AS cross sections differ from the effective-theory cross section only by the non-constant $\mathcal{S}(\hat{s})$, this flatness implies that the shapes of the AS distributions in Figure 11.1 are qualitatively given by those of the $C(y^2)$ discussed in Chapter 10; most notably by $|C(y^2)|^2$ in the region where SM contributions are negligible.

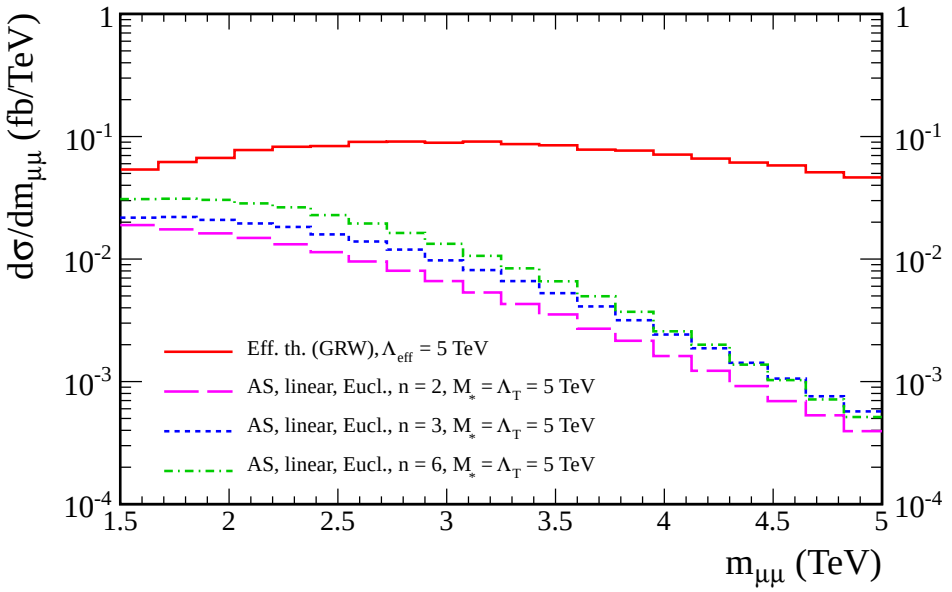

Figure 11.2: Pure gravity-induced dimuon invariant mass distribution for the LHC with $\sqrt{s} = 14\,\text{TeV}$. Parameters are chosen to reproduce histograms in Ref. [138]. The distribution is not divided by 0.175, the bin width in units of TeV.

11.2.1 AS cross sections

Cross sections for the AS graviton-enhanced Drell-Yan process have been discussed also in Ref. [138], for the Euclidean propagator signature. We review here some of these quantities in an independent calculation, and discuss those with the Minkowskian propagator in addition. To be compatible with Ref. [138], we apply the simplified acceptance cuts

$$p_{\ell,T} > 50\,\text{GeV} \quad \text{and} \quad \eta_\ell < 2.5, \tag{11.4}$$

on both leptons, where η_ℓ is the pseudorapidity of ℓ. We also adopt $\mu_F = p_{\ell,T}$ and use the CTEQ6.5 PDF set [166] in accordance with the reference. As before, the statistical error per bin is smaller than 3% for each histogram shown.

With our calculation, we can confirm the $d\sigma/dm_{\mu\mu}$ distributions of Ref. [138] in the linear approximation with an Euclidean propagator, except for $n = 2$, see Figure 11.2. For $n = 2$, we find the distribution to be smaller by a global approximate factor of two compared to the reference. At $m_{\mu\mu} = \Lambda_T = \text{M}_\star = 5\,\text{TeV}$, the differential distribution for $n = 3$ is expected to be larger than the $n = 2$ distribution by a factor of

$$\left(\frac{4\pi\, C^{(1)}_{n=3}(1)}{2\pi\, C^{(1)}_{n=2}(1)}\right)^2 \approx 1.45, \tag{11.5}$$

as it is in our figure (with $C^{(1)}(y^2)$ denoting the dimensionless KK sum in linear

approximation). In general, the unnormalized distributions in the reference differ from ours by a global normalization factor of $3.5/20 = 0.175$ (the bin width in units of TeV) [167]. For a comparison, the numeric values in all histograms shown here have to be multiplied by this factor, with the exception of Figure 11.2.

Figure 11.3 shows the pure gravitational differential cross section $d\sigma/dm_{\mu\mu}$ for muon pair production in the quenched approximation for various values of n and $\Lambda_T = \mathrm{M}_\star = 5\,\mathrm{TeV}$. Additionally the zero-$\hat{s}$ effective-theory distribution is shown for reference. As expected from the discussion of the transition behavior of the KK sums, the cross-over to the UV fixed-point scaling of the AS distributions already sets in at $m_{\ell\ell}$ much smaller than Λ_T. While the AS distributions—especially those for the Euclidean propagator—show little dependence on n, except for the overall normalization, they show sizable differences with respect to the signature of the propagator. Since the distributions are governed by $|C(y^2)|^2$, this is an expected effect. Likewise, a pronounced dependence of the shapes on the approximation scheme is expected following the discussion in Section 10.4. Note the instant transition between the IR scaling and the UV scaling in the distribution for the Minkowskian denominator at $m_{\mu\mu} \approx 3.5\,\mathrm{TeV} \approx \Lambda_T/\sqrt{2}$, which is characteristic for the quenched approximation. We come back to the approximation-scheme dependence in the next section.

We show the total cross sections for gravity-mediated muon-pair production in Figure 11.4. Since $\mathrm{M}_\star$ appears only as a global factor in the KK sum, see (10.4), cross sections $\sigma(\mathrm{M}'_\star)$ for a $\mathrm{M}'_\star = \zeta\mathrm{M}_\star$ can be obtained by multiplying $\sigma(\mathrm{M}_\star)$ by $1/\zeta^{2(n+2)}$. The large exponent in this rescaling factor—even for small n—implies a strong dependence of the cross section on the exact value of $\mathrm{M}_\star$, similarly to the well-known Λ_{eff} dependence of the effective-theory cross section. Exemplarily, even for 10% increased $\mathrm{M}_\star$, the cross section is reduced to less than half its value for all $n \geq 2$. In Figure 11.4 this effect is visualized by the dotted ($\zeta = 0.9$) and dashed ($\zeta = 1.1$) lines. Note that $\mathrm{M}_\star$, the Planck scale, is a fundamental quantity while Λ_{eff} merely parametrizes the finiteness of the KK sum.

The generic shape of the curves with their plateaus at $3 \lesssim n \lesssim 7$ (for $\zeta = 1$) is related to the surface of the unity sphere S_{n-1} (2.31), that has a maximum at $n = 7$, and the decrease of the KK sum's overall normalization $\sim c_0$.

11.2.2 Approximation-scheme dependence

The shape of the $d\sigma/dm_{\mu\mu}$ distribution is sensitive to the cross-over behavior between the Gaussian and non-Gaussian regimes. In general, this offers the opportunity that a very precisely measured $d\sigma/dm_{\mu\mu}$ distribution may allow us to gain insight in the details of the transition region, once n is determined elsewhere.

To assess the dependence of the expected distributions on the approximation-scheme, the pure gravitational part of the distribution is depicted in Figure 11.5 for $n = 3$ in the quenched, linear, and quadratic approximations. Other parameters are as in the last section. The approximation-dependent transition scales are matched at $\hat{s} = 0$ according to (10.9) and read $\Lambda_T^{(0)} = 5\,\mathrm{TeV}$, $\Lambda_T^{(1)} \approx 5.8\,\mathrm{TeV}$, and $\Lambda_T^{(2)} \approx 5.5\,\mathrm{TeV}$. The figure shows that the direct impact of the cross-over region on the shape of the $d\sigma/dm_{\mu\mu}$

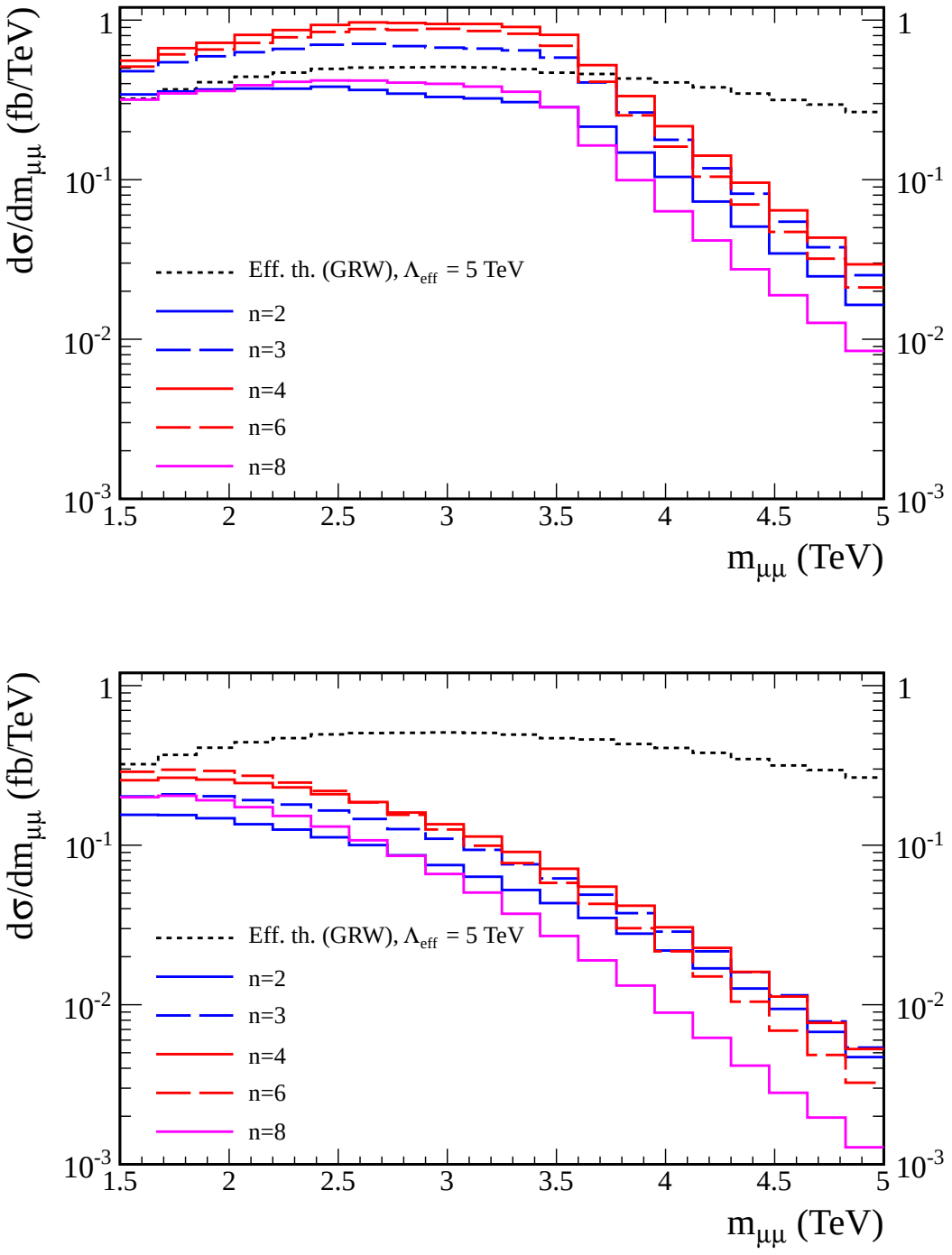

Figure 11.3: Pure gravitational part of the differential cross sections for muon pair production at several values of n, with Minkowskian (top panel) and Euclidean (bottom panel) propagators—quenched approximation with $\Lambda_T = \mathrm{M}_\star = 5\,\mathrm{TeV}$ and $\sqrt{s} = 14\,\mathrm{TeV}$.

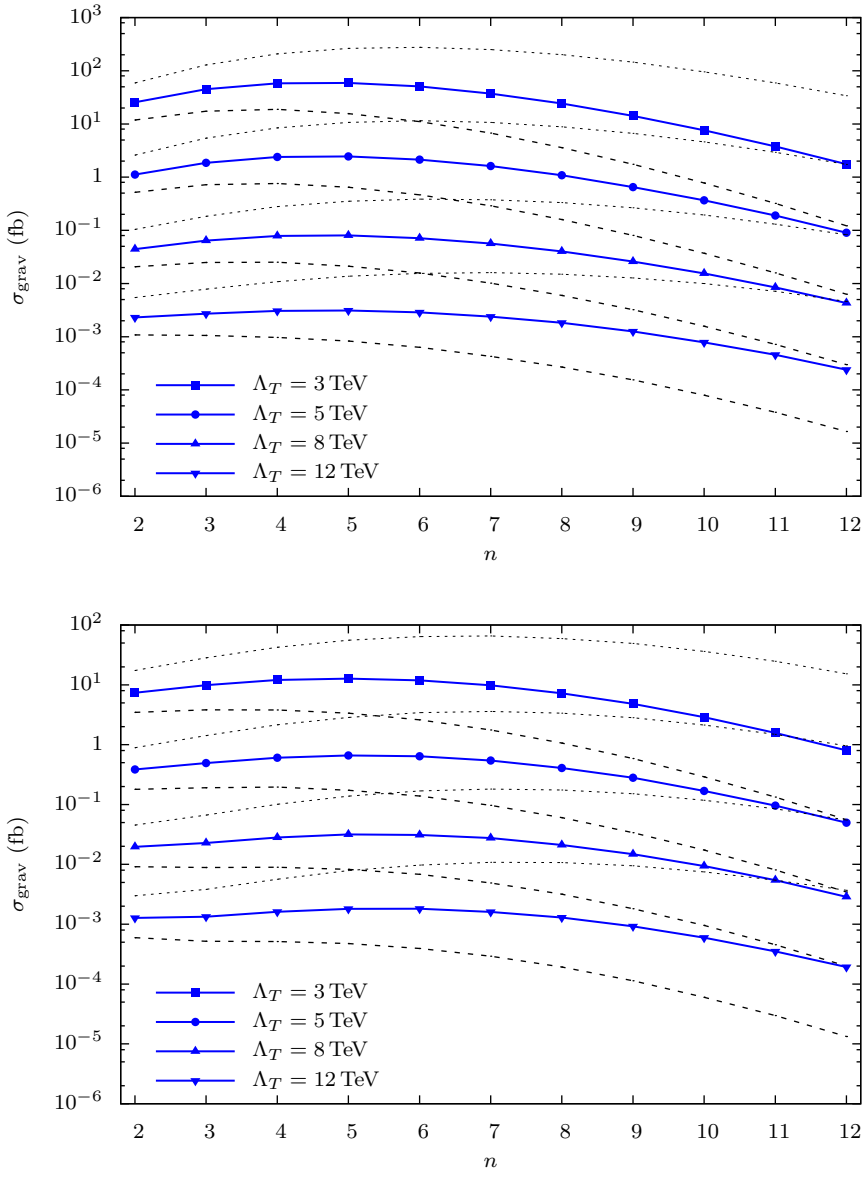

Figure 11.4: Integrated cross sections for graviton-induced muon pair production at the LHC with $\sqrt{s} = 14\,\mathrm{TeV}$ and the cuts in (11.4) without the SM contributions. The lines connecting the points at integer values of n are employed to guide the eye. Solid lines: $\mathrm{M}_\star = \Lambda_T$. Dashed (dotted) lines correspond to the solid curves above (below) with $\mathrm{M}_\star = 1.1\Lambda_T$ ($\mathrm{M}_\star = 0.9\Lambda_T$).

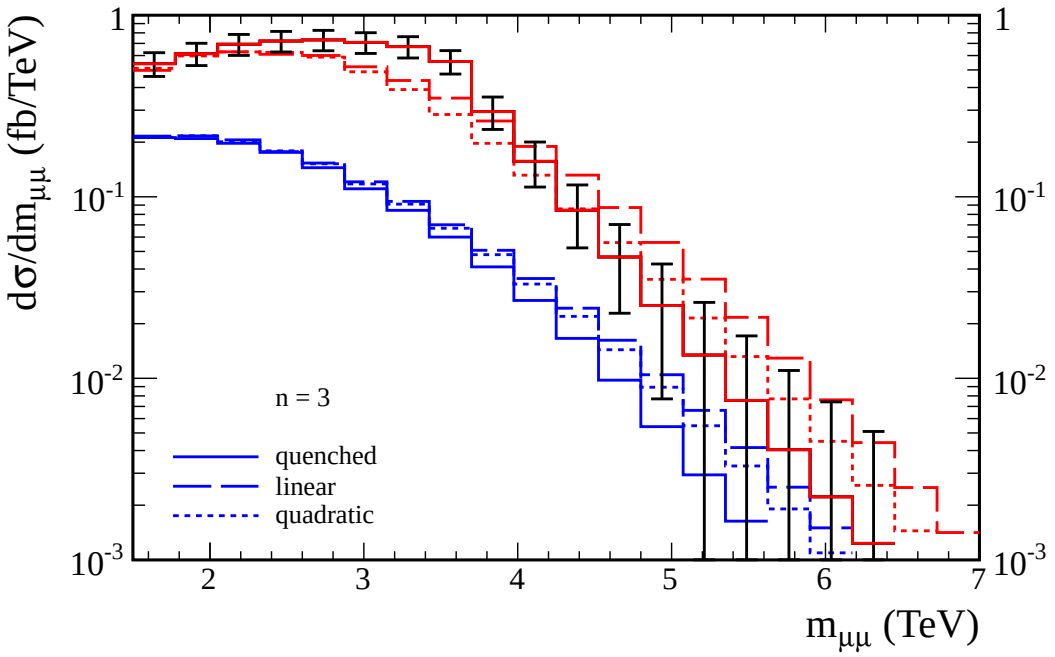

Figure 11.5: Pure gravitational part of the differential cross sections for muon pair production in three extra dimensions in the quenched, linear, and quadratic approximations ($\sqrt{s} = 14\,\text{TeV}$). Blue: Euclidean propagator; red: Minkowskian propagator. $M_\star = \Lambda_T^{(0)} = 5\,\text{TeV}$, $\Lambda_T^{(1)} \approx 5.8\,\text{TeV}$, and $\Lambda_T^{(2)} \approx 5.5\,\text{TeV}$; matched according to (10.9). The error bars depict the statistical 1σ environment expected for $300\,\text{fb}^{-1}$ of data.

distribution is less pronounced in the linear and quadratic approximations compared to the quenched approximation even for the Minkowskian propagator.

In the Minkowskian case, the distribution in the quenched approximation shows its characteristically late but instant transition to the UV regime, resulting in larger cross sections in the bins up to $m_{\mu\mu} \approx 3.5\,\text{TeV} \approx \Lambda_T/\sqrt{2}$. Apart from that, the distributions differ by the steepness of their decrease with increasing $m_{\mu\mu}$. All the distributions have the same large-$m_{\mu\mu}$ scaling, but this limit is not reached in the region shown. In the large-$m_{\mu\mu}$ limit, the ratio of the differential cross sections is given by

$$\left(\frac{g_{\text{NG}}^{(i)}}{g_{\text{NG}}^{(j)}}\right)^2 = \left(\frac{\Lambda_T^{(i)}}{\Lambda_T^{(j)}}\right)^{2(n+2)} = \left(\frac{c_0^{(j)}}{c_0^{(i)}}\right)^{\frac{2(n+2)}{(n-2)}} \tag{11.6}$$

for the approximations i and j, following from (10.4) and (10.23).

The total cross sections enlisted in Figure 11.4 imply that the quenched distribution for the Minkowskian propagator signature in Figure 11.5 is sampled over 550 events approximately for $\mathcal{L}_{\text{int}} = 300\,\text{fb}^{-1}$ at the 14-TeV LHC. The corresponding statistical 1σ environment is depicted in Figure 11.5 as error bars. (Note that the distributions

themselves are generated with a statistical error of less than 3% per bin as before.) Since the statistical errors are of the same order of magnitude as the differences among the approximation schemes, the latters' impact on the findings within the standard LHC program presumably are negligible at the benchmark point $\Lambda_T \sim \mathrm{M}_\star = 5\,\mathrm{TeV}$. With $3000\,\mathrm{fb}^{-1}$ of data collected in the future high-luminosity upgrade HL-LHC [168], the statistical errors would be small compared to the approximation-scheme dependence, however.

There is no experimental sign for derivations from the SM in the dilepton channel at the time of writing [164, 169]. Therefore, only exclusion limits on the model's integrated cross section within signal bins can be derived from data. To assess the sensitivity of the cross section on the approximation scheme, we show the ratios of the total cross sections in the three approximations for $\sqrt{s} = 14\,\mathrm{TeV}$ in dependence on $\Lambda_T^{(0)}$ in Figure 11.6. The approximation-scheme dependence universally is more pronounced for small $\Lambda_T^{(0)}$. This can be understood recalling that contributions to cross section from the region $2\,\mathrm{TeV} \lesssim m_{\mu\mu} \lesssim 4.5\,\mathrm{TeV}$ generically are enhanced by the parton luminosities and the kinematic factors in (11.1), (11.2)—see the effective-theory distribution in Figure 11.3. The smaller Λ_T is, the more the total cross section is dominated by the fixed-point regime with $C(y^2) \sim 1/y^4$. The approximation-scheme dependence in this region of Figure 11.3 stems from the zero-$\hat{s}$ scale matching. Since this is introduced to minimize the approximation-scheme dependence in the low-$\hat{s}$ regime (i.e. for large Λ_T), its use is discouraged in regions where the cross section is dominated by the fixed-point scaling. In an experimental search, the minimal-$m_{\ell\ell}$ cut of the signal region controls the minimal Λ_T for which the fixed-point scaling dominates.

11.2.3 Bounds from dilepton LHC data

Here we derive bounds on the AS parameters from experimental exclusion limits on Λ_{eff}, the characteristic mass scale in the GRW parametrization in (10.7); see also Ref. [4]. The CMS collaboration has measured the $m_{\ell\ell}$ distributions of dielectron and dimuon events at the LHC with a center-of-mass energy of $\sqrt{s} = 8\,\mathrm{TeV}$ with the integrated luminosities $20.6\,\mathrm{fb}^{-1}$ and $19.6\,\mathrm{fb}^{-1}$ [164]. No excess over the SM expectation is found, and the collaboration states a 95%-CL limit on Λ_{eff} of 4.15 TeV, derived from the combination of both data samples and a k-factor of 1.3. The limit is obtained employing a minimal-$m_{\ell\ell}$ cut $m_{\ell\ell}^{\mathrm{min}} = 1.8\,\mathrm{TeV}$ and with setting the parton-level cross section to zero at $\hat{s} > \Lambda_{\mathrm{eff}}^2$.

Having two physical scales in the AS scenario, the experimental bound on Λ_{eff} translates to cuts through the Λ_T-$\mathrm{M}_\star$ plane. The CMS bound is adapted here to the AS scenario in the following procedure:

1. We recalculate the cross section for $\Lambda_{\mathrm{eff}} = 4.15\,\mathrm{TeV}$ with $m_{\ell\ell} > 1.8\,\mathrm{TeV}$ with PYTHIA 8.170.

2. For a given number of extra dimensions, we fix $\mathrm{M}_\star$ and vary Λ_T so that the AS cross section matches the effective-theory cross section in the signal bin.

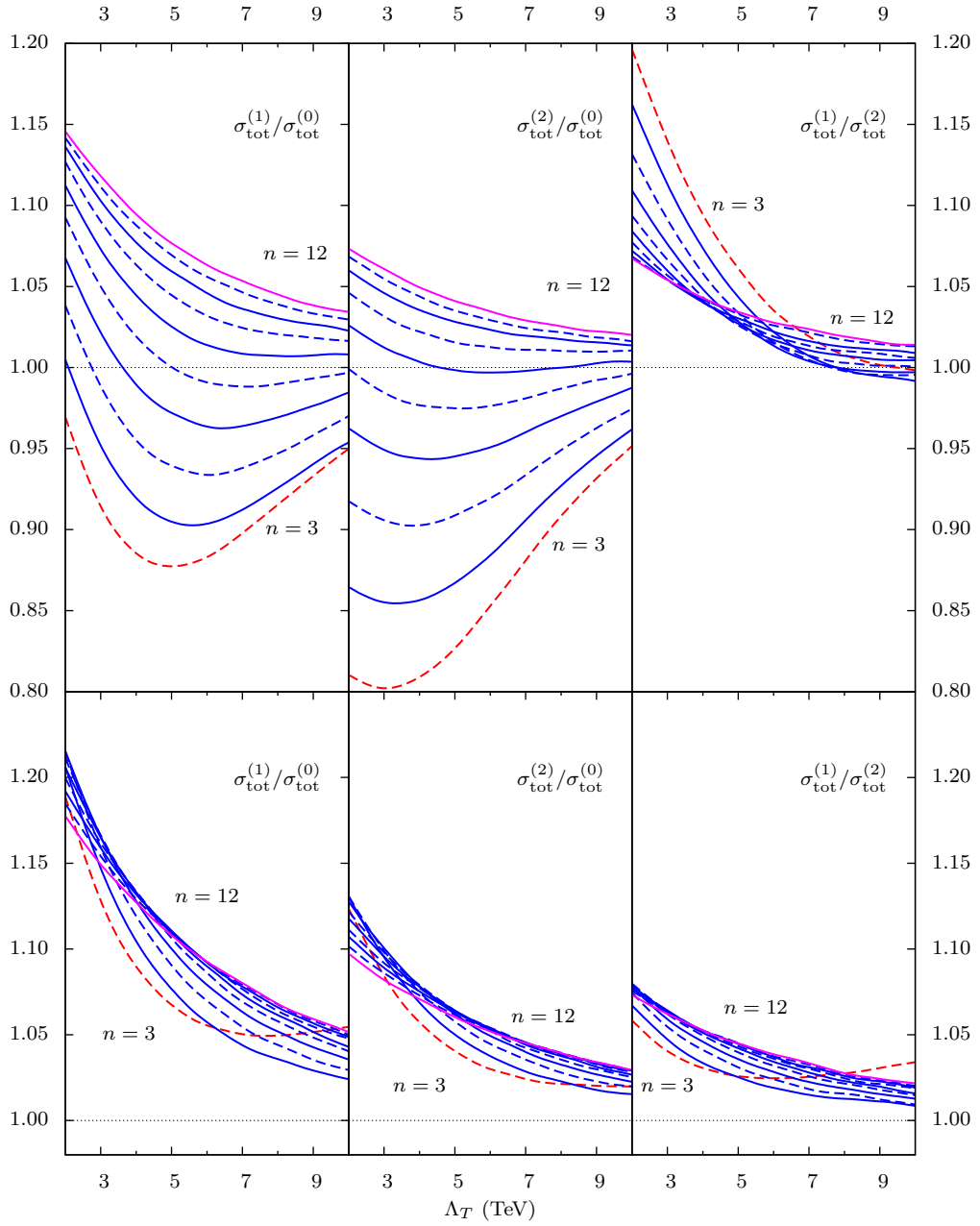

Figure 11.6: Ratios of the pure gravitational total $pp \to \ell^-\ell^+$ cross sections in the three approximations for various values of n in dependence on $\Lambda_T^{(0)}$ [transition-scale matching according to in (10.9)]. Upper panels: Minkowskian propagator, bottom panels: Euclidean propagator. Dashed lines: odd n, solid lines: even n; $\sqrt{s} = 14\,\text{TeV}$.

We perform the calculation for each PDF set used in Ref. [164] to assess the PDF uncertainty of the adaption procedure. These PDFs are the central fits of the CT10, MSTW08, and NNPDF21 sets [170]. In addition to PDF variation, we perform the calculation for two factorization-scale choices, $\mu_F = p_{\ell,T}$ and $\mu_F = \sqrt{\hat{s}}$.

The results are depicted in Figures 11.7–11.9, for the quenched, linear, and quadratic approximations. For several values of n, the bounds are depicted as thick, curved lines. Transition scales above them are in conflict with the experimental findings. The PDF and factorization-scale uncertainty on Λ_T from the adaption procedure is at the 2%-percent level for $n = 2$ and falls below the 1%-percent level for $n > 2$. There are two distinct regions where the functional form of the curves can be understood in terms of their asymptotic behavior: For large $\mathrm{M}_\star$ and Λ_T, the typical partonic center-of-mass energies are small compared to Λ_T so that the KK sum can be approximated by its value at $\hat{s} = 0$. $\mathrm{M}_\star$ and Λ_T for $n > 2$ then scale as

$$\frac{4\pi}{\Lambda_{\mathrm{eff}}^4} = c_0\, S_{n-1} \frac{\Lambda_T^{n-2}}{\mathrm{M}_\star^{n+2}}, \tag{11.7}$$

where Λ_{eff} is the experimental bound in the GRW parametrization. This scaling is depicted for $n = 3$–5 as black lines near the AS bounds at higher values of $\mathrm{M}_\star$. As expected from the discussion in Section 10.4, the AS cross section in the Euclidean case shows a larger deviation from the zero-$\hat{s}$ scaling in (11.7) than in the Minkowskian case. [For $n = 2$, the scaling of $\Lambda_T(\mathrm{M}_\star)$ at high Λ_T is exponential due to the KK sum's logarithmic IR divergence, see (10.13).]

The second region where the functional form of the bounds readily can be understood is the small-$\mathrm{M}_\star$ regime. In this region, the strong minimal-$m_{\ell\ell}$ cut of the signal bin constrains the AS cross section to its UV-scaling part depending only on $(\Lambda_T/\mathrm{M}_\star)^{(n+2)}$. The bound is therefore only sensitive to both scales' ratio and scales linearly with $\mathrm{M}_\star$. Note that the hard minimal-$m_{\ell\ell}$ cut limits the sensitivity of the analysis in this small-$\mathrm{M}_\star$ region. Since virtual gravitons nevertheless would significantly alter the $d\sigma/dm_{\ell\ell}$ distribution for $m_{\ell\ell}$ below $m_{\ell\ell}^{\mathrm{min}} = 1.8\,\mathrm{TeV}$, earlier experimental searches or those with smaller $m_{\ell\ell}^{\mathrm{min}}$ potentially provide more severe bounds in this region.

Cuts through the $\mathrm{M}_\star$-Λ_T plane

The ratio $\Lambda_T/\mathrm{M}_\star$ determines the value of the non-Gaussian fixed point through (9.12). We therefore can exemplarily compare the prediction of the fixed point in the EH truncation in (9.7) with the dilepton bound in the $\mathrm{M}_\star$-Λ_T plane. The EH prediction is depicted as straight lines in Figures 11.7–11.9, colored as the associated dilepton bound. Since the areas above the dilepton curves are in conflict with the data, the points where these curves intercept with the EH prediction mark the smallest values of $\mathrm{M}_\star$ and Λ_T where the prediction is in agreement with the data. We list these lowest values of $\mathrm{M}_\star$ and Λ_T in Table 11.1. (We quote the scales here at the precision of $\Lambda_{\mathrm{eff}} = 4.15\,\mathrm{TeV}$; the PDF-$\mu_F$ uncertainty of adaption procedure is far below the %-level for the EH cuts.)

As an alternative to the prediction in the EH truncation, we can derive minimal values for the identified scales $\Lambda_T = \mathrm{M}_\star$ that are in agreement with the CMS bounds. The corresponding cut through the $\mathrm{M}_\star$-Λ_T planes is depicted as a black, dash-dotted

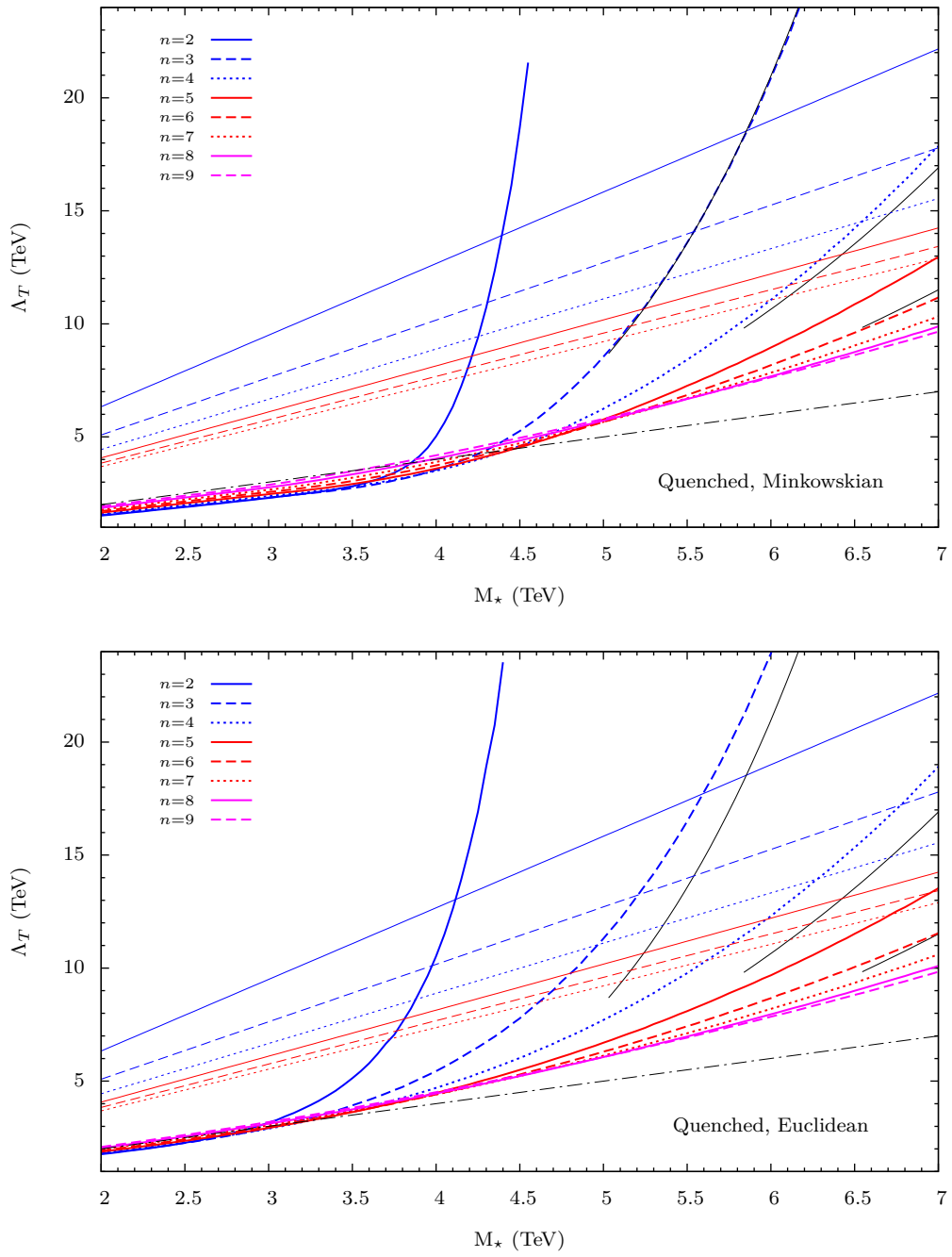

Figure 11.7: Bounds on the fundamental Planck scale $M_\star$ and the transition scale Λ_T for several values of n, based on a 8-TeV, 20-fb^{-1} CMS search in the dilepton channel [164]. Regions above the thick, curved lines are excluded. Thin black curved lines: results in the zero-$\hat{s}$ approximation. Thin straight lines: predictions in the EH truncation. Dash-dotted line $\Lambda_T = M_\star$. Upper panel: Minkowskian propagator, lower panel: Euclidean propagator (both quenched approximation; no scale matching).

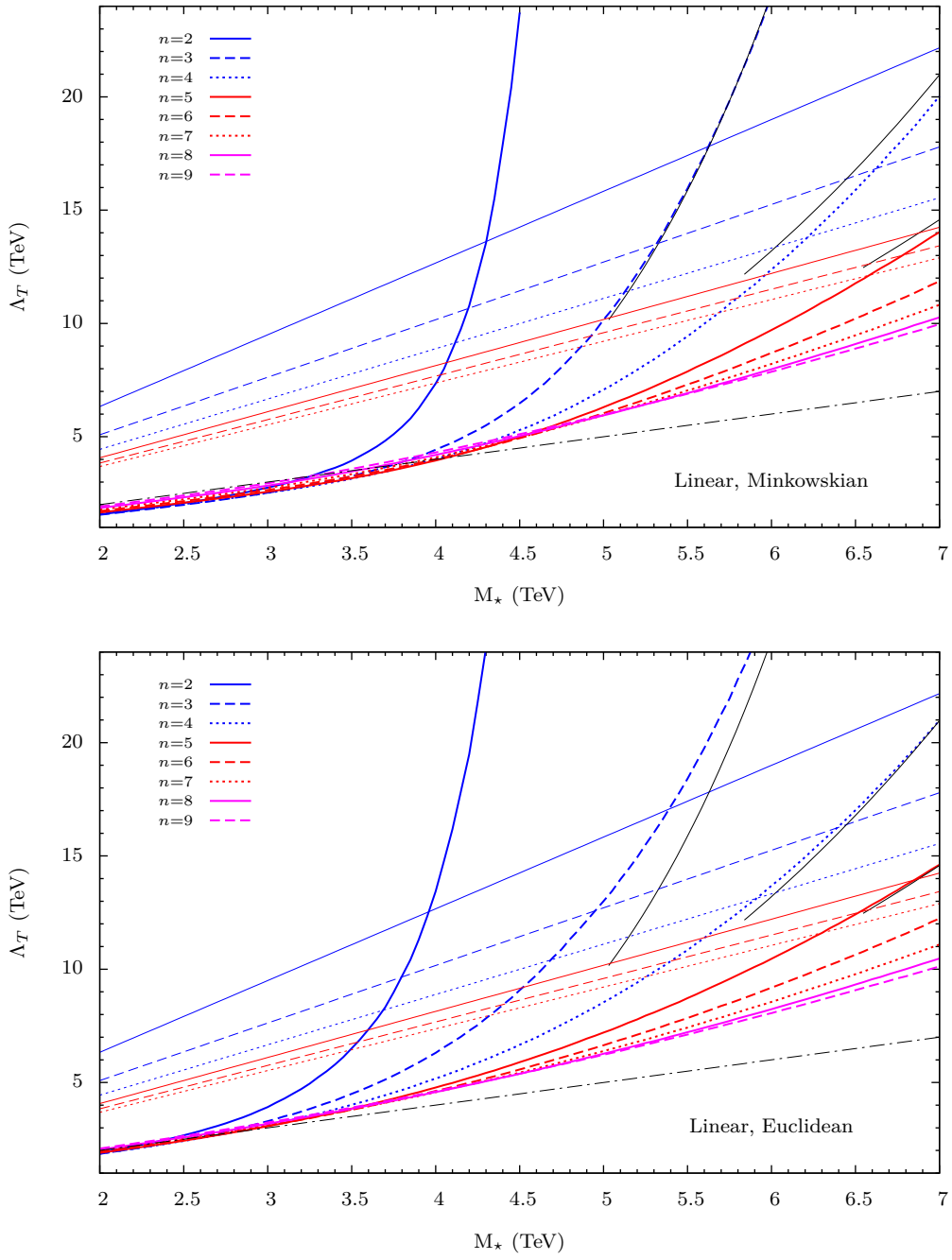

Figure 11.8: The same as Figure 11.7, in the linear approximation; no scale matching.

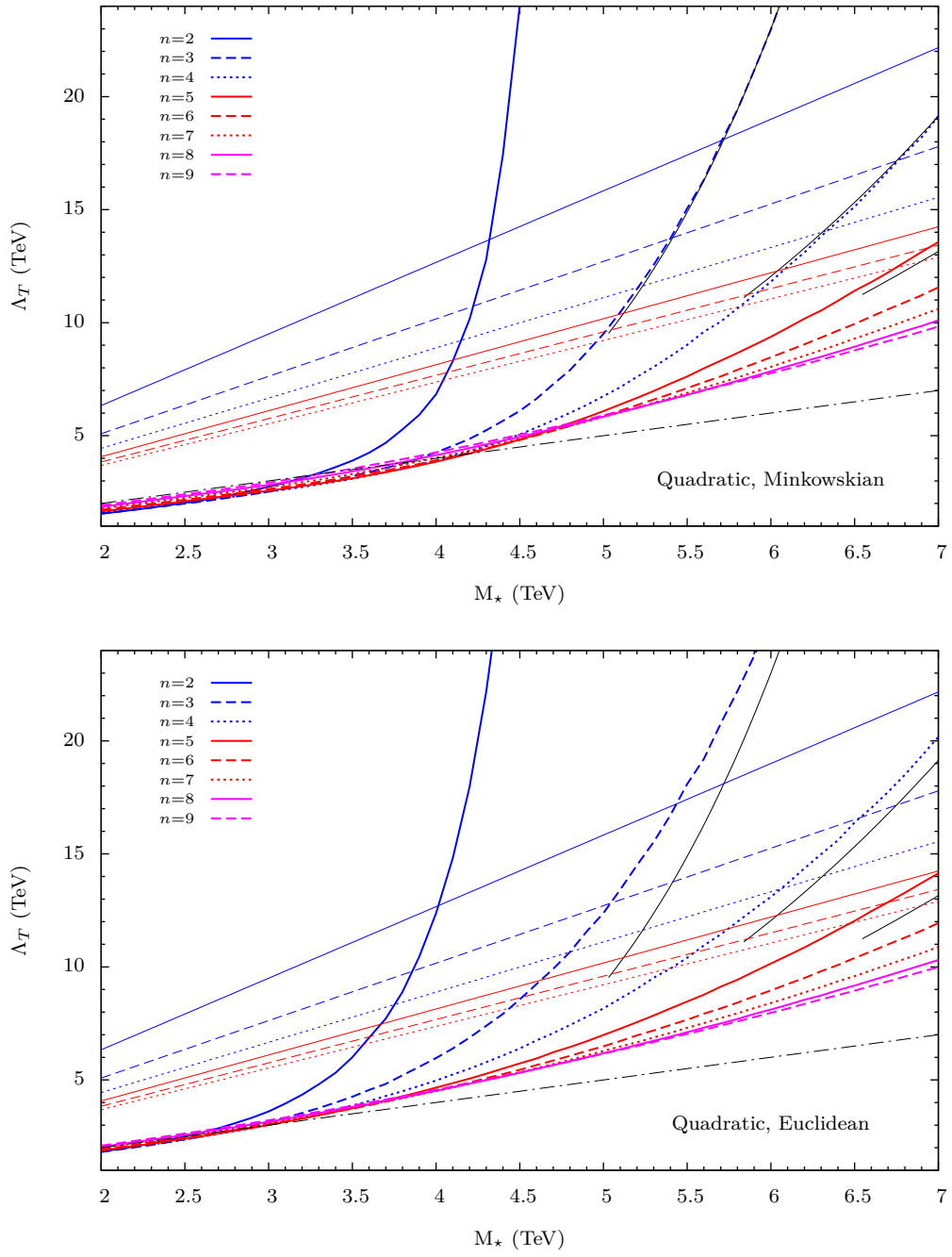

Figure 11.9: The same as Figure 11.7, in the quadratic approximation; no scale matching.

	Minkowskian					
	quenched		linear		quadratic	
n	$M_\star$ (TeV)	Λ_T (TeV)	$M_\star$ (TeV)	Λ_T (TeV)	$M_\star$ (TeV)	Λ_T (TeV)
2	4.39	13.9	4.29	13.6	4.31	13.7
3	5.54	14.1	5.31	13.5	5.40	13.7
4	6.55	14.6	6.21	13.8	6.36	14.1
5	7.38	15.0	7.03	14.3	7.19	14.6

	Euclidean					
	quenched		linear		quadratic	
n	$M_\star$ (TeV)	Λ_T (TeV)	$M_\star$ (TeV)	Λ_T (TeV)	$M_\star$ (TeV)	Λ_T (TeV)
2	4.15	13.2	3.92	12.4	4.01	12.7
3	5.20	13.2	4.94	12.6	5.03	12.8
4	6.28	13.9	5.88	13.1	6.05	13.4
5	7.25	14.7	6.84	13.9	7.02	14.3

Table 11.1: Minimal values of $M_\star$ and Λ_T in agreement with the CMS dilepton data and the fixed-point prediction in the Einstein-Hilbert truncation (no scale matching).

line in Figures 11.7–11.9. This line intercepts with the CMS bounds in regions where the AS cross section in the signal bin is dominated by the UV fixed-point scaling $\sigma \propto (\Lambda_T/M_\star)^{2(n+2)}$, in particular for the Euclidean propagators. In this region, the absolute differences of the cross sections in the three approximations are small for unmatched transition scales. However, since the dependence on the absolute values of the individual scales—the deviation from fixed-point scaling—is suppressed, bounds on $M_\star = \Lambda_T$ would differ distinctly for the three approximations if derived in this region. We give bounds on $M_\star = \Lambda_T$ in Table 11.2 in the quenched approximation. Because of the approximations made in the semi-numerical calculation, bounds on $M_\star = \Lambda_T$ cannot be reliably calculated in linear and quadratic approximations if Λ_T approaches the $m_{\ell\ell}^{\min}$ cut, see the discussion in Appendix C. The larger sensitivity of the $\Lambda_T = M_\star$ bound on small variations of the cross sections is signaled by an increase of the uncertainty associated with the PDF and factorization-scale choices in the adaption of the $\Lambda_{\text{eff}} = 4.15\,\text{TeV}$ bound. The increase is visible for larger n in the Euclidean case, see Table 11.2.

	Minkowskian		Euclidean	
n	Λ_T (TeV)	$\epsilon_{\rm rel}$ (%)	Λ_T (TeV)	$\epsilon_{\rm rel}$ (%)
2	3.85	0.5	2.87	1.3
3	4.25	0.3	3.10	1.3
4	4.44	0.2	3.22	1.4
5	4.47	0.2	3.22	1.4
6	4.38	0.3	3.06	2

Table 11.2: Minimal values of $\mathrm{M}_\star = \Lambda_T$ in agreement with the CMS dilepton data, quenched approximation. $\epsilon_{\rm rel}$: relative PDF and μ_F uncertainty of the adaption procedure.

11.2.4 Comparison to real-graviton searches

We observe two characteristic differences, comparing the bounds on Λ_T and $\mathrm{M}_\star$ obtained in the last section with analogue bounds derived from real-graviton contributions to mono-jet+$\not{E}_T$ production rates [139, 171] (see Figure 11.10):

1. An amplitude for virtual-graviton exchange is sensible to the UV regime of gravity irrespective where it takes over, because of the full KK tower contributing. Dilepton searches therefore impose bounds on Λ_T for any $\mathrm{M}_\star$ irrespective how large $\mathrm{M}_\star$ is, see Figures 11.7–11.9. In contrast, jet+$\not{E}_T$ searches yield no bound on Λ_T, once $\mathrm{M}_\star$ exceeds a critical value. They only are sensitive to the details of the transition regime if the mass of the heaviest graviton that can be produced is $\mathcal{O}(\Lambda_T)$.

2. The two types of searches are complementary with respect to their sensitivity in dependence on n. The real-graviton search gives the tightest bound on Λ_T and $\mathrm{M}_\star$ for $n = 2$. In the virtual-graviton case, the bounds are tighter the larger n is. To explain this, we consider the large-Λ_T regime. For virtual-graviton exchange, the increased sensitivity for larger n then stems from the power-scaling in (11.7). This scaling itself originates from the n-dependence in (2.30). In gluon+graviton production at a fixed $\hat{s}$, the emitted gluon is softer the larger the mass of the KK graviton is. The larger n is, the more are higher graviton masses—hence softer gluons—favored by the KK-state density [54]. Since the gluon energy both controls $\not{E}_T$ and jet-p_T, the jet+$\not{E}_T$ signal is smaller the larger n is, given a fixed $\mathrm{M}_\star$. Conversely bounds on $\mathrm{M}_\star$ from the jet+graviton channel are weaker the larger n is.

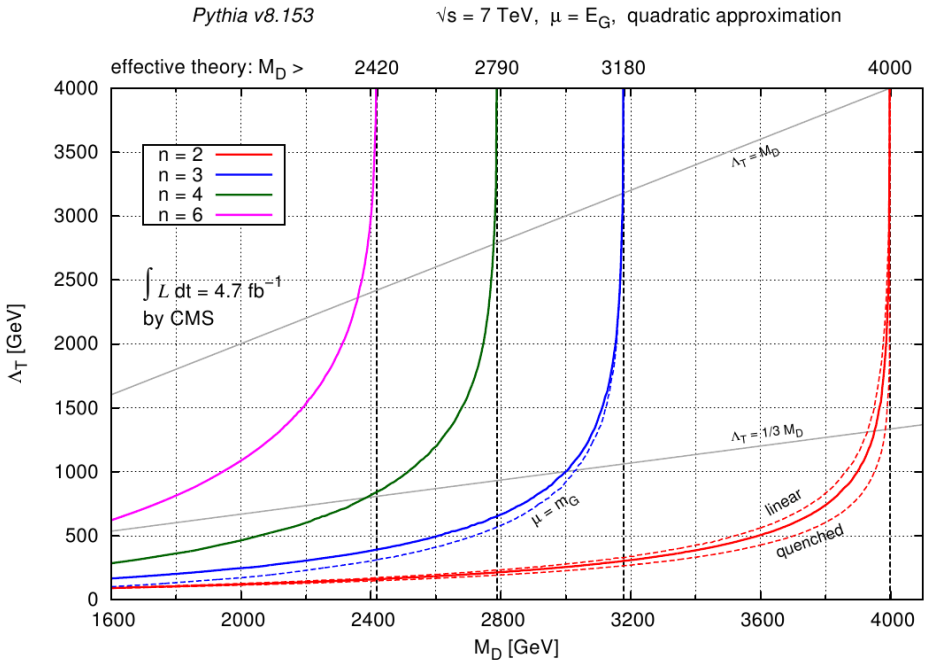

Figure 11.10: Bounds on the fundamental Planck scale $m_D \equiv \mathrm{M}_\star$ and the transition scale Λ_T in the quadratic approximation, derived from approximately $5\,\mathrm{fb}^{-1}$ of mono-jet+$\not{E}_T$ CMS data at 7 TeV [171]. The upper-left area is excluded. Figure from Ref. [139].

12 Conclusion of Part III

The existence of compactified large extra dimensions as conjectured in the ADD model would offer the exiting possibility to observe quantum-gravity effects at the LHC. Such an observation would not only resolve the EW hierarchy problem, it also can hint at the nature of high-energy quantum gravity.

LED quantum gravity would have intriguing implications for collider physics. Virtual gravitons can modify the cross sections of SM pair production processes. Real gravitons can generate mono-jet+$\not{E}_T$ events. Finally, mini black holes can be produced if the fundamental Planck scale is low enough. The predictions for these phenomena depend on the high-energy regime of quantum gravity. Real-graviton production is well-defined as a low-energy quantum-gravity effect as long as the maximal graviton mass tested is well below the transition scale to the high-scale gravity regime. Virtual-graviton amplitudes, requiring a summation over complete KK towers (i.e. infinite graviton momenta), in contrast are sensitive to the high-scale regime, irrespective where it takes over. Also the description of BH-production thresholds requires a full quantum-gravity description. The Asymptotic Safety Scenario is an elegant conjecture for these high-scale dynamics—elegant in that only a minimum of new, hypothetical structures have to be introduced: The metric fluctuation is retained as the fundamental degree of freedom at all energies, and fixed-point RG scaling is an effect known from other strong coupling theories such as asymptotically free QCD. Moreover, through its RG trajectories, AS exhibits a well-defined connection of the fundamental UV sector to classical general relativity as its IR limit. Calculations of the RG flow beyond the minimal EH truncation provide confidence that there is indeed a universal UV fixed-point regime with only a finite number of relevant operators.

We discussed the implications of asymptotically safe gravity on Feynman amplitudes for s-channel virtual-graviton exchange for n extra spatial dimensions. Dressing the propagators of the KK graviton states with the $(4{+}n)$-dimensional graviton wave-function renormalization factor and identifying the renormalization scale with a $(4{+}n)$-dimensional graviton momentum, we calculated finite, UV-safe amplitudes. For $n = 2$–12 extra dimensions, we solved the KK sum over the dressed s-channel graviton propagator analytically in the quenched approximation of the RG evolution and semi-numerically in the linear and quadratic approximations, both for Euclidean and Minkowskian propagators. The scales determining the overall normalizations of the KK sums, Λ_T and $\mathrm{M}_\star$, are physical quantities, in contrast to Λ_{eff} in the zero-$\hat{s}$ effective-theory approximation which merely regularizes the KK sum.

The finite s-channel KK sums are common to the virtual-graviton contributions to any SM $2 \to 2$ pair-production process. We discussed the collider phenomenology of AS graviton-exchange exemplarily for dilepton production. For this we provided an implementation of the process in the multipurpose Monte-Carlo generator PYTHIA 8.

Total cross sections for $pp \to \ell^+\ell^-$ and the associated invariant-mass distributions of the lepton pairs are found to show sizable approximation-scale dependencies for transition-scales smaller than or of the order of the collider's center-of-mass energy. However, for the benchmark values $\mathrm{M}_\star = 5\,\mathrm{TeV}$ and $\Lambda_T \sim 5\,\mathrm{TeV}$, these approximation-scale dependencies seem not to be relevant for $d\sigma/dm_{\ell\ell}$ distributions in the reach of the LHC due to small event counts. The prediction of AS in the EH truncation, constituting an approximate upper limit on $\Lambda_T/\mathrm{M}_\star$ consistent with unitarity, are found to be compatible with CMS limits from $20\,\mathrm{fb}^{-1}$ of 8-TeV data [164] if $\mathrm{M}_\star \gtrsim 4\,\mathrm{TeV}$ and $\Lambda_T \gtrsim 13\,\mathrm{TeV}$, the bounds are tighter for larger n and lower for the identification $\Lambda_T = \mathrm{M}_\star$. The bounds show a reversed n-dependence compared to those that can be obtained from searches for real-gravitons in jet+$\not{E}_T$ channels.

There are several apparent directions the work presented here can be extended. The KK sums as implemented in PYTHIA can be reused for other pair-production processes such as $pp \to \gamma\gamma$. This is in preparation at the time of writing in the context of a master's thesis [172]. If an excess in pair-production data is found, it would be worthwile to fully include the KK sums for either the linear or the quadratic approximation as analytically expressions in PYTHIA, since the shape of the distribution differs sizably among the approximations.

With AS, virtual-graviton amplitudes are well-defined also for interaction energies well above the fundamental Planck scale. However, at these energies they could be rendered completely irrelevant: Black holes, having a well-defined minimal mass in AS [140], spectacularly could signal an end of short-distance physics if the distances probed fall below the minimal BH-event horizon [137].

Overall conclusion and outlook

At the time of writing, the LHC has entered its first long shutdown and is scheduled to resume operation in 2015. So far, both general-purpose experiments ATLAS and CMS have recorded about $30\,\text{fb}^{-1}$ of pp-collision data each that led to the spectacular discovery of a particle consistent with the SM Higgs. After three years of LHC measurements, there still is no evidence for fundamental deviations from the SM.

The unknown source of flavor violation and the EW hierarchy problem are two aspects where the SM is in need of improvements. They must be addressed theoretically—in particular now that EW-symmetry breaking received further experimental support through the observation of a Higgs boson. Efforts to resolve the hierarchy problem have resulted in spectacular new concepts such as spacetime supersymmetry or an enlarged spacetime dimensionality. In this thesis we discussed collider implications of two models incorporating these concepts, the MSSM implementing broken supersymmetry and the ADD model of extra dimensions.

Connected to the EW scale through the hierarchy problem, signals of these models are expected to show up around the TeV scale, which is probed at the LHC. None of the hypothesized sparticles signaling a broken spacetime SUSY is observed. Also there are no deviations from SM signatures that would signal extra-dimensional low-scale gravity. Especially the MSSM parameter space, whose stop sector is linked to the 1-TeV scale through the naturalness of the observed Higgs mass, is already significantly constrained.

A rich experimental program will allow to further test the TeV scale in the future: The LHC will continue with Run II in 2015, delivering a luminosity of $45\,\text{fb}^{-1}$/year at 13–14 TeV for 3–4.5 years [173, 174]. After a second long shutdown, it will enter a Run III and in total will deliver at least $300\,\text{fb}^{-1}$ of data [173]. After that the LHC will be upgraded to the high-luminosity LHC (HL-LHC) which is expected to increase the total integrated luminosity to $3000\,\text{fb}^{-1}$ [168, 173]. Complementary to the hadron-collider programs there are two competing electron-collider projects, the International Linear Collider (ILC) with $\sqrt{s} = 0.5$–1 TeV [175] and the Compact Linear Collider (CLIC) with $\sqrt{s} = 1$–3 TeV [176]. These lepton-colliders would allow to measure couplings and masses of newly discovered particles with a precision unmatched by the LHC program. However the prospects for a realization of either of these projects most certainly will depend on the findings of the LHC's Run II and the mass scales involved in potential deviations from the SM.

Irrespective the experimental long-term schedules, the next few years of LHC operation will be decisive. They will decide on the fate of TeV-scale spacetime supersymmetry and probably on the fate of four-dimensional spacetime. Whatever the outcomes are, the coming LHC results inevitably will change the landscape of high-energy physics.

Appendices

A Miscellaneous formulae

A.1 Hadronic cross sections in the parton model—PDFs

In the parton model [177], the hard scattering of two hadrons A and B can be described in terms of the scatterings of their constituents (gluons, quarks) called partons for historical reasons. Because of asymptotic freedom in QCD, parton a can be considered to move freely with three-momentum $\boldsymbol{p}_a = x_a \boldsymbol{p}_A$ in the interaction if the energy scale Q, characteristic for the scattering process, is much larger than the hadronic mass scale $\Lambda = \mathcal{O}(1\,\mathrm{GeV})$. For $2 \to 2$ scattering, this is assured if $p_T \gg \Lambda$, where p_T is the transverse momentum of the final states.

The probability distribution for finding parton a with momentum fraction x (along the beam axis) inside hadron A is described by the parton distribution function (PDF) $f_{a/A}(x)$. Being governed by non-calculable long-range effects, PDF sets usually are obtained in fits to experimental data. In terms of the PDFs, the inclusive total cross section for dilepton production, $AB \to \ell\bar{\ell}X$ exemplary reads [113]

$$\sigma_{ab\to\ell\bar{\ell}X} = \sum_{a,b} \int_0^1 d\tau \int_\tau^1 \frac{dx_a}{x_b} \left[f_{a/A}(x_a) f_{b/B}(x_a)(\tau/x_a) + (A \leftrightarrow B \text{ if } a \neq b) \right] \hat{\sigma}_{ab\to\ell\bar{\ell}}(\hat{s} = \tau s). \tag{A.1}$$

Here X denotes other products of the hadron scattering, $\hat{\sigma}$ the total partonic cross section. $\sqrt{\hat{s}}$ and $\sqrt{s}$ denote the partonic and hadronic center-of-mass energies. The parton model assumes incoherent scattering.

The inner integral in (A.1), the parton luminosity, is a useful quantity to assess the relative weight of a particular parton-level cross section with $\hat{s} = \tau s$:

$$\frac{d\mathcal{L}(\tau)}{d\tau} = C_{ab} \int_\tau^1 \frac{dx_a}{x_b} \left[f_{a/A}(x_a) f_{b/B}(x_a)(\tau/x_a) + (A \leftrightarrow B \text{ if } a \neq b) \right], \tag{A.2}$$

where C_{ab} is the color averaging factor, absorbed in $\hat{\sigma}$ in (A.1). ($C_{gg} = 1/64$, $C_{qg} = 1/24$, $C_{qq} = C_{q\bar{q}} = 1/9$.)

A massless quark inside a hadron can emit a real gluon prior to the hard interaction and thereby gains a nonzero transverse momentum k_T. The probability distribution for this splitting diverges for small k_T (a collinear divergence) or equivalently for a small virtuality $|k^2|$. Such collinear divergences can be absorbed by a redefinition of the PDFs. These then become dependent on a factorization scale μ_F, constituting the upper limit for those k_T or virtualities that are absorbed into the PDFs. For details see Ref. [113], for example.

A.2 Hadron-collider observables

In a hadron collider, the center-of-mass coordinate system of the hard scattering partons does not coincide with the laboratory coordinate system. Dependent on the longitudinal momentum fractions x_a and x_b the partons carry, the partonic center-of-mass system is boosted along the beam axis (longitudinally) with respect to the laboratory system. Collider observables therefore usually are constructed such that they either are invariant under longitudinal boosts or transform in a simple manner. In the following we define some quantities used throughout this thesis. We use spherical coordinates in the laboratory frame with azimuthal angle ϕ and polar angle ϑ. The origin is at the interaction point, and the z-axis is identified with the beam axis.

Transverse momentum $\boldsymbol{p_T}$: The projection of an object's three-momentum $\boldsymbol{p}(p, \phi, \vartheta)$—taken to originate from the laboratory system's origin—to the plane perpendicular to the beam axis:

$$p_T = p \sin \vartheta. \tag{A.3}$$

Pseudorapidity $\boldsymbol{\eta}$: For the three-momentum $\boldsymbol{p}(p, \phi, \vartheta)$ defined above, the pseudorapidity is

$$\eta = -\ln \tan \frac{\vartheta}{2} \qquad \Big(= \frac{1}{2} \ln \frac{1 + \cos \vartheta}{1 - \cos \vartheta} \Big). \tag{A.4}$$

For a particle with negligible mass, η is equal to $y = \frac{1}{2} \ln \frac{E + p_z}{E - p_z}$, the rapidity parametrizing the longitudinal boost of the particle's rest frame with respect to the laboratory frame.

Missing transverse energy ($\not{E}_T$) When two hadrons—moving along the z-axis—scatter, the total transverse momentum of all products (visible and invisible in the detector) must be zero because of momentum conservation:

$$0 = \sum_{i=1}^{N_{\text{vis.}}} \boldsymbol{p}_{Ti} + \sum_{i=1}^{N_{\text{invis.}}} \boldsymbol{p}_{Ti}. \tag{A.5}$$

Here $\boldsymbol{p}_{Ti} = p_{Ti}(\cos \phi_i, \sin \phi_i)$ is the two-dimensional projection of the three-momentum $\boldsymbol{p}_i$ into the plane perpendicular to the beam axis, for product i. The production of an undetectable particle therefore is signaled by a nonzero transverse total transverse momentum. On the detector-level, the energy-depositions in all calorimeter cells is summed up in an equivalent manner. The imbalance of this sum is $\not{E}_T$:

$$\not{E}_T = \left| \sum_{i=1}^{N_{\text{cells}}} \boldsymbol{E}_{Ti} \right|, \tag{A.6}$$

where $\boldsymbol{E}_{Ti} = E_i \sin \vartheta_i (\cos \phi_i, \sin \phi_i)$ with E_i, the energy deposition in calorimeter cell i located at ϑ_i, ϕ_i. At typical interaction energies, the masses of the scattering

products are small, so that $\boldsymbol{E}_{Ti} \approx \boldsymbol{p}_{Ti}$. Hence, $\not{E}_T$ measures the transverse-momentum imbalance caused by undetectable particles:

$$\not{E}_T \approx \left| \sum_{i=1}^{N_{\text{invis.}}} \boldsymbol{p}_{Ti} \right| . \tag{A.7}$$

Transverse impact parameter

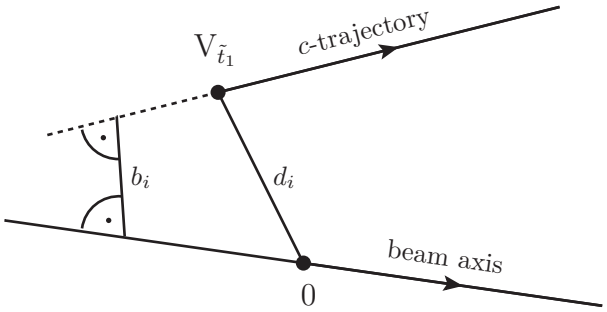

Figure A.1: Stop decay distance d_i and the impact parameter b_i of its charmed decay product ($V_{\tilde{t}_1}$: displaced stop decay vertex, 0: origin).

A.3 RGE evolution of the soft sfermion mass terms

In the normalization of Ref. [16] with $A^f \equiv (\mathsf{A}_f)_{33}/\lambda_f$ and $m^2_{\tilde{f}_X} \equiv (\mathsf{m}^2_F)_{33}$, the one-loop beta-functions for the contributions to the third generation's squark mass matrix are in the $\overline{\text{DR}}$ renormalization scheme [16, 178]:

$$\beta_{A^t} = \frac{1}{8\pi^2}\left(6\lambda_t^2 A^t + \lambda_b^2 A^b - \frac{16}{3}g_s^2 M_3 - 3g^2 M_2 - \frac{13}{9}g'^2 M_1\right), \tag{A.8a}$$

$$\beta_{A^b} = \frac{1}{8\pi^2}\left(6\lambda_b^2 A^b + \lambda_t^2 A^t - \frac{16}{3}g_s^2 M_3 - 3g^2 M_2 - \frac{7}{9}g'^2 M_1\right), \tag{A.8b}$$

$$\beta_{m^2_{\tilde{t}_\text{R}}} = \frac{1}{8\pi^2}\left(2\lambda_t^2 S_t - \frac{16}{3}g_s^2|M_3|^2 - \frac{16}{9}g'^2|M_1|^2 - \frac{2}{3}g'^2 S_Y\right), \tag{A.8c}$$

$$\beta_{m^2_{\tilde{b}_\text{R}}} = \frac{1}{8\pi^2}\left(2\lambda_b^2 S_b - \frac{16}{3}g_s^2|M_3|^2 - \frac{4}{9}g'^2|M_1|^2 + \frac{1}{3}g'^2 S_Y\right), \tag{A.8d}$$

$$\beta_{m^2_{\tilde{q}_3}} = \frac{1}{8\pi^2}\left(\lambda_t^2 S_t + \lambda_b^2 S_b - \frac{16}{3}g_s^2|M_3|^2 - 3g^2|M_2| - \frac{1}{9}g'^2|M_1|^2 + \frac{1}{6}g'^2 S_Y\right), \tag{A.8e}$$

$$\beta_{m^2_{h_u}} = \frac{1}{8\pi^2}\left(3\lambda_t^2 S_t - 3g^2|M_2| - g'^2|M_1|^2 + \frac{1}{2}g'^2 S_Y\right), \tag{A.8f}$$

$$\beta_{m^2_{h_d}} = \frac{1}{8\pi^2}\left(3\lambda_b^2 S_b - 3g^2|M_2| - g'^2|M_1|^2 - \frac{1}{2}g'^2 S_Y\right), \tag{A.8g}$$

$$\beta_{\lambda_t} = \frac{\lambda_t}{16\pi^2}\left(6\lambda_t^2 + \lambda_b^2 - \frac{16}{3}g_s^2 - 3g^2 - \frac{13}{9}g'^2\right), \tag{A.8h}$$

$$\beta_{\lambda_b} = \frac{\lambda_b}{16\pi^2}\left(6\lambda_b^2 + \lambda_t^2 - \frac{16}{3}g_s^2 - 3g^2 - \frac{7}{9}g'^2\right), \tag{A.8i}$$

$$\beta_{g_i^2} = \frac{g_i^4}{8\pi^2}b_{g_i}^{(1)}, \qquad \beta_{M_i} = \frac{g_i^2}{8\pi^2}b_{g_i}^{(1)}M_i, \tag{A.8j}$$

For $(b_{g'}^{(1)}, b_g^{(1)}, b_{g_s}^{(1)}) = (11,\ 1,\ -3)$ and (Y_i: hypercharge of field i):

$$S_t = m_{h_u}^2 + m_{\tilde{q}_3}^2 + m_{\tilde{t}_\mathrm{R}}^2 + |A^t|^2, \tag{A.9a}$$

$$S_b = m_{h_d}^2 + m_{\tilde{q}_3}^2 + m_{\tilde{b}_\mathrm{R}}^2 + |A^b|^2, \tag{A.9b}$$

$$S_Y = \frac{1}{2}\sum_i^{\text{all scalars}} Y_i m_i^2. \tag{A.9c}$$

A.4 Phase-space integrals

Phase space integrals for $\tilde{t}_1 \to \tilde{G}W^+b$ decays [120]:

$$I(a,b) = \int_a^1 dx \frac{(1-x)^4(x-a)^2}{12x^3a} \cdot \left(\frac{6x^3(3a+x)}{(x-b)^2} + \frac{4x^2(4a-x)}{x-b} + x^2 + 2xa + 3a^2\right), \tag{A.10a}$$

$$J(a,b) = \int_a^1 dx \frac{b(1-x)^4(x-a)^2(2a+x)}{2x^2a(x-b)^2}. \tag{A.10b}$$

A.5 Kaluza-Klein decomposition

Component fields of the KK-mode $h_{AB}^{(\boldsymbol{k})}$ in unitary gauge [54]:

$$G_{\mu\nu}^{(\boldsymbol{k})} = h_{\mu\nu}^{(\boldsymbol{k})} + \frac{\kappa}{3}\left(\eta_{\mu\nu} + \frac{\partial_\mu\partial_\nu}{\hat{k}^2}\right)H^{(\boldsymbol{k})}, \tag{A.11a}$$

$$V_{\mu j}^{(\boldsymbol{k})} = \frac{\mathrm{i}}{\sqrt{2}}h_{\mu j}^{(\boldsymbol{k})}, \tag{A.11b}$$

$$S_{ij}^{(\boldsymbol{k})} = h_{ij}^{(\boldsymbol{k})} - \frac{\kappa}{n-1}\left(\eta_{ij} + \frac{\hat{k}_i\hat{k}_j}{\hat{k}^2}\right)H^{(\boldsymbol{k})}, \tag{A.11c}$$

$$H^{(\boldsymbol{k})} = \frac{1}{\kappa}h^{(\boldsymbol{k})}{}_j^j, \tag{A.11d}$$

with $\kappa = \sqrt{\frac{3(n-1)}{n+2}}$, $\hat{k}_i = k_i/r$, $\hat{k}^2 = -k^jk_j = \sum_{i=1}^n |k_i|^2$. See Ref. [54] for the ungauged expressions.

A.6 Schwarzschild radius in LED

The line element for a (4+n)-dimensional Schwarzschild black hole is [179]

$$ds^2 = -f(r)dt^2 + \frac{dr^2}{f(r)} + r^2 d\Omega_{n+2}^2, \tag{A.12}$$

where $d\Omega_{n+2}^2$ is the line element of a (2+n)-dimensional unit sphere. $f(r)$ is given by

$$f(r) = \left[1 - \left(\frac{r_c}{r}\right)^{n+1}\right], \tag{A.13}$$

and yields a divergence of the line element (A.12) if $r \to r_c$, where r_c is the Schwarzschild radius in 4+n dimensions [136, 179]:

$$r_c = \left(\frac{2(2\pi)^n m_{\mathrm{BH}}}{(n+2)S_{n+2}\mathrm{M}_\star^{n+2}}\right)^{\frac{1}{n+1}}. \tag{A.14}$$

A.7 Kinematic functions in LED parton-level cross sections

Kinematic functions in the parton-level Drell-Yan cross sections [54]:

$$G_4(x) = 1 + 10x + 42x^2 + 64x^3 + 32x^4, \tag{A.15a}$$
$$G_5(x) = 1 + 6x + 12x^2 + 8x^3, \tag{A.15b}$$
$$G_6(x) = 1 + 6x + 6x^2, \tag{A.15c}$$
$$G_{12}(x) = -(x + 3x^2 + 4x^3 + 2x^4). \tag{A.15d}$$

B Simplified $\gamma\gamma\not{E}_T$ and $t\bar{t}\not{E}_T$ cuts

We enlist here kinematic cuts, adapted from Ref. [117, 118, 127]. They are implemented using a customized version of DELPHES 1.9 [124]. (We modify the program to account for a DØ-like calorimeter with more than 40 segments in η direction and flag gravitinos as undetectable particles.)

B.1 DØ—$\gamma\gamma\not{E}_T$ channel

In a simplified layout of the DØ calorimeter, cells with the dimensions $0.1 \times (2\pi/64)$ in $\eta \times \phi$ space cover $|\eta| \leq 4.2$ and $\phi \in [0, 2\pi[$. As usual η and ϕ denote the pseudorapidity and azimuthal angle in the laboratory coordinate system. Jets are reconstructed with the iterative midpoint algorithm [180] with $R = 0.5$.

Modeling Ref. [117], we apply the following event-selection criteria:

- There are at least two isolated photons with $p_T > 25\,\text{GeV}$ and $|\eta| < 1.1$.
- $\sphericalangle(\not{E}_T j) < 2.5$ if there is a jet, where $\sphericalangle(\not{E}_T j)$ is the azimuthal angle between the directions of $\not{E}_T$ and the hardest jet (p_T-ordered).
- $\sphericalangle(\not{E}_T \gamma_i) > 0.2$ for $i = 1, 2$. Here, $\sphericalangle(\not{E}_T \gamma_i)$ is the azimuthal angle between the directions of $\not{E}_T$ and the isolated photon γ_i (p_T-ordered).
- $\not{E}_T < 35\,\text{GeV}$.

95% of a photon's energy must be deposited in the electromagnetic calorimeter. A photon is considered to be isolated if the calorimetric isolation variable I (cf. Ref. [117]) is smaller than 0.1 and if the scalar sum of all transverse momenta of all tracks in a cone of $0.05 < \delta R < 0.4$ to the photon is smaller than $2\,\text{GeV}$. [δR is the usual distance in $\eta \times \phi$ space, cf. (5.19).]

Nearly in all signal events, both photons are found to be isolated. They are thus well separated from the hadronic decay products of the stops. This is expected, since both products in the decay $\tilde{\chi}_1^0 \to \tilde{G}\gamma$ are massless, while $\tilde{\chi}^0$ has a large mass. In consequence the neutralino decays dominantly decide about the photons' kinematics with a negligible influence of the original stops' flight directions.

B.2 ATLAS—$\gamma\gamma\not{E}_T$ channel

We use the default ATLAS detector layout of DELPHES. From Ref. [118], we adapt the following cuts:

- There are at least two isolated photons with $p_T < 25\,\text{GeV}$, $|\eta| < 1.81$, and $|\eta| \notin [1.37, 1.52]$.

- $\not{E}_T > 125\,\text{GeV}$.

Ref. [118] employs a tight photon selection criterion on photon candidates, where a true, prompt photon is identified with an efficiency of 85%, approximately [181]. We mimic this efficiency by randomly removing photons from our Monte-Carlo samples with a probability of 15%. In this modified sample, a photon is considered to be isolated if the scalar E_T sum of all calorimeter depositions inside a cone of $\delta R < 0.2$ is less than 5 GeV [excluding the cell the photon points to; recall the definition of δR in (5.19)].

Almost all signal photons are isolated, see the DØ case for an explanation. For larger $m_{\tilde{\chi}_1^0}$, our dominant event-number reduction stems from the artificial 85% photon selection efficiency described above.

B.3 ATLAS—$t\bar{t}\not{E}_T$ channel

Using the default ATLAS detector layout implemented in DELPHES, we apply the following simplified cuts adapted from Ref. [127]:

- There is one isolated electron with $p_T > 25\,\text{GeV}$ or one muon with $p_T > 20\,\text{GeV}$. An electron's pseudorapidity has to fulfill $|\eta| < 2.47$ and $|\eta| \notin [1.37, 1.52]$. A muon has to fulfill $|\eta| < 2.5$.
- There are no further isolated leptons with $p_T > 15\,\text{GeV}$.
- There are at least four jets with $p_T > 25\,\text{GeV}$ and $|\eta| < 2.5$.
- $\not{E}_T > 100\,\text{GeV}$.
- $m_T(\ell, \not{E}_T) = \sqrt{2p_{T,\ell}\not{E}_T[1 - \cos(\phi_\ell - \phi_{\not{E}_T})]} > 150\,\text{GeV}$ (ℓ=lepton).
- There is no single track with $p_T > 15\,\text{GeV}$ without further tracks with $p_T > 4\,\text{GeV}$ within a cone of $R = 0.4$.

Jets are reconstructed with the anti-k_T algorithm [182] with $R = 0.4$. Electrons (muons) are isolated if the scalar sum of E_T of the calorimeter cells Σ_{E_T} in a cone with $\delta R = 0.2$ ($\delta R = 0.3$) around the lepton is less than $4\,\text{GeV} + 0.023\Sigma_{E_T}$ (4 GeV) [183]. For stop masses below 300 GeV, the dominant cut is $m_T > 150\,\text{GeV}$.

C Additional Kaluza-Klein sums

C.1 Quenched approximation—KK sum with $\mu^2 = m^2$ and $s \geq 0$

Using the notation established in Sections 10.2 and 10.3 ($y^2 = s/\Lambda_T^2$), the dimensionless KK-summed graviton propagator in quenched approximation

$$C(y^2) = C_{\mathrm{IR}}(y^2) + C_{\mathrm{UV}}(y^2) \tag{C.1}$$

is given for an Euclidean propagator by

$$C_{\mathrm{IR}}(y^2) = \begin{cases} (-1)^{\frac{n}{2}} y^{n-3} \left[y \ln\left(\frac{\sqrt{1+y^2}}{y}\right) + y f_{\mathrm{IR}}^{(n)}(y^2) \right] & \text{if } n \text{ even} \\ (-1)^{\frac{n-1}{2}} y^{n-3} \left[y \tan^{-1}\left(\frac{1}{y}\right) + g_{\mathrm{IR}}^{(n)}(y^2) \right] & \text{if } n \text{ odd,} \end{cases} \tag{C.2}$$

where

$$f_{\mathrm{IR}}^{(n)}(y^2) = \sum_{\ell=1}^{\frac{n-2}{2}} \frac{(-1)^{\ell+1}}{2\ell} y^{-2\ell}, \qquad g_{\mathrm{IR}}^{(n)}(y^2) = \sum_{\ell=0}^{\frac{n-3}{2}} \frac{(-1)^{\ell+1}}{2\ell+1} y^{-2\ell} \tag{C.3}$$

and

$$C_{\mathrm{UV}}(y^2) = \frac{1}{2y^4} \left[y^2 - \ln(1+y^2) \right]. \tag{C.4}$$

The expressions for a Minkowskian propagator are obtained by analytical continuation to negative arguments, i.e. by the replacement $y^2 \to -y^2$.

C.2 Linear and quadratic approximation—seminumerical KK sums

With $x^2 = m^2/\Lambda_T^2$ and $y^2 = s/\Lambda_T^2$, the graviton wave function renormalization function Z^{-1} is in the linear and the quadratic approximation with $\mu^2 = (x^2 + y^2)\Lambda_T^2$ are given in (10.10)

Im $C(y^2)$
The imaginary part of the dimensionless KK-summed propagator, which is non-zero only for a Minkowskian propagator, can be calculated analytically [cf. (10.17)]:

$$\mathrm{Im}\, C_{\mathrm{Mink}}^{(1)} = \frac{1}{1 + (2y^2)^{\frac{n+2}{2}}} \frac{\pi y^{n-2}}{2}, \tag{C.5a}$$

$$\mathrm{Im}\, C_{\mathrm{Mink}}^{(2)} = \left(\sqrt{1 + \frac{1}{4}(2y^2)^{n+2}} - \frac{1}{2}(2y^2)^{\frac{n+2}{2}} \right) \frac{\pi y^{n-2}}{2}, \tag{C.5b}$$

where (1) and (2) denote to linear and quadratic approximations, respectively.

$\mathbf{Re}\, C(y^2)$

The other integrals can be calculated analytically for large $y^2 = s/\Lambda_T^2$. They coincide with those in quenched approximation as the transition region has a negligible contribution in this limit. Therefore, we approximate all KK sums by the quenched KK sum for $y > y_\epsilon$. The approximation-dependent and n-dependent y_ϵ is defined as that value of y, where the integrand of the KK sum in linear or quadratic approximation is overestimated relatively by less than ϵ compared to the integrand in quenched approximation (with unmatched—i.e. identified—transition scales):

$$Z^{-1}_{(1\text{ or }2)}(y_\epsilon)/Z^{-1}_{(0)}(y_\epsilon) = (1-\epsilon) \tag{C.6a}$$

$$\Rightarrow \qquad \left(y_\epsilon^{(1)}\right)^2 = \left(\frac{1-\epsilon}{\epsilon}\right)^{\frac{2}{n+2}}, \qquad \left(y_\epsilon^{(2)}\right)^2 = \left(\frac{(1-\epsilon)^2}{\epsilon}\right)^{\frac{1}{(n+2)}} \tag{C.6b}$$

For the analysis presented in Part III, we use $\epsilon = 5\%$, implying the y_ϵ^2 in Table C.1, and calculate $\mathrm{Re}\, C^{(1,2)}(y)$ numerically at 101 equidistant points y_i^2 in the interval $[0, y_\epsilon^2]$ using the computer algebra system MATHEMATICA 7, for $n = 2$–12 respectively.

Continuous expressions for $\mathrm{Re}\, C^{(1,2)}(y)$ are obtained by linear interpolation, with an exception for $n = 2$ discussed below. In comparison to other theoretical uncertainties (leading order (LO) cross sections, PDFs, scales), the interpolation error is considered to be negligible in the findings—cf. Figure C.1.

n	2	3	4	5	6	7	8	9	10	11	12
$\left(y_\epsilon^{(1)}\right)^2$	4.36	3.25	2.67	2.32	2.09	1.92	1.80	1.71	1.63	1.57	1.52
$\left(y_\epsilon^{(2)}\right)^2$	2.06	1.78	1.62	1.51	1.43	1.38	1.34	1.30	1.27	1.25	1.23

Table C.1: Integration boundaries for $\epsilon = 5\%$ according to (C.6b).

For $n = 2$, the KK-sum diverges logarithmically for $\hat{s} \to 0$,

$$\mathrm{Re}\, C(y^2)\big|_{n=2} \approx -\ln y \quad \text{(for small } y\text{)} \tag{C.7}$$

in all three approximations and for both propagator variants. For y^2 below $y^2_{\min} = y_\epsilon^2/100$, we extrapolate $\mathrm{Re}\, C(y^2)$ according to (C.7). The relative errors this approximation introduces are maximal at $y^2_{\min}$. They are 0.03%, 5%, 4%, and 4% for $C^{(1)}_{\mathrm{Eucl}}$, $C^{(2)}_{\mathrm{Eucl}}$, $C^{(1)}_{\mathrm{Mink}}$, and $C^{(2)}_{\mathrm{Mink}}$, respectively.

Breakdown of the approximation

Approximating all KK sums by the quenched one above a certain y_ϵ can result in significant approximation error on bounds on Λ_T under certain conditions: In dilepton searches, a minimal-$m_{\ell\ell}$ cut on the cross section can restrict the latter to its fixed-point regime, where it dominantly is controlled by the fraction $\Lambda_T/\mathrm{M}_\star$, with only minor

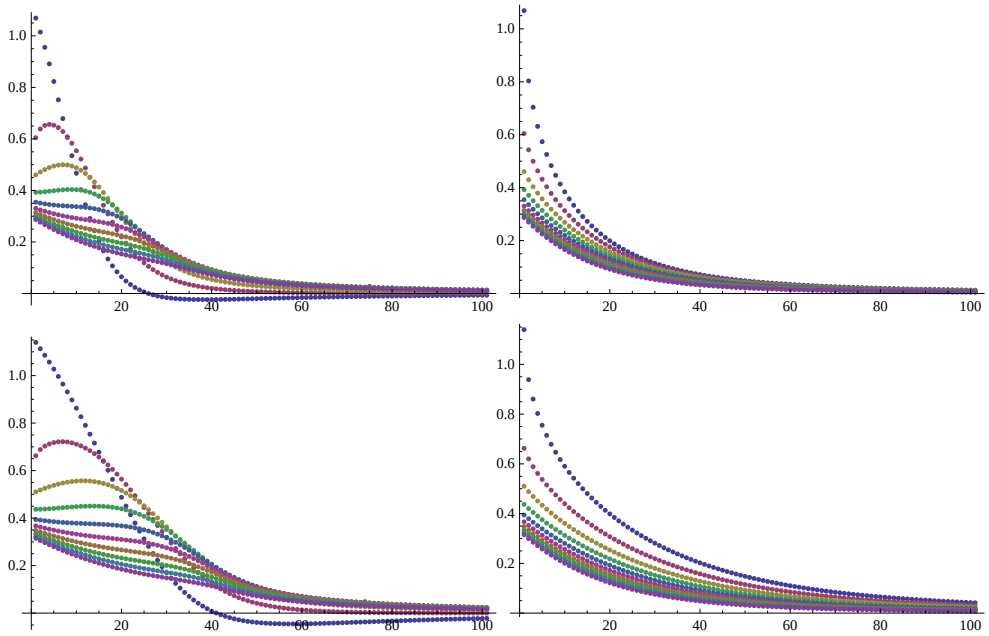

Figure C.1: Numerically calculated $\mathrm{Re}\, C(y)$, evaluated equidistantly at 101 points in $[0, y_\epsilon^2]$. y_ϵ is calculated according to (C.6) for $\epsilon = 5\%$. Upper (lower) panels: linear (quadratic) approximation; left (right) panels: Minkowskian (Euclidean) propagator.

dependencies on the individual scales. $y_{\min} = m_{\ell\ell}^{\min}/\Lambda_T$, given by the minimal-$m_{\ell\ell}$ cut, approaches y_ϵ for small values of Λ_T and the violation of $\Lambda_T/\mathrm{M}_\star$ scaling would increasingly depend on the location of $y_{\min}$ in relation to y_ϵ, but not on the true scaling violation of the KK sum.

D PYTHIA implementation of Asymptotic Safety

We implement two classes for AS dilepton production based on the LED implementation of PYTHIA 8.170 [111, 162, 163]:

$$\begin{aligned} &\texttt{Sigma2ffbar2ASLEDllbar} && \text{for } f\bar{f} \to \ell\bar{\ell}, \\ &\texttt{Sigma2gg2ASLEDllbar} && \text{for } gg \to \ell\bar{\ell}. \end{aligned} \tag{D.1}$$

Below, we list the parameters and switches added to the program. Also we shortly discuss how further KK-sum schemes may be added to the implementation.

Program parameters

`flag` **`ExtraDimensionsASLED:gg2llbar`** `(default=off)`
Switches on $gg \to \ell\bar{\ell}$ in the asymptotic safety scenario of large extra dimension.

`flag` **`ExtraDimensionsASLED:ffbar2llbar`** `(default=off)`
Switches on $f\bar{f} \to \ell\bar{\ell}$ in the asymptotic safety scenario of large extra dimension. Does not include the t-channel amplitude relevant for $e^+e^- \to e^+e^-$.

`flag` **`ExtraDimensionsASLED:MatchScales`** `(default=off)`
Controls if the transition scales in the linear and quadratic approximations are rescaled to give matching KK sums at $\hat{s} = 0$ for all three approximations.

`mode` **`ExtraDimensionsASLED:n`** `(default=4, min=1, max=12)`
The number of extra dimensions.

`parm` **`ExtraDimensionsASLED:LambdaT`** `(default=2000)`
The scale characterizing the transition between the IR regime with Gaussian fixed-point scaling and the UV regime with non-Gaussian fixed-point scaling (GeV).

`parm` **`ExtraDimensionsASLED:MD`** `(default=2000)`
The fundamental scale of gravity in $4 + n$ dimensions (GeV).

`mode` **`ExtraDimensionsASLED:ApproximationMode`** `(default=0, min=0, max=4)`
Allows to choose the regularization method of the divergent Kaluza-Klein-summed graviton propagator. With options `0`–`2`, the Kaluza-Klein sum is regularized through the introduction of a running graviton wave-function renormalization factor $Z^{-1}(\mu)$, evaluated at a renormalization scale $\mu^2 = m^2 + \hat{s}$. The three options represent three different approximations of $Z^{-1}(\mu)$ as introduced in Section 9.2. For cross checks, the options `3`–`4` reproduce the EFT result of Ref. [163].

`option 0`: Asymptotic safety, quenched approximation.

`option 1`: Asymptotic safety, linear approximation.

`option 2`: Asymptotic safety, quadratic approximation.

`option 3`: Effective theory, zero-$\hat{s}$ approximation.

`option 4`: Effective theory, zero-$\hat{s}$ approximation. Truncation of the cross section for $\hat{s} > \Lambda_T$.

`mode ExtraDimensionsASLED:IntMode (default=0, min=0, max=1)`
Allows to choose the signature of the propagator.

`option 0`: Minkowskian

`option 1`: Eulidean

`mode ExtraDimensionsASLED:SMMode (default=0, min=0, max=2)`
Controls how Standard Model amplitudes should be treated.

`option 0`: Contributions from the SM and extra dimension with interference.

`option 1`: Contributions from the SM and extra dimension withhout interference.

`option 2`: Contributions from extra dimensions only.

Implementation and the addition of new approximations

Since the KK-summed s-channel propagator is common to the two processes in (D.1), as it is to others such as $f\bar{f} \to \gamma\gamma$, its calculation is factored out into the class `ASLEDcommon::DimlessKKSumSChannel`. This class manages an object of a class implementing the interface `ASLEDcommon::KKSumImpl` explicitly for a choice of approximation, renormalization scale, and metric signature.

This scheme is intended to alleviate the addition of new variants of the KK-summed propagator while keeping the extra structures added to PYTHIA small. To add a new variant of the KK-summed propagator to the implementation, the necessary steps are 1) to derive a corresponding class from `ASLEDcommon::KKSumImpl`, 2) to add a new set of modes, flags, or parameters to PYTHIA's settings database (`XML` files) identifying the new summation, 3) to associate this set of modes with the construction of the new implementation in `ASLEDcommon::DimlessKKSumSChannel::make_impl(...)`.

Bibliography

[1] G. Aad *et al.* (ATLAS Collaboration), Phys. Lett. **B716**, 1 (2012), arXiv:1207.7214 [hep-ex]; S. Chatrchyan *et al.* (CMS Collaboration), Phys. Lett. **B716**, 30 (2012), arXiv:1207.7235 [hep-ex].

[2] G. Hiller, J. S. Kim, and H. Sedello, Phys. Rev. **D80**, 115016 (2009), arXiv:0910.2124 [hep-ph].

[3] J. S. Kim and H. Sedello, (2011), DO-TH-11-28, ADP-11-42-T764, arXiv:1112.5324 [hep-ph].

[4] G. Hiller, D. F. Litim, and H. Sedello, In preparation.

[5] S. Glashow, Nucl. Phys. **22**, 579 (1961); S. Weinberg, Phys. Rev. Lett. **19**, 1264 (1967); A. Salam, in *Elementary Particle Physics*, edited by N. Svartholm (Almqvist and Wiksell, Stockholm, 1968) pp. 367–377; D. J. Gross and F. Wilczek, Phys. Rev. Lett. **30**, 1343 (1973); H. D. Politzer, Phys. Rev. Lett. **30**, 1346 (1973).

[6] P. Langacker, Phys. Rept. **72**, 185 (1981).

[7] J. Beringer *et al.* (Particle Data Group), Phys. Rev. **D86**, 010001 (2012), 2013 partial update for the 2014 edition.

[8] J. Charles *et al.* (CKMfitter Group), Eur. Phys. J. **C41**, 1 (2005), preliminary results (FPCP 2013 conference), updated results available at `http://ckmfitter.in2p3.fr`, arXiv:hep-ph/0406184 [hep-ph].

[9] G. 't Hooft, Nucl. Phys. **B61**, 455 (1973); S. Weinberg, Phys. Rev. **D8**, 3497 (1973).

[10] N. Cabibbo, Phys. Rev. Lett. **10**, 531 (1963); M. Kobayashi and T. Maskawa, Prog. Theor. Phys. **49**, 652 (1973).

[11] L. Wolfenstein, Phys. Rev. Lett. **51**, 1945 (1983); A. J. Buras, M. E. Lautenbacher, and G. Ostermaier, Phys. Rev. **D50**, 3433 (1994), arXiv:hep-ph/9403384 [hep-ph].

[12] B. Pontecorvo, Sov. Phys. JETP **6**, 429 (1957); Z. Maki, M. Nakagawa, and S. Sakata, Prog. Theor. Phys. **28**, 870 (1962).

[13] P. Harrison, D. Perkins, and W. Scott, Phys. Lett. **B458**, 79 (1999), arXiv:hep-ph/9904297 [hep-ph]; P. Harrison, D. Perkins, and W. Scott, Phys. Lett. **B530**, 167 (2002), arXiv:hep-ph/0202074 [hep-ph]; F. An *et al.* (DAYA-BAY Collaboration), Phys. Rev. Lett. **108**, 171803 (2012), arXiv:1203.1669 [hep-ex].

[14] C. Froggatt and H. B. Nielsen, Nucl. Phys. **B147**, 277 (1979).

[15] M. Baak, M. Goebel, J. Haller, A. Hoecker, D. Ludwig, *et al.*, Eur. Phys. J. **C72**, 2003 (2012), arXiv:1107.0975 [hep-ph].

[16] M. Drees, R. M. Godbole, and P. Roy, *Theory and Phenomenology of Sparticles* (World Scientific Publishing, Singapore, 2004).

[17] G. 't Hooft and M. Veltman, Nucl. Phys. **B44**, 189 (1972).

[18] H. Aoki and S. Iso, Phys. Rev. **D86**, 013001 (2012), arXiv:1201.0857 [hep-ph].

[19] S. Weinberg, Phys. Rev. **D19**, 1277 (1979).

[20] L. Susskind, Phys. Rev. **D20**, 2619 (1979); M. Veltman, Acta Phys. Polon. **B12**, 437 (1981).

[21] G. 't Hooft, NATO Adv. Study Inst. Ser. B Phys. **59**, 135 (1980).

[22] F. Zwicky, Helv. Phys. Acta **6**, 110 (1933); L. Bergstrom, Rept. Prog. Phys. **63**, 793 (2000), arXiv:hep-ph/0002126 [hep-ph].

[23] S. Gershtein and Y. a. Zeldovich, JETP Lett. **4**, 120 (1966); R. Cowsik and J. McClelland, Phys. Rev. Lett. **29**, 669 (1972).

[24] P. Ade *et al.* (Planck Collaboration), (2013), arXiv:1303.5076 [astro-ph].

[25] J. Bond, G. Efstathiou, and J. Silk, Phys. Rev. Lett. **45**, 1980 (1980); A. Doroshkevich, Y. Zeldovich, R. Sunyaev, and M. Khlopov, Sov. Astron. Lett. **6**, 252 (1980).

[26] M. Drees and G. Gerbier, in Ref. [7], Chap. 24.

[27] E. W. Kolb and M. E. Turner, *The Early Universe* (Addison-Wesley, 1990).

[28] G. Bertone, ed., *Particle dark matter* (Cambridge Univ. Press, Cambridge, 2010).

[29] B. Moore, S. Ghigna, F. Governato, G. Lake, T. R. Quinn, *et al.*, Astrophys. J. **524**, L19 (1999), arXiv:astro-ph/9907411 [astro-ph].

[30] P. Bode, J. P. Ostriker, and N. Turok, Astrophys. J. **556**, 93 (2001), arXiv:astro-ph/0010389 [astro-ph].

[31] P. Peebles, Astrophys. J. **258**, 415 (1982); J. Bond and A. Szalay, Astrophys. J. **274**, 443 (1983); J. Bond, A. Szalay, and M. S. Turner, Phys. Rev. Lett. **48**, 1636 (1982); S. Colombi, S. Dodelson, and L. M. Widrow, Astrophys. J. **458**, 1 (1996), arXiv:astro-ph/9505029 [astro-ph].

[32] K. A. Olive and J. A. Peacock, in Ref. [7], Chap. 21.

[33] M. Viel, G. D. Becker, J. S. Bolton, M. G. Haehnelt, M. Rauch, *et al.*, Phys. Rev. Lett. **100**, 041304 (2008), arXiv:0709.0131 [astro-ph].

[34] S. Weinberg, *THE QUANTUM THEORY OF FIELDS*, Vol. III (Cambridge University Press, Cambridge, 2000).

[35] S. R. Coleman and J. Mandula, Phys. Rev. **159**, 1251 (1967).

[36] J. Wess and B. Zumino, Phys. Lett. **B49**, 52 (1974).

[37] R. Haag, J. T. Lopuszanski, and M. Sohnius, Nucl. Phys. **B88**, 257 (1975).

[38] Y. Golfand and E. Likhtman, JETP Lett. **13**, 323 (1971); J. Wess and B. Zumino, Nucl. Phys. **B70**, 39 (1974).

[39] J. Iliopoulos and B. Zumino, Nucl. Phys. **B76**, 310 (1974); M. T. Grisaru, W. Siegel, and M. Rocek, Nucl. Phys. **B159**, 429 (1979).

[40] S. P. Martin, in *Perspectives on supersymmetry*, Vol. II, edited by G. L. Kane (2010) hep-ph/9709356.

[41] B. Allanach, C. Balazs, G. Belanger, M. Bernhardt, F. Boudjema, *et al.*, Comput. Phys. Commun. **180**, 8 (2009), arXiv:0801.0045 [hep-ph].

[42] S. Ahmed *et al.* (SNO Collaboration), Phys. Rev. Lett. **92**, 102004 (2004), arXiv:hep-ex/0310030 [hep-ex].

[43] S. Weinberg, Phys. Rev. **D26**, 287 (1982).

[44] G. R. Farrar and P. Fayet, Phys. Lett. **B76**, 575 (1978).

[45] M. Dine and A. E. Nelson, Phys. Rev. **D48**, 1277 (1993), arXiv:hep-ph/9303230 [hep-ph]; M. Dine, A. E. Nelson, and Y. Shirman, Phys. Rev. **D51**, 1362 (1995), arXiv:hep-ph/9408384 [hep-ph]; M. Dine, A. E. Nelson, Y. Nir, and Y. Shirman, Phys. Rev. **D53**, 2658 (1996), arXiv:hep-ph/9507378 [hep-ph]; G. Giudice and R. Rattazzi, Phys. Rept. **322**, 419 (1999), arXiv:hep-ph/9801271 [hep-ph].

[46] S. P. Martin, Phys. Rev. **D55**, 3177 (1997), arXiv:hep-ph/9608224 [hep-ph].

[47] H. E. Haber, in *Physics from Planck scale to electroweak scale* and *Electroweak symmetry breaking* (1994) arXiv:hep-ph/9501320 [hep-ph]; J. F. Gunion and H. E. Haber, Phys. Rev. **D67**, 075019 (2003), arXiv:hep-ph/0207010 [hep-ph]; P. Nath, (2013), arXiv:1302.1863 [hep-ph].

[48] M. Misiak, S. Pokorski, and J. Rosiek, Adv. Ser. Direct. High Energy Phys. **15**, 795 (1998), arXiv:hep-ph/9703442 [hep-ph].

[49] D. Balin and A. Love, *SUPERSYMMETRIC GAUGE FIELD THEORY AND STRING THEORY* (Taylor & Francis Group, New York, 1994).

[50] D. Volkov and V. Soroka, JETP Lett. **18**, 312 (1973); S. Deser and B. Zumino, Phys. Rev. Lett. **38**, 1433 (1977); E. Cremmer, B. Julia, J. Scherk, S. Ferrara, L. Girardello, *et al.*, Nucl. Phys. **B147**, 105 (1979).

[51] P. Fayet, Phys. Lett. **B70**, 461 (1977); R. Casalbuoni, S. De Curtis, D. Dominici, F. Feruglio, and R. Gatto, Phys. Lett. **B215**, 313 (1988); R. Casalbuoni, S. De Curtis, D. Dominici, F. Feruglio, and R. Gatto, Phys. Rev. **D39**, 2281 (1989).

[52] N. Arkani-Hamed, S. Dimopoulos, and G. Dvali, Phys. Lett. **B429**, 263 (1998), arXiv:hep-ph/9803315 [hep-ph].

[53] S. Carroll, *SPACETIME AND GEOMETRY* (Addison Wesley, San Francisco, 2004).

[54] G. F. Giudice, R. Rattazzi, and J. D. Wells, Nucl. Phys. **B544**, 3 (1999), arXiv:hep-ph/9811291 [hep-ph].

[55] L. Randall and R. Sundrum, Phys. Rev. Lett. **83**, 4690 (1999), arXiv:hep-th/9906064 [hep-th].

[56] C. Csaki, (2004), arXiv:hep-ph/0404096 [hep-ph]; E. Gerwick and T. Plehn, PoS **CLAQG08**, 009 (2011), arXiv:0912.2653 [hep-ph].

[57] C. Hoyle, D. Kapner, B. R. Heckel, E. Adelberger, J. Gundlach, *et al.*, Phys. Rev. **D70**, 042004 (2004), arXiv:hep-ph/0405262 [hep-ph].

[58] D. Kapner, T. Cook, E. Adelberger, J. Gundlach, B. R. Heckel, *et al.*, Phys. Rev. Lett. **98**, 021101 (2007), arXiv:hep-ph/0611184 [hep-ph].

[59] E. G. Adelberger, B. R. Heckel, and A. E. Nelson, Ann. Rev. Nucl. Part. Sci. **53**, 77 (2003), arXiv:hep-ph/0307284 [hep-ph].

[60] J. Polchinski, (1994), arXiv:hep-th/9411028 [hep-th]; R. Maartens and K. Koyama, Living Rev. Rel. **13** (2010), 10.12942/lrr-2010-5, cited 20$^{\text{th}}$ Nov, 2013, `http://www.livingreviews.org/lrr-2010-5`; C. Rovelli, Living Rev. Rel. **11** (2008), 10.12942/lrr-2008-5, cited 20$^{\text{th}}$ Nov, 2013, `http://www.livingreviews.org/lrr-2008-5`.

[61] B. Sathyaprakash and B. F. Schutz, Living Rev. Rel. **12** (2009), 10.12942/lrr-2009-2, cited 27$^{\text{th}}$ Dec, 2013, `http://www.livingreviews.org/lrr-2009-2`.

[62] T. Kaluza, Sitzungsber. Preuss. Akad. Wiss. Berlin (Math. Phys.) **1921**, 966 (1921); O. Klein, Z. Phys. **37**, 895 (1926).

[63] J. R. Ellis, S. Kelley, and D. V. Nanopoulos, Phys. Lett. **B260**, 131 (1991); U. Amaldi, W. de Boer, and H. Furstenau, Phys. Lett. **B260**, 447 (1991); P. Langacker and M.-x. Luo, Phys. Rev. **D44**, 817 (1991).

[64] G. Aad *et al.* (ATLAS Collaboration), (2009), arXiv:0901.0512 [hep-ex].

[65] C. Collaboration, *CMS Physics TDR*, Tech. Rep. (2006).

[66] G. Aad *et al.* (ATLAS Collaboration), Phys. Rev. **D87**, 012008 (2013), arXiv:1208.0949 [hep-ex]; G. Aad *et al.* (ATLAS Collaboration), JHEP **1310**, 130 (2013), arXiv:1308.1841 [hep-ex]; S. Chatrchyan *et al.* (CMS Collaboration), *Search for supersymmetry in pp collisions at* $\sqrt{s}$ *= 8 TeV in events with a single lepton, large jet multiplicity, and multiple b jets*, Tech. Rep. (2013) arXiv:1311.4937 [hep-ex].

[67] *Commissioning of the ATLAS high-performance b-tagging algorithms in the 7 TeV collision data*, Tech. Rep. ATLAS-CONF-2011-102 (CERN, Geneva, 2011).

[68] *b-jet tagging calibration on c-jets containing* D^{*+} *mesons*, Tech. Rep. ATLAS-CONF-2012-039 (CERN, Geneva, 2012).

[69] G. Hiller and Y. Nir, JHEP **0803**, 046 (2008), arXiv:0802.0916 [hep-ph].

[70] J. S. Hagelin, S. Kelley, and T. Tanaka, Nucl. Phys. **B415**, 293 (1994).

[71] F. Gabbiani, E. Gabrielli, A. Masiero, and L. Silvestrini, Nucl. Phys. **B477**, 321 (1996), arXiv:hep-ph/9604387 [hep-ph].

[72] J. P. Saha and A. Kundu, Phys. Rev. **D69**, 016004 (2004), arXiv:hep-ph/0307259 [hep-ph].

[73] Z.-j. Xiao, F.-g. Li, and W.-j. Zou, Commun. Theor. Phys. **46**, 687 (2006), arXiv:hep-ph/0603120 [hep-ph].

[74] P. Ko and J.-h. Park, Phys. Rev. **D80**, 035019 (2009), arXiv:0809.0705 [hep-ph].

[75] M. Ciuchini, E. Franco, D. Guadagnoli, V. Lubicz, M. Pierini, *et al.*, Phys. Lett. **B655**, 162 (2007), arXiv:hep-ph/0703204 [hep-ph].

[76] S. Khalil and O. Lebedev, Phys. Lett. **B515**, 387 (2001), arXiv:hep-ph/0106023 [hep-ph].

[77] E. Gabrielli and S. Khalil, Phys. Rev. **D67**, 015008 (2003), arXiv:hep-ph/0207288 [hep-ph].

[78] J. Casas and S. Dimopoulos, Phys. Lett. **B387**, 107 (1996), arXiv:hep-ph/9606237 [hep-ph].

[79] A. Behring, C. Gross, G. Hiller, and S. Schacht, JHEP **1208**, 152 (2012), arXiv:1205.1500 [hep-ph].

[80] P. Ball, S. Khalil, and E. Kou, Phys. Rev. **D69**, 115011 (2004), arXiv:hep-ph/0311361 [hep-ph].

[81] J. Aguilar-Saavedra, Acta Phys. Polon. **B35**, 2695 (2004), arXiv:hep-ph/0409342 [hep-ph].

[82] S. Chatrchyan *et al.* (CMS Collaboration), Phys. Lett. **B718**, 1252 (2013), arXiv:1208.0957 [hep-ex].

[83] T. Han, R. Peccei, and X. Zhang, Nucl. Phys. **B454**, 527 (1995), arXiv:hep-ph/9506461 [hep-ph]; T. Han, K. Whisnant, B. Young, and X. Zhang, Phys. Rev. **D55**, 7241 (1997), arXiv:hep-ph/9603247 [hep-ph]; T. Han, M. Hosch, K. Whisnant, B.-L. Young, and X. Zhang, Phys. Rev. **D58**, 073008 (1998), arXiv:hep-ph/9806486 [hep-ph]; M. Hosch, K. Whisnant, and B. Young, Phys. Rev. **D56**, 5725 (1997), arXiv:hep-ph/9703450 [hep-ph].

[84] R. Barbieri, G. Dvali, and L. J. Hall, Phys. Lett. **B377**, 76 (1996), arXiv:hep-ph/9512388 [hep-ph]; A. Aranda, C. D. Carone, and R. F. Lebed, Phys. Rev. **D62**, 016009 (2000), arXiv:hep-ph/0002044 [hep-ph]; S. King, JHEP **0508**, 105 (2005), arXiv:hep-ph/0506297 [hep-ph]; I. de Medeiros Varzielas and G. G. Ross, Nucl. Phys. **B733**, 31 (2006), arXiv:hep-ph/0507176 [hep-ph]; F. F. Deppisch, Fortsch. Phys. **61**, 622 (2013), arXiv:1206.5212 [hep-ph].

[85] M. Leurer, Y. Nir, and N. Seiberg, Nucl. Phys. **B420**, 468 (1994), arXiv:hep-ph/9310320 [hep-ph].

[86] G. Hiller, Y. Hochberg, and Y. Nir, JHEP **0903**, 115 (2009), arXiv:0812.0511 [hep-ph]; G. Hiller, Y. Hochberg, and Y. Nir, JHEP **1003**, 079 (2010), arXiv:1001.1513 [hep-ph].

[87] A. Crivellin and U. Nierste, Phys. Rev. **D79**, 035018 (2009), arXiv:0810.1613 [hep-ph]; A. Crivellin, L. Hofer, U. Nierste, and D. Scherer, Phys. Rev. **D84**, 035030 (2011), arXiv:1105.2818 [hep-ph].

[88] A. Buras, P. Gambino, M. Gorbahn, S. Jager, and L. Silvestrini, Phys. Lett. **B500**, 161 (2001), arXiv:hep-ph/0007085 [hep-ph]; G. D'Ambrosio, G. Giudice, G. Isidori, and A. Strumia, Nucl. Phys. **B645**, 155 (2002), arXiv:hep-ph/0207036 [hep-ph]; G. Isidori and D. M. Straub, Eur. Phys. J. **C72**, 2103 (2012), arXiv:1202.0464 [hep-ph]; A. J. Buras, Acta Phys. Polon. **B34**, 5615 (2003), arXiv:hep-ph/0310208 [hep-ph].

[89] M. Blanke, A. J. Buras, D. Guadagnoli, and C. Tarantino, JHEP **0610**, 003 (2006), arXiv:hep-ph/0604057 [hep-ph].

[90] A. H. Chamseddine, R. L. Arnowitt, and P. Nath, Phys. Rev. Lett. **49**, 970 (1982).

[91] G. F. Giudice, M. A. Luty, H. Murayama, and R. Rattazzi, JHEP **9812**, 027 (1998), arXiv:hep-ph/9810442 [hep-ph]; L. Randall and R. Sundrum, Nucl. Phys. **B557**, 79 (1999), arXiv:hep-th/9810155 [hep-th]; B. Allanach, G. Hiller, D. Jones, and P. Slavich, JHEP **0904**, 088 (2009), arXiv:0902.4880 [hep-ph].

[92] G. Colangelo, E. Nikolidakis, and C. Smith, Eur. Phys. J. **C59**, 75 (2009), arXiv:0807.0801 [hep-ph]; J. Ellis, R. N. Hodgkinson, J. S. Lee, and A. Pilaftsis, JHEP **1002**, 016 (2010), arXiv:0911.3611 [hep-ph].

[93] Y. Okada, M. Yamaguchi, and T. Yanagida, Prog. Theor. Phys. **85**, 1 (1991); H. E. Haber and R. Hempfling, Phys. Rev. Lett. **66**, 1815 (1991); J. R. Ellis, G. Ridolfi, and F. Zwirner, Phys. Lett. **B257**, 83 (1991).

[94] R. Essig, Phys. Rev. **D75**, 095005 (2007), arXiv:hep-ph/0702104 [hep-ph].

[95] R. Barbieri and A. Strumia, Phys. Lett. **B462**, 144 (1999), arXiv:hep-ph/9905281 [hep-ph].

[96] S. Chatrchyan *et al.* (CMS Collaboration), (2013), arXiv:1308.1586 [hep-ex].

[97] G. Aad *et al.* (ATLAS Collaboration), (2013), arXiv:1308.2631 [hep-ex].

[98] *Search for pair-produced top squarks decaying into a charm quark and the lightest neutralinos with 20.3 fb^{-1} of pp collisions at $\sqrt{s} = 8$ TeV with the ATLAS detector at the LHC*, Tech. Rep. ATLAS-CONF-2013-068 (CERN, Geneva, 2013).

[99] LEPSUSYWG, ALEPH, DELPHI, L3, and OPAL experiments, "LEPSUSYWG/04-02.1," `http://lepsusy.web.cern.ch/lepsusy/`.

[100] T. Aaltonen *et al.* (CDF Collaboration), JHEP **1210**, 158 (2012), arXiv:1203.4171 [hep-ex].

[101] M. Carena, A. Freitas, and C. Wagner, JHEP **0810**, 109 (2008), arXiv:0808.2298 [hep-ph].

[102] A. Djouadi, M. Guchait, and Y. Mambrini, Phys. Rev. **D64**, 095014 (2001), arXiv:hep-ph/0105108 [hep-ph].

[103] W. Beenakker, M. Kramer, T. Plehn, M. Spira, and P. Zerwas, Nucl. Phys. **B515**, 3 (1998), arXiv:hep-ph/9710451 [hep-ph].

[104] J. M. Yang and B.-L. Young, Phys. Rev. **D62**, 115002 (2000), arXiv:hep-ph/0007165 [hep-ph].

[105] S. Kraml and A. R. Raklev, Phys. Rev. **D73**, 075002 (2006), arXiv:hep-ph/0512284 [hep-ph].

[106] T. Stelzer and W. Long, Comput. Phys. Commun. **81**, 357 (1994), arXiv:hep-ph/9401258 [hep-ph].

[107] J. Pumplin, D. Stump, J. Huston, H. Lai, P. M. Nadolsky, *et al.*, JHEP **0207**, 012 (2002), arXiv:hep-ph/0201195 [hep-ph].

[108] H. Pilkuhn, *The interactions of hadrons* (North-Holland, Amsterdam, 1967).

[109] W. Beenakker, R. Hopker, M. Spira, and P. Zerwas, Nucl. Phys. **B492**, 51 (1997), arXiv:hep-ph/9610490 [hep-ph].

[110] ATLAS Inner Detector Community, *ATLAS Technical Design Report*, Tech. Rep. (CERN, 1997).

[111] T. Sjostrand, S. Mrenna, and P. Z. Skands, JHEP **0605**, 026 (2006), arXiv:hep-ph/0603175 [hep-ph].

[112] B. Andersson, G. Gustafson, G. Ingelman, and T. Sjostrand, Phys. Rept. **97**, 31 (1983); T. Sjostrand, Nucl. Phys. **B248**, 469 (1984).

[113] V. D. Barger and R. J. N. Phillips, *Collider Physics* (Westview Press, Boulder, Colorado, 1991).

[114] A. C. Kraan, Eur. Phys. J. **C37**, 91 (2004), arXiv:hep-ex/0404001 [hep-ex]; M. Fairbairn, A. Kraan, D. Milstead, T. Sjostrand, P. Z. Skands, *et al.*, Phys. Rept. **438**, 1 (2007), arXiv:hep-ph/0611040 [hep-ph].

[115] S. Chatrchyan *et al.* (CMS Collaboration), JHEP **1307**, 122 (2013), arXiv:1305.0491 [hep-ex].

[116] S. Chatrchyan *et al.* (CMS Collaboration), (2013), arXiv:1311.6736 [hep-ex].

[117] V. M. Abazov *et al.* (D0 Collaboration), Phys. Rev. Lett. **105**, 221802 (2010), arXiv:1008.2133 [hep-ex].

[118] G. Aad *et al.* (ATLAS Collaboration), Phys. Lett. **B710**, 519 (2012), arXiv:1111.4116 [hep-ex].

[119] S. Ambrosanio, G. L. Kane, G. D. Kribs, S. P. Martin, and S. Mrenna, Phys. Rev. **D54**, 5395 (1996), arXiv:hep-ph/9605398 [hep-ph].

[120] U. Sarid and S. D. Thomas, Phys. Rev. Lett. **85**, 1178 (2000), arXiv:hep-ph/9909349 [hep-ph].

[121] S. P. Martin and P. Ramond, Phys. Rev. **D48**, 5365 (1993), arXiv:hep-ph/9306314 [hep-ph].

[122] S. Dimopoulos, S. D. Thomas, and J. D. Wells, Nucl. Phys. **B488**, 39 (1997), arXiv:hep-ph/9609434 [hep-ph].

[123] P. M. Nadolsky, H.-L. Lai, Q.-H. Cao, J. Huston, J. Pumplin, *et al.*, Phys. Rev. **D78**, 013004 (2008), arXiv:0802.0007 [hep-ph].

[124] S. Ovyn, X. Rouby, and V. Lemaitre, (2009), arXiv:0903.2225 [hep-ph].

[125] T. Junk, Nucl. Inst. & Meth. **A434**, 435 (1999), arXiv:hep-ex/9902006 [hep-ex]; A. L. Read, J. Phys. G **G28**, 2693 (2002).

[126] J. Conway (CDF collaboration), in *Workshop on Confidence Limits*, CERN (CERN, Geneva, 2000) pp. 247–255.

[127] G. Aad *et al.* (ATLAS), Phys. Rev. Lett. **108**, 041805 (2012), arXiv:1109.4725 [hep-ex].

[128] D. R. Tovey, JHEP **0804**, 034 (2008), arXiv:0802.2879 [hep-ph].

[129] G. Aad *et al.* (ATLAS Collaboration), Phys. Lett. B **718**, 411 (2012).

[130] G. Aad *et al.* (ATLAS Collaboration), (2013), arXiv:1304.6310 [hep-ex].

[131] S. Chatrchyan *et al.* (CMS Collaboration), J. High Energy Phys. **03**, 111. 49 p (2012).

[132] S. Chatrchyan *et al.* (CMS Collaboration), Phys. Lett. **B722**, 273 (2013), arXiv:1212.1838 [hep-ex].

[133] C. Boehm, A. Djouadi, and M. Drees, Phys. Rev. **D62**, 035012 (2000), arXiv:hep-ph/9911496 [hep-ph]; J. R. Ellis, K. A. Olive, and Y. Santoso, Astropart. Phys. **18**, 395 (2003), arXiv:hep-ph/0112113 [hep-ph]; G. Belanger, S. Kraml, and A. Pukhov, Phys. Rev. **D72**, 015003 (2005), arXiv:hep-ph/0502079 [hep-ph].

[134] C. Csaki, L. Randall, and J. Terning, Phys. Rev. **D86**, 075009 (2012), arXiv:1201.1293 [hep-ph].

[135] T. Banks and W. Fischler, (1999), arXiv:hep-th/9906038 [hep-th].

[136] S. Dimopoulos and G. L. Landsberg, Phys. Rev. Lett. **87**, 161602 (2001), arXiv:hep-ph/0106295 [hep-ph].

[137] S. B. Giddings and S. D. Thomas, Phys. Rev. **D65**, 056010 (2002), arXiv:hep-ph/0106219 [hep-ph].

[138] E. Gerwick, D. Litim, and T. Plehn, Phys. Rev. **D83**, 084048 (2011), arXiv:1101.5548 [hep-ph].

[139] J. P. Dabruck, *Constraining Asymptotically Safe Quantum Einstein Gravity in Large Extra Dimensions*, Diploma thesis, TU Dortmund (2012).

[140] K. Falls, D. F. Litim, and A. Raghuraman, Int. J. Mod. Phys. **A27**, 1250019 (2012), arXiv:1002.0260 [hep-th].

[141] M. H. Goroff and A. Sagnotti, Phys. Lett. **B160**, 81 (1985).

[142] G. 't Hooft and M. Veltman, Annales Poincare Phys. Theor. **A20**, 69 (1974); S. Deser and P. van Nieuwenhuizen, Phys. Rev. **D10**, 401 (1974); S. Deser, H.-S. Tsao, and P. van Nieuwenhuizen, Phys. Rev. **D10**, 3337 (1974).

[143] T. Han, J. D. Lykken, and R.-J. Zhang, Phys. Rev. **D59**, 105006 (1999), arXiv:hep-ph/9811350 [hep-ph].

[144] S. Weinberg, in *General relativity: an Einstein centenary survey*, edited by S. W. Hawking and W. Israel (Cambridge University Press, Cambridge, 1980) Chap. 16.

[145] M. Reuter and F. Saueressig, New J. Phys. **14**, 055022 (2012), arXiv:1202.2274 [hep-th].

[146] M. Niedermaier and M. Reuter, Living Rev. Rel. **9**, 5 (2006), cited 27$^{\text{th}}$ Mar, 2013, `http://www.livingreviews.org/lrr-2006-5`; D. F. Litim, Phil. Trans. Roy. Soc. London **A369**, 2759 (2011), arXiv:1102.4624 [hep-th].

[147] D. F. Litim, Phys. Rev. Lett. **92**, 201301 (2004), arXiv:hep-th/0312114 [hep-th].

[148] C. Wetterich, Phys. Lett. **B301**, 90 (1993); M. Reuter, Phys. Rev. **D57**, 971 (1998), arXiv:hep-th/9605030 [hep-th].

[149] D. F. Litim, Phys. Rev. **D64**, 105007 (2001), arXiv:hep-th/0103195 [hep-th].

[150] A. Codello, R. Percacci, and C. Rahmede, Int. J. Mod. Phys. **A23**, 143 (2008), arXiv:0705.1769 [hep-th]; A. Codello, R. Percacci, and C. Rahmede, Annals Phys. **324**, 414 (2009), arXiv:0805.2909 [hep-th]; K. Falls, D. Litim, K. Nikolakopoulos, and C. Rahmede, (2013), arXiv:1301.4191 [hep-th].

[151] R. Percacci and D. Perini, Phys. Rev. **D68**, 044018 (2003), arXiv:hep-th/0304222 [hep-th]; R. Percacci and D. Perini, Phys. Rev. **D67**, 081503 (2003), arXiv:hep-th/0207033 [hep-th]; G. Narain and R. Percacci, Class. Quant. Grav. **27**, 075001 (2010), arXiv:0911.0386 [hep-th]; G. Narain and C. Rahmede, Class. Quant. Grav. **27**, 075002 (2010), arXiv:0911.0394 [hep-th]; P. Schuh, *Renormalization Group Flow of Gravity with Scalar Fields*, Master's thesis, TU Dortmund (2013).

[152] J. Hewett and T. Rizzo, JHEP **0712**, 009 (2007), arXiv:0707.3182 [hep-ph].

[153] J. Schröder, *Unitarity Bounds for Higgs Scattering within a* $4+n$ *dimensional setup of Fixed Point Gravity*, Diploma thesis, TU Dortmund (2011).

[154] J. Brinkmann, G. Hiller, D. F. Litim, and J. Schröder, DO-TH 12/25, to appear.

[155] J. L. Hewett, Phys. Rev. Lett. **82**, 4765 (1999), arXiv:hep-ph/9811356 [hep-ph].

[156] C. Burgess, Living Rev. Rel. **7** (2004), cited 27$^{\text{th}}$ Mar, 2013, `http://www.livingreviews.org/lrr-2004-5`.

[157] G. F. Giudice, T. Plehn, and A. Strumia, Nucl. Phys. **B706**, 455 (2005), arXiv:hep-ph/0408320 [hep-ph].

[158] P. Mathews, V. Ravindran, K. Sridhar, and W. van Neerven, Nucl. Phys. **B713**, 333 (2005), arXiv:hep-ph/0411018 [hep-ph]; P. Mathews and V. Ravindran, Nucl. Phys. **B753**, 1 (2006), arXiv:hep-ph/0507250 [hep-ph]; M. Kumar, P. Mathews, and V. Ravindran, Eur. Phys. J. **C49**, 599 (2007), arXiv:hep-ph/0604135 [hep-ph].

[159] O. J. Eboli, T. Han, M. Magro, and P. Mercadante, Phys. Rev. **D61**, 094007 (2000), arXiv:hep-ph/9908358 [hep-ph]; K.-m. Cheung and G. L. Landsberg, Phys. Rev. **D62**, 076003 (2000), arXiv:hep-ph/9909218 [hep-ph]; M. Kumar, P. Mathews, V. Ravindran, and A. Tripathi, Phys. Lett. **B672**, 45 (2009), arXiv:0811.1670 [hep-ph]; N. Agarwal, V. Ravindran, V. K. Tiwari, and A. Tripathi, Phys. Rev. **D82**, 036001 (2010), arXiv:1003.5450 [hep-ph].

[160] P. Mathews, S. Raychaudhuri, and K. Sridhar, Phys. Lett. **B450**, 343 (1999), arXiv:hep-ph/9811501 [hep-ph].

[161] P. Mathews, S. Raychaudhuri, and K. Sridhar, JHEP **0007**, 008 (2000), arXiv:hep-ph/9904232 [hep-ph].

[162] H. Sun, Y.-J. Zhou, and H. Chen, Eur. Phys. J. **72**, 2011 (2012), arXiv:1211.5197 [hep-ph]; T. Sjostrand, S. Mrenna, and P. Z. Skands, Comput. Phys. Commun. **178**, 852 (2008), arXiv:0710.3820 [hep-ph].

[163] S. Ask, I. Akin, L. Benucci, A. De Roeck, M. Goebel, *et al.*, Comput. Phys. Commun. **181**, 1593 (2010), arXiv:0912.4233 [hep-ph].

[164] S. Chatrchyan *et al.* (CMS Collaboration), *Search for Extra Dimensions in Dimuon Events in pp Collisions at* $\sqrt{s} = 8$ *TeV*, Tech. Rep. CMS-PAS-EXO-12-027 (CERN, Geneva, 2013); S. Chatrchyan *et al.* (CMS Collaboration), *Search for Large Extra Spatial Dimensions in Dielectron Production with the CMS Detector*, Tech. Rep. CMS-PAS-EXO-12-031 (CERN, Geneva, 2013).

[165] A. Martin, R. Roberts, W. Stirling, and R. Thorne, Phys. Lett. **B531**, 216 (2002), arXiv:hep-ph/0201127 [hep-ph].

[166] W. Tung, H. Lai, A. Belyaev, J. Pumplin, D. Stump, *et al.*, JHEP **0702**, 053 (2007), arXiv:hep-ph/0611254 [hep-ph].

[167] E. Gerwick, Private communication.

[168] The HL-LHC project, `http://hilumilhc.web.cern.ch/hilumilhc/index.html`.

[169] G. Aad *et al.* (ATLAS Collaboration), Phys. Rev. **D87**, 015010 (2013), arXiv:1211.1150 [hep-ex]; S. Chatrchyan *et al.* (CMS Collaboration), Phys. Lett. **B711**, 15 (2012), arXiv:1202.3827 [hep-ex].

[170] H.-L. Lai, M. Guzzi, J. Huston, Z. Li, P. M. Nadolsky, *et al.*, Phys. Rev. **D82**, 074024 (2010), arXiv:1007.2241 [hep-ph]; A. Martin, W. Stirling, R. Thorne,

and G. Watt, Eur. Phys. J. **C63**, 189 (2009), arXiv:0901.0002 [hep-ph]; R. D. Ball *et al.* (NNPDF Collaboration), JHEP **1005**, 075 (2010), arXiv:0912.2276 [hep-ph].

[171] S. Chatrchyan *et al.* (CMS Collaboration), JHEP **1209**, 094 (2012), arXiv:1206.5663 [hep-ex].

[172] M. Zenglein, Master's thesis, TU Dortmund (2014), in preparation.

[173] M. Lamont, "LHC, HL-LHC and beyond," (HEP 2013 Conference, Stockholm, 2013) Jul, 2013.

[174] M. Lamont, "Post LS1 Schedule," (RLIUP Workshop, Archamps, 2013) Oct, 2013.

[175] H. Baer, T. Barklow, K. Fujii, Y. Gao, A. Hoang, *et al.*, *The International Linear Collider Technical Design Report - Volume 2: Physics*, Tech. Rep. (2013) arXiv:1306.6352 [hep-ph].

[176] P. Lebrun, L. Linssen, A. Lucaci-Timoce, D. Schulte, F. Simon, S. Stapnes, N. Toge, H. Weerts, and J. Wells, eds., *The CLIC Programme: towards a staged e^+e^- Linear Collider exploring the Terascale. CLIC Conceptual Design Report*, Tech. Rep. CERN-2012-005 (CERN, 2012).

[177] R. P. Feynman, Phys. Rev. Lett. **23**, 1415 (1969).

[178] S. P. Martin and M. T. Vaughn, Phys. Rev. **D50**, 2282 (1994), arXiv:hep-ph/9311340 [hep-ph].

[179] R. C. Myers and M. Perry, Annals Phys. **172**, 304 (1986).

[180] G. C. Blazey, J. R. Dittmann, S. D. Ellis, V. D. Elvira, K. Frame, *et al.* (2000) arXiv:hep-ex/0005012 [hep-ex].

[181] G. Aad *et al.* (ATLAS Collaboration), Phys. Rev. **D83**, 052005 (2011), arXiv:1012.4389 [hep-ex]; G. Aad *et al.* (ATLAS Collaboration), (2010), `http://cdsweb.cern.ch/record/1273197`.

[182] M. Cacciari, G. P. Salam, and G. Soyez, JHEP **0804**, 063 (2008), arXiv:0802.1189 [hep-ph].

[183] G. Aad *et al.* (ATLAS Collaboration), Eur. Phys. J. **C71**, 1577 (2011), arXiv:1012.1792 [hep-ex].